MEASUREMENT OF ADHESION BETWEEN CALCIUM OXALATE MONOHYDRATE AND MODEL SURFACES USING A DYNAMIC WET CELL

By

CRAIG F. HABEGER

A DISSERTATION PRESENTED TO THE GRADUATE SCHOOL
OF THE UNIVERSITY OF FLORIDA IN PARTIAL FULFILLMENT
OF THE REQUIREMENTS FOR THE DEGREE OF
DOCTOR OF PHILOSOPHY

UNIVERSITY OF FLORIDA

1997

This work is dedicated to my loving and supportive wife,

Nicole Habeger,

my parents,

James and Sandra Habeger,

and

my brother and sister, niece and nephew,

Larrin Habeger and Bonnie, Miranda, and Ralph Isaac Testa.

You are all the greatest!

ACKNOWLEDGMENTS

I would like to thank all of the people who made this research possible. Sincere thanks are extended to Dr. James H. Adair, my committee chair and advisor, for his guidance and patience. I would like to recognize the other members of my committee, Drs. Christopher D. Batich, Anthony B. Brennan, and Brij M. Moudgil, from the Department of Materials Science and Engineering, and Dr. Raymond L. Hackett, from the Department of Pathology. All of these gentlemen contributed to the work reported herein and I am grateful for their advice. I would also like to thank Dr. Saeed R. Khan, from the Department of Pathology, who was not lucky enough to be on my committee but graciously gave me advice on my research anyway. I appreciate the advice given to me by Dr. John J. Mecholsky, Jr., from the Department of Materials Science and Engineering, and his willingness to substitute for Dr. Brennan during my defense. I would like to acknowledge the National Institutes of Health grant number POG 5P01 DK20586-17 which supported the work reported herein.

I would like to acknowledge the staff of the Major Analytical Instrumentation Center (MAIC) for valuable advice, discussions, and training. I would also like to thank Paula Scott, Pat Glenton, and Karen Byer for all of their assistance throughout my research.

I am grateful to all of my friends, those in Dr. Adair's research group and those not in the group. When I broke my leg, you showed me what friends really are. Special thanks are extended to Drs. Robert E. Chodelka, Malanie L. Carasso, Tuo Li and soon to be Drs. Jeffrey A. Kerchner, Nelson S. Bell, and Paul A. Demkowicz for their fruitful intellectual conversations but mostly for their lousy card playing ability.

I am indebted to my wife, Nicole, who nursed me through a broken leg, twice, and many other aches and pains too numerous to develop upon. She pushed me to finish, however, at times, not hard enough. I would like to thank my entire family for being so supportive. Finally, but most importantly, I would like to thank my personal Lord and Savior, Jesus Christ, without whom none of this would be possible.

TABLE OF CONTENTS

ACKNOWLEDGMENT ii

LIST OF TABLES viii

LIST OF FIGURES x

ABSTRACT xvi

CHAPTERS

1 INTRODUCTION 1
- 1.1 Introduction 1
- 1.2 Literature Review 1
- 1.3 Development and Characterization of Model COM Particles 2
- 1.4 Evaluation of the Calcium Oxalate Monohydrate Hamaker Constant 3
- 1.5 Development of the Dynamic Wet Cell and Streaming Potential Measurements 3
- 1.6 Measurement of COM Adhesion to Macromolecular Substrates 4
- 1.7 Conclusions and Future Research 4

2 LITERATURE REVIEW 5
- 2.1 Introduction 5
- 2.2 Particle Interactions 7
  - 2.2.1 Electrostatic Repulsion 9
  - 2.2.2 Attraction 14
  - 2.2.4 Interaction Energy 15
- 2.3 Aggregation Mechanisms Among Particles and Particles at Surfaces 17
  - 2.3.1 Particle Aggregation in Simple Electrolytes 19
  - 2.3.2 Secondary Minimum Coagulation 19
  - 2.3.3 Heterocoagulation 20
  - 2.3.4 Polymer Bridging Flocculation 23
  - 2.3.5 Flocculation of COM Particles by Phospholipids and other Intercellular Substances 26
  - 2.3.6 Adhesion of Particles at Surfaces 26
- 2.4 The Human Kidney 31
- 2.5 Characterization Techniques 34

2.5.1 Electrokinetic Measurements 34
2.5.1.1 Electrophoresis 36
2.5.1.2 Streaming Potential 36
2.5.2 Scanning Probe Microscopy 41
2.5.3 Scanning Electron Microscopy 43
2.5.4 Fourier Transform Infrared Spectroscopy 43
2.5.5 Particle Size Determination 45
2.5.6 X-Ray Diffraction 48

3 DEVELOPMENT AND CHARACTERIZATION OF MODEL COM PARTICLES 49
3.1 Introduction 49
3.2 Preparation and Characterization of Calcium Oxalate Monohydrate Particles under Different Conditions 54
3.2.1 COM particles ("33" particles) without seeds 54
3.2.2 COM particles with seeds 56
3.2.3 COM particles precipitated from homogeneous solution at 90°C 56
3.2.4 Characterization 58
3.2.5 Crystal and Atomic Structure Modeling Using the Computer Programs SHAPE© and ATOMS© 60
3.3 Results and Discussion 62
3.3.1 COM particles ("33" particles) without seeds 66
3.3.2 COM particles ("33" particles) with seeds 69
3.3.3 COM particles precipitated from homogeneous solution at 90°C 71
3.3.4 Atomic structures of COM particles as a function of habit plane for the high temperature form 71
3.3.5 Characterization of COM crystals 79
3.4 Conclusions 82

4 EVALUATION OF THE CALCIUM OXALATE MOMOHYDRATE HAMAKER CONSTANT BASED ON STATIC DIELECTRIC CONSTANT DETERMINATION AND ELECTRONIC POLARIZATION 85
4.1 Introduction 85
4.2 Materials and Methods 89
4.3 Results and Discussion 95
4.4 Conclusions 103

5 DEVELOPMENT OF THE DYNAMIC WET CELL AND STREAMING POTENTIAL MEASUREMENTS 106
5.1 Introduction 106
5.2 Materials and Methods 109
5.2.1 Adhesion Measurements using the Dynamic Wet Cell 109
5.2.2 Streaming Potential Measurement 116

5.3 Results and Discussion 122
5.3.1 Dynamic Wet Cell 122
5.3.2 Model COM Particles 125
5.3.3 Streaming Potential 127
5.3.4 Adhesion 131
5.3.5 Theoretical Modeling of Interactions 133
5.4 Conclusions 138

6 MEASUREMENT OF COM ADHESION TO MACROMOLECULAR SUBSTRATES 140
6.1 Introduction 140
6.2 Materials and Methods 143
6.2.1 Particle Synthesis and Characterization 143
6.2.2 Substrate Coating 143
6.2.3 Adhesion Measurements 145
6.2.4 Streaming Potential Measurements 146
6.3 Results and Discussion 146
6.3.1 Substrate Coverage 146
6.3.2 Zeta Potential Determinations 149
6.3.3 Adhesion Measurements 153
6.3.4 Hydrodynamic Model of the Human Kidney 167
6.4 Conclusions 170

7 SUMMARY AND FUTURE WORK 173
7.1 Summary 173
7.2 Future Work 175

APPENDICES

A DETERMINATION OF THE AREA OF COM CRYSTALLOGRAPHIC FACES USING EQUIVALENT SPHERICAL DIAMETER 177

B DETERMINATION OF THE STRESS IN THE KIDNEY AS A FUNCTION OF FLOW AND DISTANCE FROM THE TUBULE WALL 179

REFERENCES 182

BIOGRAPHICAL SKETCH 192

LIST OF TABLES

Table page

3.1. Composition of artificial urine ion solution 61

3.2. Values of the lattice parameters of calcium oxalate monohydrate 63

3.3. Atomic coordinates of Whewellite 65

3.4. Crystal forms and corresponding central distance values used to generate the theoretical shape of COM crystals 68

3.5. Values of the crystallographic data for the high temperature form of Whewellite 73

3.6. Atomic coordinates for high temperature form of Whewellite 75

4.1. Index of refraction for COM as a function of optical direction and wavelength 88

4.2. The composite mixing rules which were evaluated 90

4.3. Molecular structures of the silane coupling agents used to disperse COM in Eccosil® 5019 silicone. 92

4.4. Dielectric constant values of COM determined by fitting the mixing rules to the experimental data 98

4.5. Calculated values of the UV characteristic frequency and corresponding dielectric constants and refractive indices as a function of crystallographic direction determined from Cauchy plots 102

4.6. Comparison of A_{131} calculated for COM using Gregory's approximation vs. the Tabor-Winterton relationship. 105

5.1. A list of the physical parameters necessary to calculate zeta potential from streaming potential. 121

6.1. The values of zeta potential of the macromolecular substrates determined using streaming potential measurements in saturated COM solution 151

6.2. Values of adhesion strength for COM particles adhering to macromolecular substrates as a function of crystallographic habit plane in COM saturated solution.....165

6.3. Values of adhesion strength for COM particles adhering to macromolecular substrates as a function of crystallographic habit plane in AUIS.....166

6.4. Human kidney tubule dimensions and volumetric flow rates reported by Kok and Khan. 169

LIST OF FIGURES

Figure page

2.1. Pathways to kidney stone formation. 6

2.2. COM particle aggregate attached to the wall of the proximal tubule in a rat nephron with one end of the constituent crystals joined together (near the arrow) and the other end free. 8

2.3. The electrical double layer structure illustrating the distribution of ions surrounding an electrostatically charged particle....10

2.4. The effect of electrolyte concentration on the ionic cloud and particle seperation distance in a (A) low ionic strength solution and a (B) high ionic strength solution....11

2.5. The effect of ioic strength on zeta potential or the electric potential at the shear plane....13

2.6. A schematic diagram illustrating the attractive, repulsive, and total energy curves for two interacting materials as afunction of seperation distance....16

2.7. A schematic representation of six aggregation mechanisms which may contribute to stone formation....18

2.8. Heterocoagulation of COM with HU is predicted based on: (A) zeta potential determinations, (B) mixing of HU and COM at pCa $\leq$ 5 where COM and HU are both negatively charged, and (C) mixing at pCa = 4 where COM and HU are both oppositely charged. 22

2.9. A schematic representation of patch charge flocculation whereby incomplete macromolecular coverage may create electrostatic shielding or opposite charge in the case of a charged polymer. 24

2.10. Scenario depicting the balance of hydrodynamic forces (F_d) and adhesive forces (F_a) acting on a COM particle bound to the brush border in the human nephron. 29

2.11. A scanning electron photomicrograph of a tubule cross section in the rat animal model demonstrating association of a COM crystal with the basement membrane. 32

2.12. A schematic illustration of a human nephron....33

2.13. A schematic representation of a tubule wall found in a kidney. 35

2.14. A schematic representing charged particle movement in an applied electric field to determine electrophoretic mobility. 37

2.15. A schematic representaion of the flow of ions under an applied hydrodynamic pressure which generate the potential across the capillary or streaming potential. 39

2.16. A schematic diagram of the SPM. 42

2.17. Multiple internal reflection within the internal reflection element which is coupled to the sample. 44

2.18. Sampling depth as a function of wavenumber for the KRS-5 internal reflection element having a 45° incident angle. 46

2.19. A schamatic diagram of a Coulter counter, electrical pulse counting instrument. 47

3.1. Possible aggregation mechanisms for particles in the urinary environment. 51

3.2. Schematic representation of processing steps for the preparation of COM crystals ("33" particles) without seeds....55

3.3. Schematic representation of processing steps for the preparation of COM crystals ("33" particles) with seeds. 57

3.4. Schematic representation of processing steps for the preparation of COM crystals ("32" particles) with heat treatment at 90°C. 59

3.5. (A) SEM photomicrograph and (B) and (C) theoretical equilibrium shapes of the COM crystals precipitated without seeds.(B) The equilibrium shape of COM crystals based on the crystallographic data of Deganello and Piro and (C) the equilibrium shape of COM crystals based on the crystallographic data of Tazzoli and Domeneghetti. 64

3.6. Theoretical atomic structures of COM crystals as a function of habit plane: (A) and (B) are the (010) and (100) planes, respectively, drawn using Cocco and Sabelli atomic coordinates; (C) and (D) are the (010) and (100) planes, respectively, drawn using Tazzoli and Domeneghetti atomic coordinates; (E) and (F) are the (010) and (100) planes, respectively, drawn using Deganello and Piro atomic coordinates. 67

3.7. SEM photomicrographs and theoretical equilibrium shapes of seed crystals and the COM crystals precipitated using seeds:(A) seed crystals, (B) equilibrium shapes of seed crystals generated with the (001) and (010) faces, respectively, (C) COM crystals grown using seeds, and (D) equilibrium shape of COM crystals....70

3.8. SEM photomicrograph and theoretical equilibrium shapes of the COM crystals precipitated from homogeneous solution at 90°C:(A) COM crystals, (B) equilibrium shapes of an individual COM crystal and a crystal with a twin generated on the (001) face, and (C) equilibrium shapes of COM crystals generated using the (010) face as the dominant face. 72

3.9. Theoretical atomic high temperature structure (stability range: 318-415 K) of COM crystals as a function of habit plane, (A) (010) and (B) ($10\bar{1}$)....76

3.10 A (top) typical experimental COM x-ray diffraction pattern and (bottom) the JCPDS file for the mineral Whewellite....77

3.11. The differential frequency vs. equivalent spherical diameter particle size distribution of the experimentally produced COM crystals grown without seeds fit to a log-normal probability distribution....79

3.12. The relative linear dimensions of experimentally produced COM crystals....80

3.13 Zeta potential as a function of pH for COM in saturated COM solution and zeta potential at pH 6 for COM in 10% AUIS. 81

3.14 Contact mode SPM scan of the COM (010) crystallographic face showing the surface roughness. 83

3.15 Contact mode SPM scan of the COM ($10\bar{1}$) crystallographic face showing the surface roughness. 84

4.1. Optical photomicrographs of COM particles dispersed in Eccosil® 5019 using (A) no coupling agent, (B) SMAEPS coupling agent, and (C) GPTMS coupling agent....96

4.2. The composite mixing rules fit to experimental dielectric data. 97

4.3. Cauchy plots for water and COM as a function of optical direction. 101

5.1. (A) A picture and (B) a schematic diagram of the dynamic wet cell developed to measure adhesion of particulate to surfaces.In (B), structural thru-holes have been omitted from the drawing to improve clarity. 108

5.2. (A) A picture and (B) a schematic diagram of the dynamic wet cell supporting equipment....112

5.3. A time lapse sequence of events during an adhesion experiment.The flow rates are (A) 12 ml/min, (B) 53 ml/min, and (C) 108ml/min. 113

5.4. COM particles of controlled morphology shown in a (A) scanning electron micrograph, (B) modeled using SHAPE© software showing the two dominant crystallographic faces, (010) and ($10\bar{1}$), and (C) demonstrating the relative crystallographic size ratios. 114

5.5. Theoretical (010) and ($10\bar{1}$) crystallographic planes of calcium oxalate monohydrate.The $Ca^{2+}/C_2O_4^{2-}$ ratio is given above each theoretical atomic structure. 115

5.6. A (A) picture and a (B) schematic diagram of the streaming potential cell....117

5.7. A diagram of the R-C circuit used to eliminate asymmetry and electrode polarizations....118

5.8. (A) A picture and (B) a schematic diagram of the streaming potential instrument including all of the supporting equipment. 119

5.9. A plot of dial setting versus volumetric flow rate used to calibrate the pump.The error bars represent the standard deviation of five individual experiments. 123

5.10. A plot of flow rate versus Reynolds number indicating the stable flow inside the dynamic wet cell at all experimental flow rates....124

5.11. Experimentally determined zeta potential of COM particles in saturated calcium oxalate monohydrate solution.Each data point is the mean +/- 95% confidence interval.The ionic strength of the saturated COM solution was $8x10^{-6}$ M....126

5.12. A plot of pressure drop or driving pressure across the streaming capillary indicating that the flow is laminar under all experimental flow conditions. 128

5.13. A plot of streaming potential vs. driving pressure for fused quartz in COM saturated solution showing a linear regression with an r^2=0.98 and 95% confidence limits.....129

5.14. The probability of an initial particle on the (010) and on the ($10\bar{1}$) adhering versus the applied stress acting on the particle at failure as determined using the dynamic wet cell.The total number of particles counted that were lying on the (010) was n=255 and on the ($10\bar{1}$) was n=380. 132

5.15. A scanning probe microscopy image of the fused quartz surface under a COM saturated solution liquid environment.Also given is the image roughness statistics which include the ra or mean surface roughness of 0.871 nm. 135

6.1. A plot of wavenumber vs. absorbance for fused quartz, collagen type I, fibronectin, MATRIGEL®, and PEI produced using ATR-FTIR.All of the macromolecular substrates were coated on fused quartz. 147

6.2. A plot of wavenumber vs. absorbance for fused quartz, collagen type I, fibronectin, MATRIGEL®, and PEI produced using ATR-FTIR for the wavenumbers 2100-3600 cm^{-1}.All of the macromolecular substrates were coated on fused quartz. 148

6.3. Zeta potential as a function of pH for COM in saturated COM solution and zeta potential at a pH of 6 for COM in 10% AUIS. 150

6.4. A plot of driving pressure vs. streaming potential for the substrates collagen type I, fibronectin, MATRIGEL® , and PEI 152

6.5. The probability of an initial COM particle on the (010) and the ($10\bar{1}$) adhering to fused quartz in AUIS versus the applied stress acting on a particle at failure as determined using the dynamic wet cell.The total number of particles counted lying on the (010) was n=113 and on the ($10\bar{1}$) was n=84.....154

6.6. The probability of an initial COM particle on the (010) and the ($10\bar{1}$) adhering to collagen type I in COM saturated solution versus the applied stress acting on a particle at failure as determined using the dynamic wet cell.The total number of particles counted lying on the (010) was n=82 and on the ($10\bar{1}$) was n=133. 155

6.7. The probability of an initial COM particle on the (010) and the ($10\bar{1}$) adhering to collagen type I in AUIS versus the applied stress acting on a particle at failure as determined using the dynamic wet cell.The total number of particles counted lying on the (010) was n=84 and on the ($10\bar{1}$) was n=72.....156

6.8. The probability of an initial COM particle on the (010) and the ($10\bar{1}$) adhering to fibronectin in COM saturated solution versus the applied stress acting on a particle at failure as determined using the dynamic wet cell.The total number of particles counted lying on the (010) was n=87 and on the ($10\bar{1}$) was n=104. 157

6.9. The probability of an initial COM particle on the (010) and the ($10\bar{1}$) adhering to fibronectin in AUIS versus the applied stress acting on a particle at failure as determined using the dynamic wet cell.The total number of particles counted lying on the (010) was n=95 and on the ($10\bar{1}$) was n=143 158

6.10. The probability of an initial COM particle on the (010) and the ($10\bar{1}$) adhering to MATRIGEL® in COM saturated solution versus the applied stress acting on a particle at failure as determined using the dynamic wet cell.The total number of particles counted lying on the (010) was n=57 and on the ($10\bar{1}$) was n=54. 159

6.11. The probability of an initial COM particle on the (010) and the ($10\bar{1}$) adhering to PEI in COM saturated solution versus the applied stress acting on a particle at failure as determined using the dynamic wet cell.The total number of particles counted lying on the (010) was n=61 and on the ($10\bar{1}$) was n=69....160

6.12. A bar chart summarizing the adhesion data experimentally determined in COM saturated solution (i.e., low ionic strength).The numbers above each set of bars is the value of the zeta potential for each substrate. 161

6.13. A bar chart summarizing the adhesion data experimentally determined in COM saturated solution (i.e., low ionic strength).The numbers above each set of bars is the value of the zeta potential for each substrate. 163

6.14. COM particles (A) coated during an adhesion experiment using fibronectin and (B) uncoated COM particles used in an adhesion experiment.Both photomicrographs were taken after flow. 168

6.15. A plot of the stress on a 5 μm to 8 μm radius model COM particle under the hydrodynamic conditions found in the different areas in the human kidney.The shaded region represents the range of experimentally measured values of adhesion of COM to biological materials....171

Abstract of Dissertation Presented to the Graduate School
of the University of Florida in Partial Fulfillment of the
Requirements for the Degree of Doctor of Philosophy

MEASUREMENT OF ADHESION BETWEEN CALCIUM OXALATE MONOHYDRATE AND MODEL SURFACES USING A DYNAMIC WET CELL

By

Craig F. Habeger

December, 1997

Chairman: Dr. James H. Adair
Major Department: Materials Science and Engineering

Calcium oxalate monohydrate (COM) is the primary constituent in kidney stones. COM crystals were synthesized in the laboratory and characterized. Computer calculations of particle shape have been reconciled to observed shapes of COM crystals experimentally synthesized under various conditions. Comparison between the theoretical atomic structures generated by computer calculations are consistent with previously reported atomic layering sequences.

Composite mixing rules were used to deconvolute the dielectric constant of COM from a COM/silicone composite. Utilizing the Lichtenecker dielectric mixing model, the value of the static dielectric constant of COM was determined to be 28.9. Optical and dielectric data were then used in the Tabor-Winterton relationship to calculate the Hamaker constant, A_{131}, of COM particles interacting in water. The A_{131} for COM as a

function of crystallographic habit also was examined. The mean value of A_{131} for COM was calculated to be 13.7×10^{-21} J at 37°C in an aqueous environment.

A hydrodynamic method for measuring the adhesion of particles to a surface has been designed for use in the study of kidney stone disease and other pathological biomineralization phenomena. The hydrodynamic force required to displace a particle adhering to a fused quartz substrate was calculated via the Poiseuille equation. The strength necessary to remove 50% of the COM particles adhering to the substrate on the (010) and $(10\bar{1})$ crystallographic surfaces are 81 and 170 Pa, respectively. The previously determined Hamaker constant and measured values of zeta potential were used to calculate the energy of interaction between a COM particle and the fused quartz substrate which was found to be comparable to experimentally measured values, provided the separation distance was on the order of 20 nm.

Using the instrument and technique developed, the adhesion of COM to biologically and non-biologically relevant materials was measured in COM saturated solution and in an artificial urine ion solution. The biologically significant materials were the proteins collagen type I, fibronectin, and MATRIGEL®, a mixture of basement membrane proteins. The non-biologically relevant material was polyethyleneimine a positively charged macromolecule used as a control. MATRIGEL® and the positive control, polyethyleneimine, exhibited the highest adhesion to COM crystals.

CHAPTER 1
INTRODUCTION

1.1 Introduction

Kidney stones effect hundreds of thousands of people each year. In 1991, 895,467 visits were made to doctors for both kidney and ureter stones [NIH97] and in 1993, kidney and ureter stones resulted in approximately 302,00 hospitalizations [Cla95]. The direct and indirect cost of kidney and ureter stones in 1993 was approximately $1.83 billion [Nat95]. Prevention of kidney stones is the focus of much research; however, before prevention can occur the mechanisms of stone formation must be understood.

1.2 Literature Review

Chapter 2 reviews the pertinent kidney stone literature and gives background on techniques utilized in the work reported herein. Kidney stone disease has been described as an opportunistic disease which can rely on many causative mechanisms acting in concert [Fin78a, Fin84]. One of those possible mechanisms is the growth of an adherent particle, called a fixed particle, in the lumen of a nephron. Such an adherent particle can subsequently grow by secondary nucleation and growth and/or aggregation of crystallites to a size large enough to occlude a renal tubule, which is the basis of the fixed stone mechanism of kidney stone development. Finlayson and Reid [Fin78b] calculated the time for a COM crystal to grow to a large enough size to cause an occlusion and determined that the crystal would not have time enough to grow to such a size.

Therefore, crystal attachment is a necessary process in kidney stone formation [Man91, Man94].

Renal injury has also been implicated in fixed stone formation [Gil79, Kha84, Man91]. Khan [Kha82, Kha95a] has discussed that after attachment of a crystal to the epithelial cell surface, injury to the cell may or may not occur.

A few different results may ensue due to crystal attachment to the epithelial cell. The cell may die and be washed away in the urine flow taking with it the crystal. The cell may envelope the crystal and continue to function normally [Lie92, Lie93, Lie94] with no further growth of the crystal. However, if epithelial cell injury has occurred, basement membrane proteins may be accessible to adhere to COM crystals by sloughing of the cells leaving behind the exposed underlying architecture, the basement membrane. The basement membrane is a layer of proteins that underlies the epithelial sheet and will be discussed subsequently in more detail. Depending on the extent of injury, other proteins common to the extracellular matrix found below the basement membrane may also be accessible for attachment to COM crystals.

Researchers have shown the attachment of COM crystals to epithelial cells and fibrous proteins characteristic of those found in the basement membrane and extracellular matrix, yet the importance of these individual materials in kidney stone formation with respect to COM crystal adhesion is not known. The necessity to determine the important materials most responsible for COM crystal adhesion will allow researchers to focus their interests to those more important materials in the search for a possible cause and therefore relief from kidney stone formation.

1.3 Development and Characterization of Model COM Particles

Chapter 3 demonstrates the laboratory synthesis of COM particles having a desired size and crystallographic shape to be used in adhesion experiments. The optimal particle shape is spherical; however, COM has a monoclinic crystal structure and

spherical, crystalline particles cannot be produced. Therefore well-defined shaped, rectangular particles having a narrow size distribution were produced to limit errors associated with calculations. The experimentally produced particles were modeled using computer software to determine the crystallographic face indices and the theoretical atomic structure of two dominant crystallographic faces. The particles were characterized using electrophoresis and atomic force microscopy. The zeta potential values for the particles were determined using electrophoresis in a low ionic strength solution, COM saturated solution, and a high ionic strength solution, artificial urine ion solution. Finally, the surface roughness of each of the two dominant crystal faces were measured in saturated COM solution using contact mode Atomic Force Microscopy.

1.4 Evaluation of the Calcium Oxalate Monohydrate Hamaker Constant

Chapter 4 involves the determination of the Hamaker constant, a measure of the van der Waals interaction forces, for COM. Attractive van der Waals forces are very important in the adhesion process and a reliable value of the Hamaker constant is necessary to determine these forces. The COM particles developed in Chapter 3 were mixed with a silicone material to produce a composite. The dielectric properties of the composite were measured and composite mixing rules were used to deconvolute the dielectric constant of COM from the COM/silicone composite. Optical and dielectric data were then used to calculate the Hamaker constant, A_{131}, of COM particles interacting in water.

1.5 Development of the Dynamic Wet Cell and Streaming Potential Measurements

Chapter 5 describes the development of a hydrodynamic method for measuring the adhesion of particles to a surface for use in the study of kidney stone disease and other pathological biomineralization phenomena. By using hydrodynamic flow to remove particles from a model surface, the strength with which particles adhere to a surface can

be measured. The hydrodynamic force required to displace a particle is calculated via the Poiseuille equation using the dynamic wet cell dimensions and the fluid flow rate. A model surface consisting of fused, spectroscopic grade quartz was used in the development of the apparatus. Also developed was an instrument to measure the electrostatic potential, called zeta potential, at the surface of a flat substrate in solution. The previously determined Hamaker constant and measured values of zeta potential were used to calculate the energy of interaction between a COM particle and the fused quartz substrate. The theoretical values of adhesive pressure were compared to the measured values of adhesion.

1.6 Measurement of COM Adhesion to Macromolecular Substrates

Chapter 6 investigates the adhesion of COM to both biologically relevant and non-biologically relevant materials. The adhesion measurements were measured in COM saturated solution and in an artificial urine ion solution, using the instrument and technique developed in this research. The use of two different ionic strength solutions allows interpretation of the types of material-material interactions taking place (i.e., van der Waals, electrostatic, chemical) to be made. The biologically significant materials were the proteins collagen type I, fibronectin, and MATRIGEL®, a mixture of basement membrane proteins. The non-biologically relevant material was polyethyleneimine, PEI, a positively charged macromolecule used as a control.

1.7 Conclusions and Future Research

Chapter 7 summarizes the conclusions of the current research and presents suggestions for future work.

CHAPTER 2
LITERATURE REVIEW

2.1 Introduction

Kidney stone disease has been called an opportunistic disease because it is thought that kidney stone disease takes an unfortunate, simultaneous convergence of factors that may be achieved by several pathways for a stone to form [Con90, Fin78a, Fin84, Rob86]. Thus, injury, supersaturation (particularly hyperoxaluria), nucleation and growth mechanisms all play a role in contributing to stone formation as demonstrated in Figure 2.1. Even so, urolithiasis is idiopathic with no one risk factor providing an obvious source of stones in chronic stone formers. However, both *in vivo* and *in vitro* evidence indicates that the presence of particles is a necessary but insufficient condition for stone formation. Most non-stone forming individuals, at certain times, have crystalluria yet do not have a stone incident. For a stone to be created from freely flowing particles, either a particle must grow to a large enough size to occlude the tubule or aggregation of multiple particles must occur. Furthermore, if aggregation is responsible for stone formation, the attractive energy or energies holding the primary particles together in an aggregate must be great enough to withstand the hydrodynamic shear forces due to the flow of fluid through the nephron.

The possibility that the growth of a large crystal leads to a stone has been shown to be unlikely by several teams of investigators [Fin78b, Kok94]. Finlayson and Reid [Fin78b] predicted that there was not enough time for a freely flowing particle to grow to a size sufficient to occlude the tubule based upon the hydrodynamics in the nephron and measured rates of crystal growth for calcium oxalate monohydrate. It was also suggested

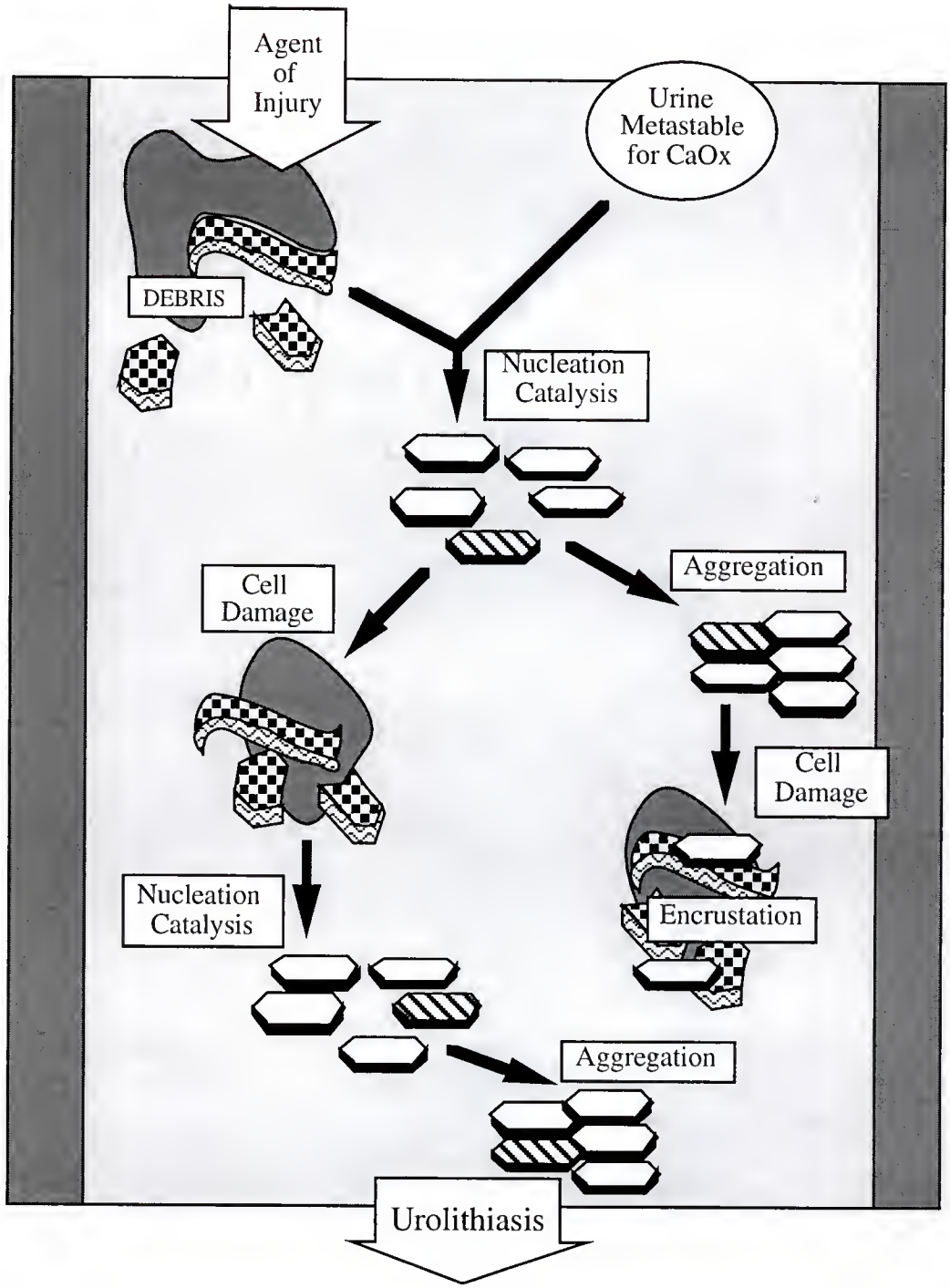

Figure 2.1. Pathways to kidney stone formation.

by Finlayson and Reid that aggregation of freely flowing particles was not likely due to the relatively low concentration of particles within the nephron at any given point in time. However, a recent analysis of the hydrodynamic aspects of transit time through the nephron by Kok and Khan [Kok94], based on better estimates of the diameters of different regions in the nephron, indicated that aggregation of freely flowing particles is possible. Regardless, attachment of calcium oxalate particles to the epithelial nephron wall has been demonstrated in a rat animal model [Fin84, Fin78b], as shown in Figure 2.2. Thus, the concept of fixed particles at the epithelial wall has become a fundamental principle in the development of kidney stones. In more recent work [Kha84, Man87, Man91, Rie88], it has been demonstrated that particle attachment can be induced by epithelial wall damage in which intercellular species, such as phospholipids, may play a role.

The objective of this chapter is to review the dynamics of aggregation for particles and interactions of the particles and/or aggregates with biological surfaces such as the basement membrane or interluminal wall of the nephron. The nature of the forces among particles and surfaces will be discussed with respect to the hydrodynamic flow scheme found in the nephron; however, particle-particle interactions must first be discussed.

2.2 Particle Interactions

Particles in solution are constantly moving. The movement of the smaller particles (<1 μm) is due to Brownian motion, also called perikinetic motion. The movement of larger particles (>5 μm), defined as orthokinetic motion, is due to gravity and convection currents. The constant motion in solution causes the particles to interact with one another ultimately resulting in either stabilization or aggregation. When repulsive forces dominate the particle-particle interaction, stabilization is the result. The opposite is the case if attractive forces dominate the particle-particle interaction, called aggregation. These forces arise from an electrostatic potential on the surface of the

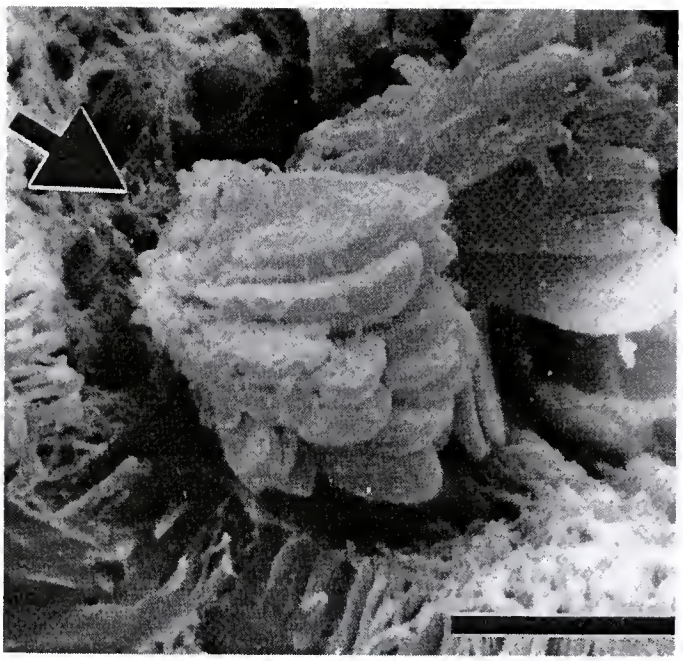

Figure 2.2. COM particle aggregate attached to the wall of the proximal tubule in a rat nephron with one end of the constituent crystals joined together (near the arrow) and the other end free (bar = 5 μm). Photomicrograph by S.R. Khan [Kha91].

particles and from an inherent dipole interaction of atoms and molecules within one particle interacting with another particle.

2.2.1 Electrostatic Repulsion

The surface potential, Ψ_o, is the potential difference between the solid surface and the bulk solution. Ions which alter the surface potential are called potential determining ions. Curreri et al. [Cur79] have hypothesized that Ca^{2+} and $C_2O_4^{2-}$ specifically adsorb to the COM surface and, thus, are termed the potential determining ions for COM.

The Gouy-Chapman electrical double layer model describes the excess ions present on the surface of the solid phase and the distribution of ionic charge of opposite sign in the solution phase surrounding the electrically charged surface which assures electroneutrality. A schematic diagram of the Gouy-Chapman model is shown in Figure 2.3. The double layer model consists of an inner layer, often called the Stern layer, which describes ions adsorbed into the compact or inner region of the double layer, and the outer or diffuse layer [Ove52]. Theoretical analysis of the double layer shows that the charge density in an aqueous solution decreases rapidly with increasing distance from the solid surface, and the electrostatic potential for low potentials is given by the Debye-Hückel approximation [Hun81],

$$\psi = \psi_o \exp(-\kappa x), \tag{2.1}$$

where ψ is the potential as a function of distance into the solution, κ is called the Debye-Hückel parameter (1/length), and x is the distance from the solid surface.

Based on the electrostatic model for aggregation, in the simplest case, the repulsive contributions between particles in solution arise from the interaction of ionic clouds surrounding the particles, as demonstrated by Figure 2.4. The extent of the ionic cloud is governed by the solution ionic strength described by the simplified equation

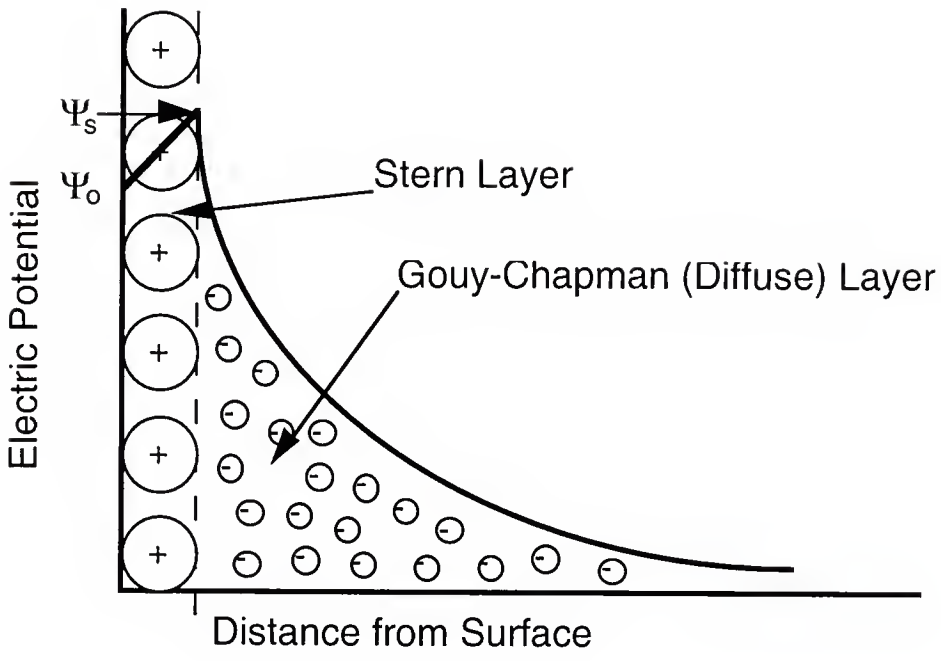

Figure 2.3. The electrical double layer structure illustrating the distribution of ions surrounding an electrostatically charged particle.

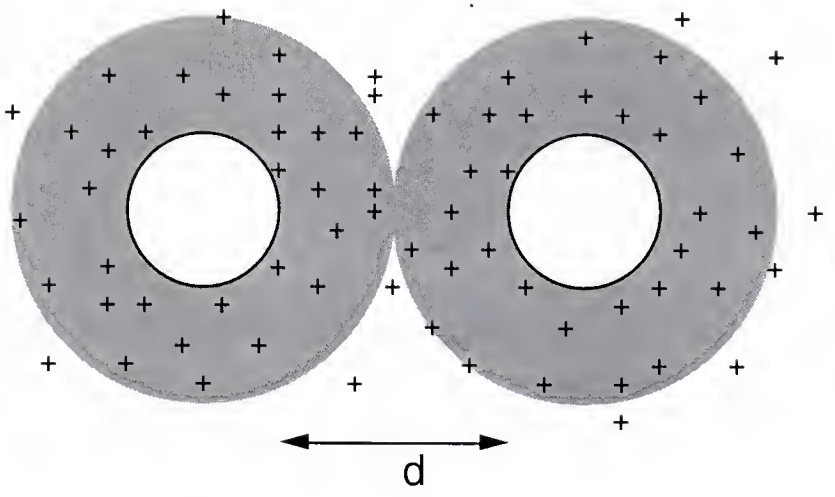

(A)

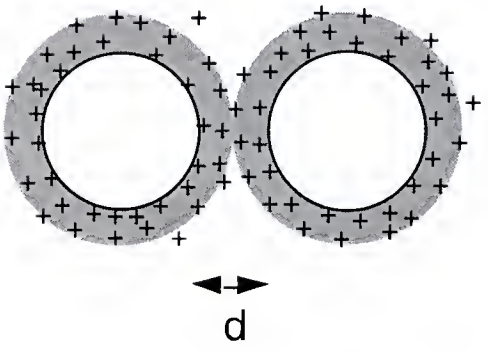

(B)

Figure 2.4. The effect of electrolyte concentration on the ionic cloud and particle separation distance in a (A) low ionic strength solution and a (B) high ionic strength solution.

$$\kappa = \left(\frac{e^2 \sum_i n_i^o z_i^2}{\varepsilon k T} \right)^{1/2} \tag{2.2}$$

where e is the elemental charge, n_i^o, is the number of ions of type i per unit volume far from the surface, z_i is the valence of ions of type i, ε is the dielectric permittivity of the solvent, k is the Boltzmann constant, and T is the temperature in Kelvin. The Debye-Hückel simplification assumes that the surface potential or stern potential is low (e.g., less than 25 mV). The quantity $1/\kappa$ is referred to as the Debye length and indicates the thickness of the double layer. The Debye length is dependent only on temperature, valence of the electrolyte ions, and electrolyte concentration. Solution ionic strength, I, is given by

$$I = \frac{1}{2} \sum_i \left(c_i z_i^2 \right) \tag{2.3}$$

where c_i is the solution concentration (M). As the ionic strength of the solution increases, the surface charge decay into the solution occurs more rapidly due to the inability of the solution to support charge. That is, the diffuse double layer becomes compressed due to the increased concentration of ions in solution as demonstrated in Figure 2.5. The increased concentration of ions near the charged particle surface causes the electrical charge to be neutralized by the ions of opposite charge, counterions, in solution. Figure 2.4 schematically describes the ionic cloud surrounding a charged particle in low and high ionic strength environments. The variable d in Figure 2.4 is the distance of separation for the two charged particles. At low ionic strength, the ionic cloud is large and electrostatic repulsion prevent particle-particle contact. At higher ionic strength the particles can

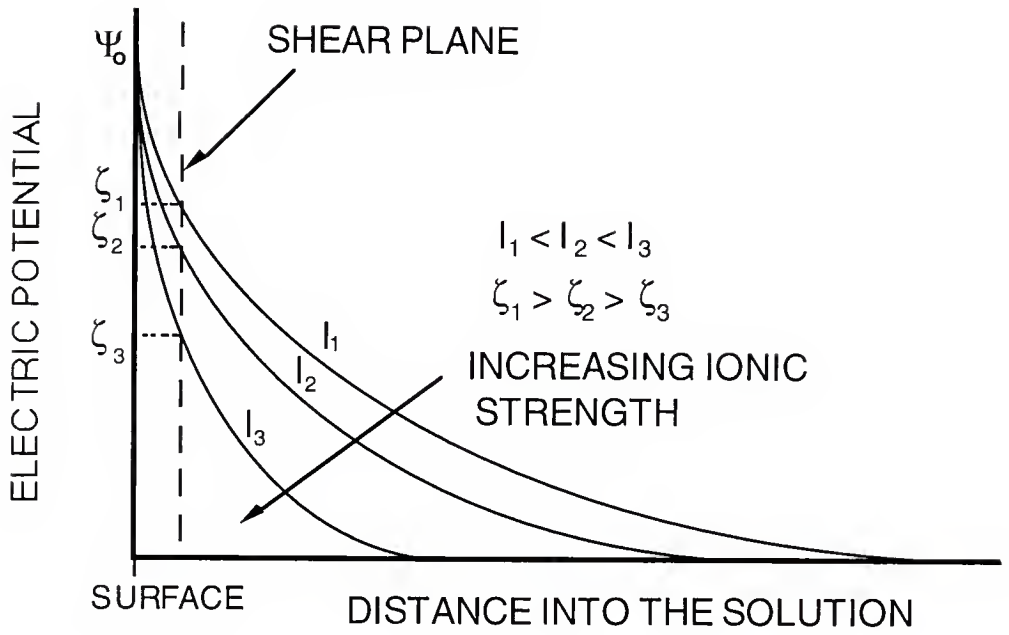

Figure 2.5. The effect of ioic strength on zeta potential or the electric potential at the shear plane.

come into much closer proximity due to collapse of the surrounding ionic cloud. If the collapse is significant, aggregation may occur.

2.2.2 Attraction

The tendency towards aggregation can result from oppositely charged electrostatic potentials or from van der Waals forces which are present at all times, irrespective of solution conditions. The attractive van der Waals forces are composed of multiple intermolecular interactions between the ions, molecules, and electrons that make up the particles interacting across a dielectric medium such as water [Hou80, Hun93, Ber90]. The mutual attraction between interacting particles arise from harmonic oscillations at the molecular, atomic, or subatomic level. Three primary sources of such intermolecular interactions exist depending upon the nature of the interacting species. Some of the more important specific dispersion interactions are known as Keesom, Debye, and London interactions [Isr92]. Keesom forces are due to molecular dipole-dipole interactions in the particles. Debye interactions occur when molecular dipoles in one particle induce electronic polarization in the other interacting particle. As such, Keesom and Debye interactions occur only if a material has one or more dipoles present within its structure. In contrast, London interactions are more ubiquitous because London interactions are due to mutual electronic polarization with all atoms, or electron cloud density shift, of adjacent atoms.

The range of the force due to dipole interactions between two atoms or molecules is a nanometer or less and varies as $1/r^6$. However, the interactions are to some degree additive in that they effect all neighboring atoms or molecules in a particle. Particle-particle van der Waals forces interact over a much longer range, $1/r^2$.

2.2.4 Interaction Energy

The Derjaguin and Landau [Der41] and Verway and Overbeek [Ver48] (DLVO) theory considered colloid stability in terms of the electrical double layer and van der Waals forces. Figure 2.6 is a plot of interaction energy as a function of separation distance, which is a potential energy diagram for two interacting materials across a medium. Positive interaction energy refers to repulsive energy and negative interaction energy refers to attractive energy. In the diagram both the attractive and repulsive portions are plotted with respect to separation distance of the two interacting materials. The third interaction line is the sum of the attractive and repulsive curves, the total interaction energy curve. Labeled on the total interaction energy curve in Figure 2.6 are the primary and secondary minimum, and the energy barrier to aggregation.

The primary minimum is the potential energy well that occurs when the two interacting materials are in contact. The main attractive forces are due to van der Waals forces. When two interacting particles are at a separation distance such that their associated interaction energy is in the primary minimum, the attractive energies dominate the total interaction energy and the two materials cannot be separated. The two particles are said to be thermodynamically unstable with respect to dispersion.

The secondary energy minimum occurs at larger separation distances, beyond the energy barrier. When two interacting materials are in the secondary energy minimum, they form a weak aggregate and may be dispersed with the addition of energy. The secondary minimum is thermodynamically metastable with respect to aggregation.

The potential energy barrier to aggregation occurs between 1 to 4 nm [Isr92] and is due to strong electronic repulsion between the ionic clouds of the interacting particles and is dependent on the surface potential. If the surface potential is high, then the potential energy barrier will be high; and, if the surface potential is low, the potential energy barrier will be low. As the electrolyte concentration of the medium increases, the energy barrier

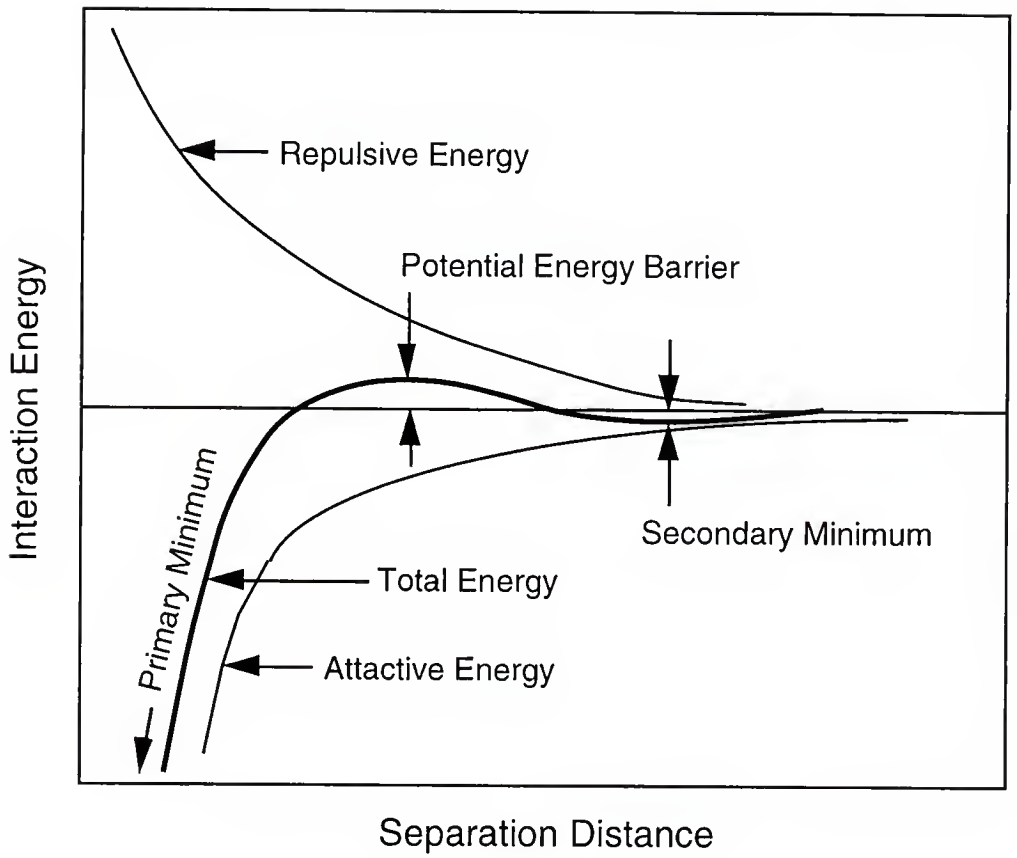

Figure 2.6. A schematic diagram illustrating the attractive, repulsive, and total energy curves for two interacting materials as a function of seperation distance.

decreases and aggregation becomes more and more likely to occur. Finally, at the critical coagulation concentration, the concentration of electrolyte at which the repulsive energy barrier falls below zero, aggregation occurs.

2.3 Aggregation Mechanisms Among Particles and Particles at Surfaces

Numerous studies [Fin78a, Fin84, Fin78b, Rie88, Ada81, Coe91, Deg91, Edy86, Edy87a, Har86a, Har86b, Kok90, Rob85, Rya81a, Rya81b, Rya81c, Rya84, Rya86, Scu86a, Scu86b, Wie87] have shown that the aggregation and/or adhesion of COM particles potentially can lead to the ultrastructures composing kidney stones. However, the actual mechanism(s) of aggregation within the biophysical environment of the human kidney have not been examined in detail. There are at least six aggregation mechanisms, as shown in Figure 2.7, acting alone or in concert which may contribute to stone formation [Ada95].

To establish dispersion techniques which may prevent stone formation, first it is necessary to determine the most important aggregation mechanisms with respect to interparticle strength. A number of possible mechanisms exist for COM aggregation within the human kidney. In addition to minimum double layer interactions, other interactions include secondary minimum coagulation, heterocoagulation, polymer bridging flocculation, aggregation by secondary nucleation and growth, and immiscible amphiphilic molecule flocculation. Hydrodynamic factors also need to be considered, including the size of the tubule and the shear rate associated with fluid flow within the nephron, as discussed by Finlayson and Reid [Fin78b], and Kok and Khan [Kok94]. Furthermore, the concentration of the COM particles performs a role whether one is considering fixed stone disease or aggregation of the particles in a freely flowing state. Finally, the flow patterns associated with peristaltic compared to continuous flow within the nephron have not been addressed in past studies but should be to realistically assess aggregate formation

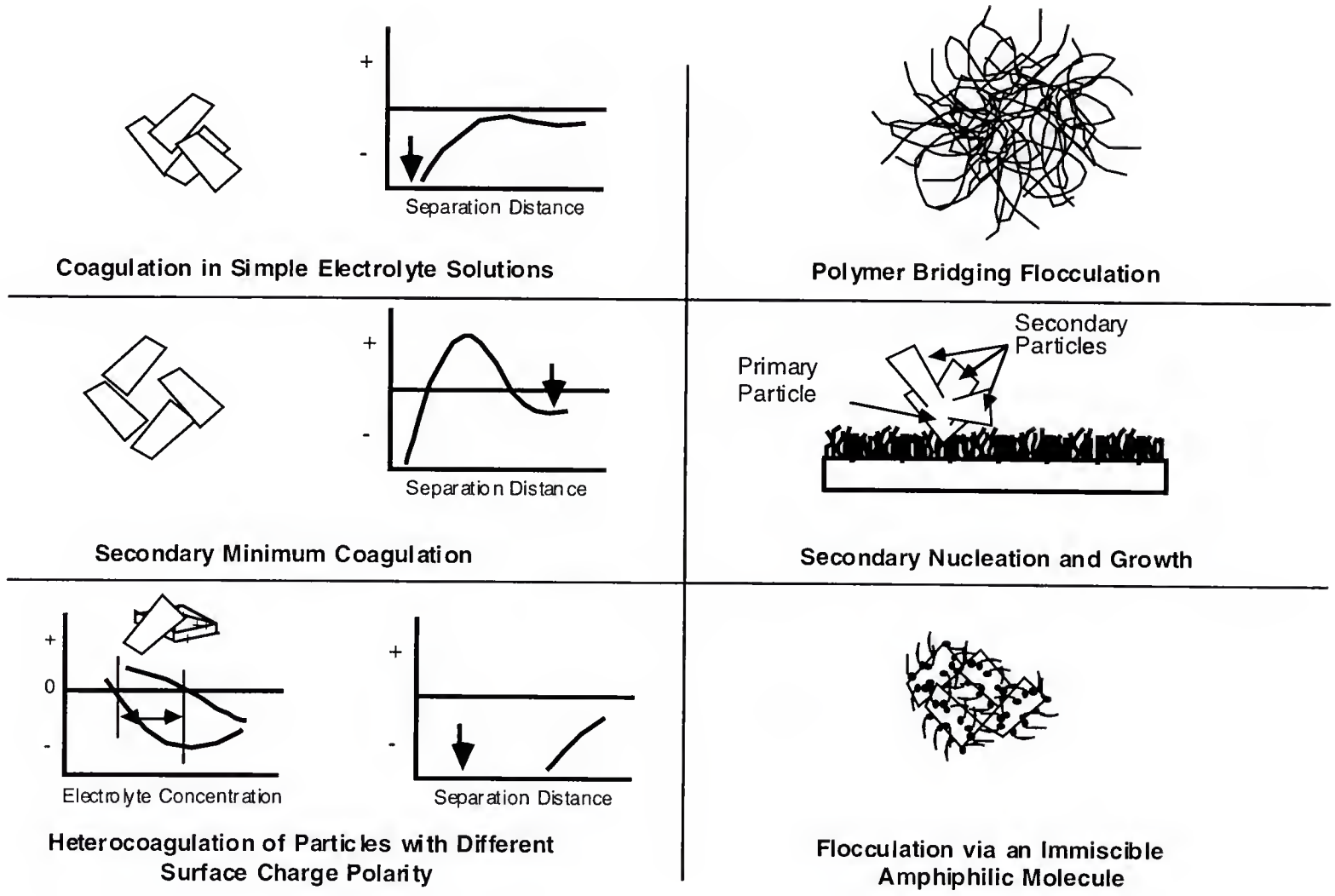

Figure 2.7. A schematic representation of six aggregation mechanisms which may contribute to stone formation [Ada95].

in the kidney. Each of the mechanisms will be discussed with respect to their likelihood in the human nephron.

2.3.1 Particle Aggregation in Simple Electrolytes

The aggregation of COM particles has traditionally been attributed to the absence of charge on COM particle surfaces and/or the high ionic strength of urine. However, neither of these aggregation mechanisms accommodates the observation that COM particles observed *in vivo* invariably have organic matter on their surfaces, as shown in Figure 2.2. Generally, particles in aqueous solution have a surface charge created by a combination of several different charging mechanisms. In the case of COM, Curreri et al. [Cur79a, Cur79b, Cur87] showed that surface charge is due to incongruent dissolution of the constituent Ca^{2+} and $C_2O_4^{2-}$. These and other species from solution then can adsorb (in their hydrated form) into an adsorbed ion layer known as the Stern layer. The electroneutrality of the system, composed of the surface and Stern charges and surrounding solution, is achieved by the charge in the diffuse cloud of ions that only are attracted electrostatically toward the surface.

2.3.2 Secondary Minimum Coagulation

As shown in Figure 2.7, a minimum exists at relatively large distances of separation in the interaction energy for COM particles. As the ionic strength increases, the magnitude of this secondary minimum increases. The secondary minimum in the interaction energy curve is a consequence of the longer range of the van der Waals attractive forces than the electrostatic repulsive interactions [Hou80, Son72]. Thus, even when the charge at the surfaces of the interacting particles is great enough to produce an energy barrier at intermediate separation distances, secondary minimum coagulation may take place because there is no energy barrier for this mechanism of aggregation. The strength of the interparticle bonds for secondary minimum interactions has been evaluated

theoretically and experimentally by Chan and Halle [Cha84]. It was demonstrated that the mean lifetime for secondary minimum aggregates increased with increasing ionic strength of the suspension containing the model spherical polystyrene particles.

Adair [Ada81] showed that COM suspensions composed of relatively coarse primary particles (~5 μm equivalent spherical diameter) aggregate over a wide range of solution and surface charge conditions. Secondary minimum aggregation was implicated in conditions where primary minimum aggregation was minimized because of low ionic strength and relatively high zeta potential. However, the results were ambiguous because only the thermodynamic aspects of the coagulation process were addressed in Adair's study. The strength of the proposed secondary minimum interaction was not determined by analyzing the hydrodynamic shear forces required to promote breakup of the aggregates. Aggregate bond strength measurements as a function of particle size were suggested since the magnitude of the secondary minimum increases as a function of the radii of the interacting particles. The increased likelihood of secondary minimum coagulation with increasing particle size may have important implications to stone disease since it has been reported by Robertson [Rob69] that stone forming individuals have particles significantly larger in size than non-stone formers.

2.3.3 Heterocoagulation

Heterocoagulation is the aggregation among particles of different materials. We are not aware of any investigators that have addressed this potential mechanism for stone formation. However, there have been a number of investigators [Bar78, Der54, Kuo80, Mat81] within the colloid chemistry community that have developed the theoretical and practical framework for a study of heterocoagulation. The basis for heterocoagulation is the difference in surface charge polarity of particles comprised of different materials. Thus, a positively charged COM particle may be electrostatically (as well as through the van der Waals interactions) attracted to a negatively charged hydroxyapatite (HAP)

particle. However, even if the surface charge on particles of dissimilar materials are the same, the van der Waals attractive forces may be strong enough to promote heterocoagulation (as well as homocoagulation).

Within the human nephron a variety of potential combinations exist that may lead to heterocoagulation. These interactions include, COM-HAP, COM-HU (uric acid), COM-NH_4U (ammonium urate), COM-COD (calcium oxalate dihydrate), COM-E.coli and other bacteria, and COM with various macromolecules. Heterocoagulation will be reversible only when the sign of the surface charge is made the same for all particles and is sufficient to overcome van der Waals interactions. The sign of the surface charge and corresponding solution conditions that will promote or inhibit heterocoagulation need to be evaluated for each system. It has been predicted that epitaxy of the high temperature form of COM and HAP is unlikely because of incoherent crystal structures [Man81]. However, heterocoagulation can explain the presence of HAP with COM in a stone.

Heterocoagulation has not been addressed for material systems relevant to urolithiasis. Preliminary experiments have been conducted in our laboratory to determine the conditions in which particles composed of various materials will be likely to heterocoagulate. An obvious starting point in this initial evaluation is to examine the effect of the polarity of the zeta potential for the various materials as a function of relevant solution conditions. The zeta potential data for COM and HU are summarized in Figure 2.8(A) as a function of Ca^{2+} and $C_2O_4^{2-}$ concentration. The COM data are from Curreri et al. [Cur79a] and incorporate the solubility product for COM in the Ca^{2+} concentrations. The uric acid data from Adair et al. [Ada88] are given as a function of Ca^{2+} or $C_2O_4^{2-}$. COM has a point of zero charge (pzc) at pCa = 5.2 ($Ca^{2+} = 6.3 \times 10^{-6}$ M) with COM having negatively charged surfaces above this pCa and positively charged surfaces at higher Ca^{2+} concentrations. Adair et al. [Ada88] showed that uric acid is negatively charged over a wide range of pH and Ca^{2+} and $C_2O_4^{2-}$ concentrations.

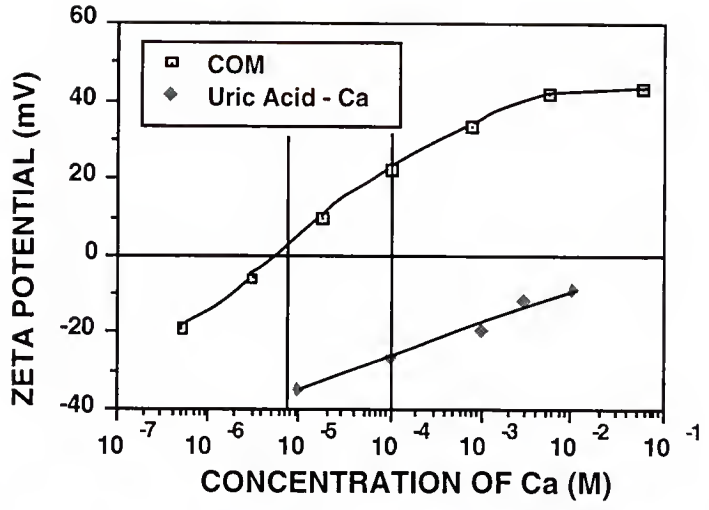

(A)

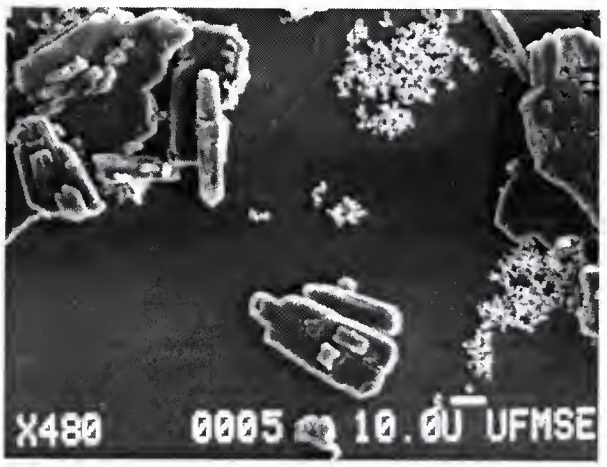

(B)

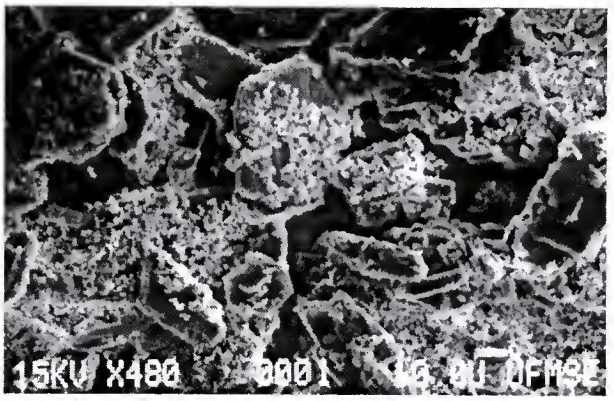

(C)

Figure 2.8. Heterocoagulation of COM with HU is predicted based on: (A) zeta potential determinations, (B) mixing of HU and COM at pCa ≤ 5 where COM and HU are both negatively charged, and (C) mixing at pCa = 4 where COM and HU are both oppositely charged (bar = 20 μm) [Ada95].

Thus, mixing COM and HU particles where pCa is less than 5.2 should promote heterocoagulation between the negatively charged HU and the positively charged COM. As shown in Figure 2.8(B) and 2.8(C), fine COM particles produced by the dimethyl oxalate decomposition adhere to the larger, prismatic HU particles when pCa=4. When COM and HU particles in saturated COM solutions are mixed with pCa=5, the fine COM particles have a greater affinity toward one another than the HU particles and heterocoagulation does not occur, as shown in Figure 2.8(C).

2.3.4 Polymer Bridging Flocculation

This mechanism takes place when there is insufficient polymer (or macromolecule) for full surface coverage on particles. This is the only aggregation mechanism that explains some ultrastructural observations of Boyce, Khan et al., and others [Boy68, Kha83a, Kha83b, Kha87, Mey82, Mey71, Pri86] on the role of matrix macromolecules in the microstructure and ultrastructure of the mature stone. Maximum flocculation takes place when one-half of the surface of a particle is covered by polymer [Son72, Hun86], as shown schematically in Figure 2.9. However, flocculation takes place anywhere between about one-tenth surface coverage to greater than 75 percent coverage. We are not aware of any studies relevant to urolithiasis that have addressed the role of flocculation in detail. Kok et al. [Kok90], Finlayson [Fin78a], and Robertson and Peacock [Rob85] have discussed this mechanism with other possible mechanisms of aggregation; but, the research emphasis has been on the prevention of aggregates by employing large concentrations of macromolecules or polymers [Coe91, Deg91, Rya81a, Rya84, Scu86a, Scu86b, Lan88, Lea77]. This mechanism can also explain the conflicting reports of inhibition versus promotion [Edy86, Cam89, Gro90]. Thus, macromolecular species such as uropontin, Tamm-Horsfall mucoprotein, and nephrocalcin may play a dual role: at sufficiently low concentration, aggregation is promoted through flocculation

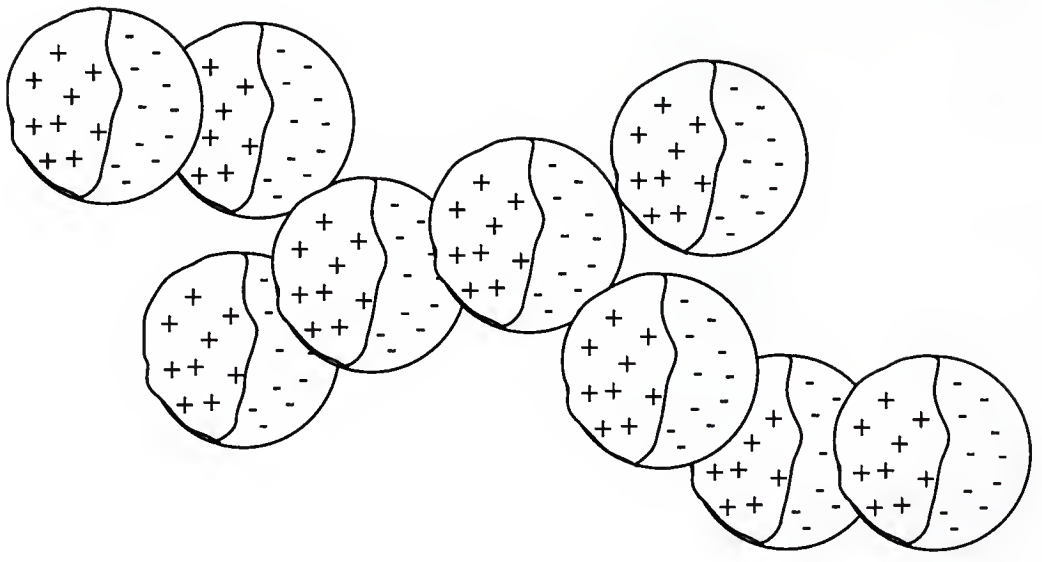

Figure 2.9. A schematic representation of patch charge flocculation whereby incomplete macromolecular coverage may create electrostatic shielding or opposite charge in the case of a charged polymer.

while at higher surface coverage, dispersion of particles is achieved through the protective colloidal effect of the macromolecular coating [Hou80, Son72].

Although there have been limited studies on flocculation with respect to urolithiasis, there have been a number of investigations on floc formation and hydrodynamic breakup because of its importance in wastewater treatment and other technologies [Dit82, Eis85, Gre81, Gre85, Ray87]. These studies provide a basis for evaluating the role of flocculation as an aggregation mechanism for COM and other relevant particles in urine. For example, an excellent starting point is to determine the macromolecular or polymer dosage for relevant urinary species required to achieve the maximum flocculation. The critical flocculation concentrations (CFC) for a particular macromolecule will indicate whether this mechanism is likely by comparison with its concentration range in urine.

In preliminary studies, we have examined a flocculant commonly used in mineral recovery. Polyethyleneimine (PEI) is a positively charged highly branched polymer molecule used by Pelton and Allen [Pel84] to produce positive charge on glass surfaces in their particle adhesion studies. It has been shown in preliminary studies, using the apparatus developed by Eisenlauer and Horn [Eis85], to evaluate the aggregation of freely flowing particles in suspension. This device has the advantage that flow rate and mode of flow (i.e., continuous versus peristaltic) can be varied. The commercial analogue to Eisenlauer and Horn's device, known as a photometric dispersion analyzer (Rank Brothers, Cambridge, UK), has been used extensively to monitor the flocculation of model systems. Initial experiments have demonstrated that fine COM particles flocculate at intermediate dosages of PEI. The relative degree of flocculation varies as a function of charge (as dictated by the concentrations of Ca^{2+} and $C_2O_4^{2-}$).

2.3.5 Flocculation of COM Particles by Phospholipids and other Intercellular Substances

Work by Khan, and Mandel and co-workers [Kha88, Man94] indicates that interaction of COM particles with phospholipids at either the epithelial surface of cells or with phospholipids liberated into the bulk solution by cell injury are important features in the formation of aggregates in the interluminal channel of the nephron. Flocculation by sparingly soluble, amphiphilic molecules such as the phospholipids forming a major component of the epithelial cell membrane have not been studied with respect to aggregation, but Mandel et al. [Man94] clearly show that adhesion of COM particles is important. The ability of phospholipids to adsorb to the surfaces of sparingly soluble inorganic particles and surfaces is well established as are the forces arising from the interaction of phospholipid monolayers on mica and similar surfaces based on force balance work by Israelachvili and others [Isr92]. Thus, one would expect phospholipids to demonstrate an effect similar to macromolecules or polymers capable of promoting flocculation. However, the interparticle strength of particles flocculated in either freely flowing suspensions or at surfaces containing phospholipids (i.e., cell membranes) would be expected to depend on the concentration of phospholipids and the efficiency of adsorption of such species to COM surfaces.

2.3.6 Adhesion of Particles at Surfaces

Adhesion is an important mechanism in the formation of fixed kidney stones and is dependent on the adhering materials and the suspending medium. One of the first theories of adhesion between solid particles and surfaces was given by Krupp [Kru67], where he defined three classes of interactions:

I. Class I interactions include long range attractive interactions resulting from van der Waals forces and electrostatic forces.

2. Class II interactions are given by short range attractive interactions such as chemical bonds and hydrogen bonds.

3. Class III interactions involve interfacial reactions occurring at elevated temperatures including sintering effects, diffusive mixing, and mutual dissolution and alloying.

Class III interactions may also be important at lower temperatures for polymer or macromolecular diffusive mixing. Other important forces also exist that were not directly addressed by Krupp. These forces are solvation forces, structural forces, or in a water medium called hydration forces. These short range forces involve ordering of the solvent medium to cause either attraction or repulsion between particles depending on the hydrophobic/hydrophilic nature of the solids in suspension [Hor90, Isr92].

All of the aforementioned interactions may apply during adhesion; however, Krupp [Kru67] believed that van der Waals forces and electrostatic forces are the dominating long range attractive forces between adhering materials. Krupp thought that only under ultra-high vacuum or extremely pure systems would primary chemical bond formation take place due to the saturation of bonding sites by contaminants under ambient conditions. Kallay et al. [Kal87] was also of the opinion that van der Waals interactions and electrostatic interactions were dominating, but they furthermore suspected that short range repulsion played a role in the total interaction energy of adhering bodies, citing solvation forces, as did Israelachvili [Isr92] and also electron cloud repulsion. These short range forces were said to act at separation distances on the order of the distance of closest approach of the two surfaces. Theoretical models for both long range interactions [Der41, Ver48, Hog66, Wil93] and short range [Isr92, Kal87] interactions are available for varying surface geometry interactions and will be discussed later.

The study of adhering materials is fundamental and very broad in application. The adhesion of many materials by several researchers has been documented [Vis76]. For

example, the adhesion of Fe_2O_3 to a glass substrate and a glass substrate covered by a layer of gelatin [Ryd95], red blood cells to glass [Moh74], human fibroblasts to glass [van92], submicrometer particles to silicon [Bus93], and bacteria to glass [Bus92] have all been measured. As observed, applications of the adhesion measurement range widely.

Just as a number of applications are in need of the adhesion measurement, a number of techniques can be used to measure the adhesion of solid particulate material to solid surfaces. In past studies researchers have used many techniques to evaluate adhesion [Cor66, Zim82]. These techniques include a rotating disc [Kri94], a packed column [Kal87], a centrifuge method [Kor60], a vibrating method [Der61], a surface force apparatus [Isr78], and a hydrodynamic method that utilizes parallel plates [Pel84, Pel82] to name only a few. The most recent technique for measuring the force with which a particle adheres to a surface utilizes the scanning probe microscope (SPM) [Duc91]. Other adhesion measuring techniques exist and are used but are best suited for specific material systems, much like the techniques mentioned above. Further discussion will be limited to only the hydrodynamic parallel-plate and adhesion measuring technique.

Another approach in evaluating the bond strength of particles adhering to a surface is to determine the hydrodynamic shear force required to remove particles. Pelton [Pel84], Busscher [Bus84], Matijevic [Mat80, Mat81], Owens [Owe87], and others [Ols78] have used this approach to evaluate thermodynamic models for the attachment of particles to surfaces. The balance of forces proposed for a COM particle attached to the epithelium is shown schematically in Figure 2.10. The shear stress at the wall (τ_W) is given by [Owe87, Esk68]

$$\tau_W = \frac{dP}{dl} b \tag{2.4}$$

where τ_W is the shear stress at the wall, P is the hydrostatic pressure drop across the conduit of length, l, and wall separation, b.

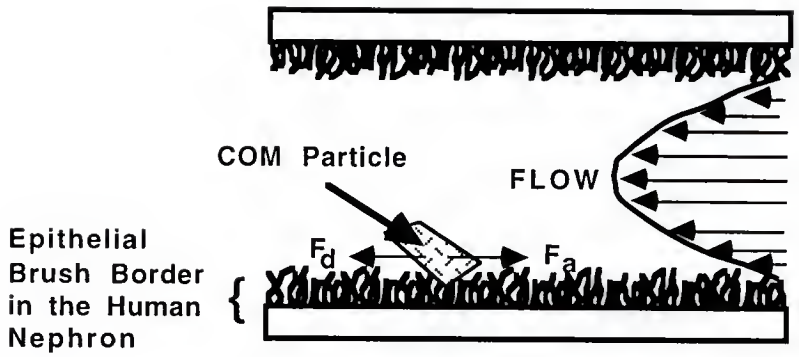

Figure 2.10. Scenario depicting the balance of hydrodynamic forces (F_d) and adhesive forces (F_a) acting on a COM particle bound to the brush border in the human nephron.

Determination of the adhesion strength for particles adhering at surfaces is of fundamental importance in deducing whether the fixed particle mechanism for stone formation proposed by Finlayson and Reid [Fin78b] is reasonable within the hydrodynamic system of the nephron. Kok and Khan [Kok92] recently re-evaluated the hydrodynamics in the kidney and determined that it is not possible to have a stone occurrence with out the aid of adhesion.

Riese, Mandel, and coworkers and others [Man94, Rie92, Rie88, Yam96] have shown *in vitro* attachment of COM crystals to inner medullary collecting duct (IMCD) epithelial cells of the rat animal model in the static case (i.e., without the presence of flow). They also proposed that perturbations in the cell membrane structure with a loss in membrane polarity can enhance crystal attachment [Rie92]. Lieske et al. [Lie95, Lie96a] has also measured adhesion of COM to MDCK cells and to monkey renal epithelial cells in a similar manner to Reise et al [Rie88]. They determined that cell anionic sites can be blocked by specific cations [Lie96a] and the positive sites on a COM crystal may be blocked by specific anions [Lie95] thereby minimizing adhesion. Bigalow et al. [Big97] recently demonstrated that COM crystal attachment to IMCD cells was effected by the cell membrane fluidity. Changes in temperature, cholesterol content, and cell culture time which increase cell membrane fluidity also increase the ability of COM crystals to bind to the membranes leading the researchers to conclude that a long range arrangement in the membrane is created to match the COM crystal structure [Big97]. *In vivo* crystal attachment to epithelial cells in the rat animal has been demonstrated by Khan et al. [Kha82]. Renal injury has also been implicated in fixed stone formation [Man91, Gil79, Kha84]. Khan [Kha82, Kha95a] has discussed that after attachment of a crystal to the epithelial cell surface that injury to the cell may occur but may not always occur.

A few different results may ensue crystal attachment to the epithelial cell. If the cell dies, the cell and attached crystal may be washed away in the urine flow. The cell

may envelope the crystal and continue to function normally [Lie92, Lie93, Lie94, Koh96] with no further growth of the crystal. However, if epithelial cell injury has occurred, basement membrane proteins may be accessible to adhere to COM crystals by sloughing of the cells leaving behind the exposed underlying architecture, the basement membrane. The basement membrane is a layer of proteins that underlies the epithelial sheet and will be discussed subsequently in more detail.

Depending on the extent of injury, other proteins common to the extracellular matrix found below the basement membrane may also be accessible for attachment to COM crystals. Khan et al. [Kha84] demonstrated the association of crystals to fibrillar macromolecular structures by scanning electron microscopy (SEM). Khan [Kha95a] has also shown crystals passing through the basement membrane into the extracellular space near the papillary tip as shown in Figure 2.11.

Researchers have shown the attachment of COM crystals to epithelial cells and fibrous proteins characteristic of those found in the basement membrane and extracellular matrix, yet the importance of these individual materials in kidney stone formation with respect to COM crystal adhesion is not known. The necessity to determine the important materials most responsible for COM crystal adhesion will allow researchers to focus their interests to those more important materials in the search for a possible cause and therefore relief from kidney stone formation.

2.4 The Human Kidney

The human kidney contains approximately 1 million nephrons which absorb nutrients and water back into the body after being filtered out of the blood by the renal glomeruli [Ham74]. The nephrons consist of tubules through which the waste is collected. As the waste products travel further down the length of the nephron, the waste becomes concentrated and supersaturated conditions may exist allowing precipitation of crystallites, such as COM, to occur. Figure 2.12 shows a nephron.

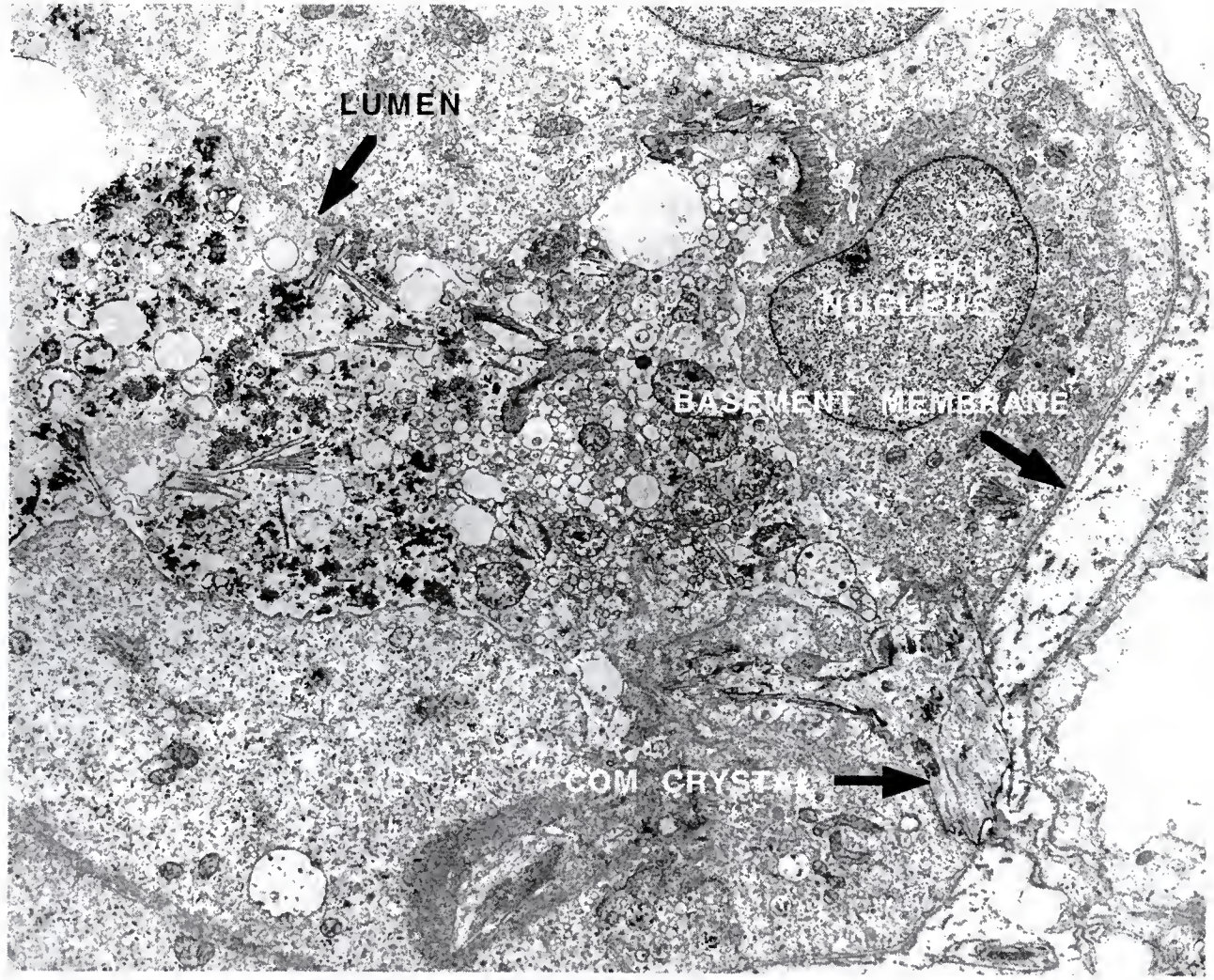

Figure 2.11. A scanning electron photomicrograph of a tubule cross section in the rat demonstrating association of a COM crystal with the basement membrane. (Courtesy of S.R. Khan).

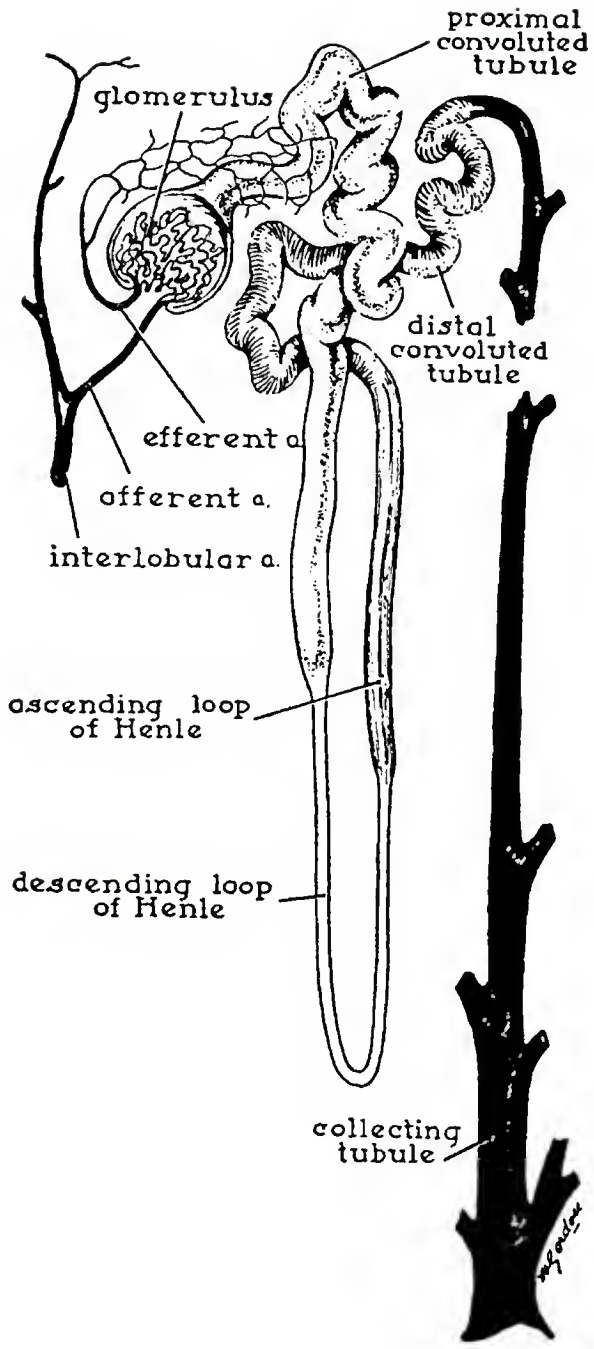

Figure 2.12. A schematic illustration of a human nephron [Ham74].

The renal tubules are lined with epithelium. Underlying the epithelial cells is a structure called the basement membrane which is a continuous thin mat of specialized extracellular matrix that functions as a support, a molecular sieve, and a cell regulator [Yur90].

The basement membrane consists of the basal lamina and the lamina reticularis. The basal lamina is also divided into two different sections, the lamina rara and the lamina densa. The basal lamina is essentially a mat of collagen type-IV with specific molecules on each side of the mat that help it bind to adjacent cells or matrix materials [Alb89]. Although the composition of the basal laminae varies from tissue to tissue, one of the molecules always found in the basal lamina is laminin. Another molecule often found in the basement membrane, in particular the lamina densa [Ino94], is fibronectin. The structure below the basement membrane is the extracellular matrix, which is primarily made up of fibrous proteins in a hydrated polysaccharide gel [Alb89]. Collagen type I is a fibril forming collagen found in skin, tendon, bone, intestine, uterus, and surrounding organs [Kuc92]. Figure 2.13 is a schematic representation of the renal epithelial cells, basement membrane, and extracellular matrix showing there relative positions in the tubule wall.

2.5 Characterization Techniques

2.5.1 Electrokinetic Measurements

Charge characterization at the solid-solution interface is very important when attempting to discern mechanisms of adhesion. As described in section 2.2.1 of this chapter, charged materials when immersed in water are surrounded by strongly adsorbed ions, called the Stern layer, and by a gradient ionic cloud, called the diffuse part of the double layer, as shown in Figure 2.3. Electrokinetic measurements are useful in determining the electrostatic potential, often called the zeta potential, ζ, at the boundary

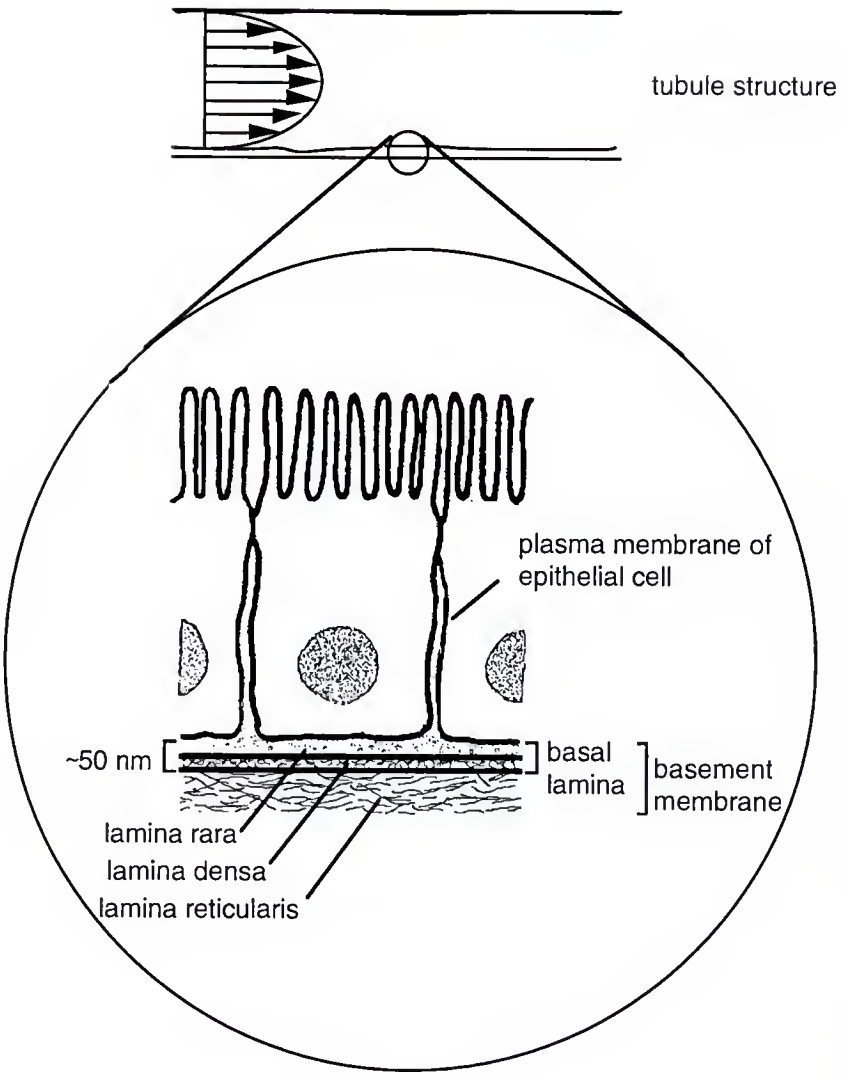

Figure 2.13. A schematic representation of a tubule wall found in a kidney.

between the strongly adsorbed layer and the beginning of the diffuse double layer as schematically depicted in Figure 2.5. Electrokinetics is the measurement of the movement of one phase with respect to another phase in which a charged boundary between the two exists. Two types of electrokinetic measurements, electrophoresis and streaming potential, are described below.

2.5.1.1 Electrophoresis

Colloidal particles immersed in water can move under an applied electric field as a result of the charge on the particle surface as shown in Figure 2.14. The electrophoretic mobility, μ_E, is defined as the particle velocity per unit static electric field. The mobility can be determined by measuring the velocity of a particle under an applied electric field. The mobility is related to the electrical potential at the shear plane surrounding the particle. The shear plane is defined as the boundary between the bulk solution, where the ions are free to move, and the inner layer of strongly adsorbed ions which move with the particle under an applied electric field. The corresponding zeta potential, ζ, is calculated from the experimentally determined electrophoretic mobility, u_E, according to the Smoluchowski equation [Hun81]

$$\zeta = \frac{\eta u_E}{D\varepsilon_o}, \tag{2.5}$$

where η is the viscosity of the solution, D is the dielectric constant of the solution, ε_o is the permittivity of free space. A number of techniques exist to determine the electrophoretic mobility under an applied electric field such as a simple optical method, electrophoretic light scattering method, and electroacoustics to name a few.

2.5.1.2 Streaming Potential

The charge at the surface or the more commonly accepted charge at the Stern layer, the zeta potential, can be determined by measuring the streaming potential

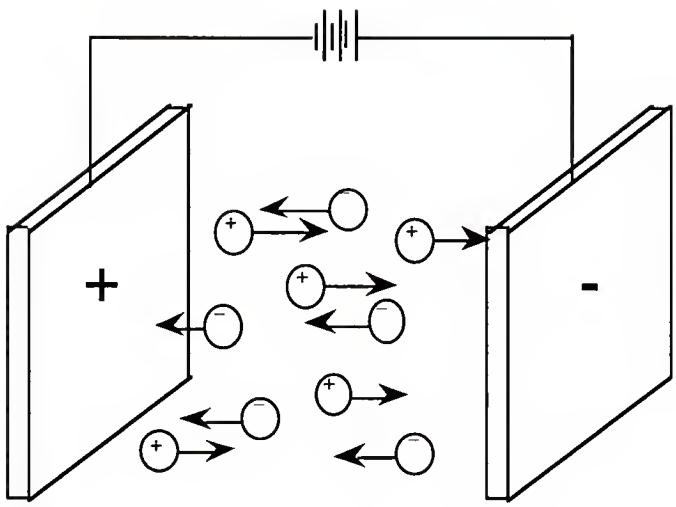

Figure 2.14. A schematic representing charged particle movement in an applied electric field to determine electrophoretic mobility.

associated with a surface. Streaming potential is the potential generated when a fluid is forced through a capillary. The hydrodynamic pressure forces the mobile charges in the double layer in the direction of flow. The accumulation of charge at one end of the capillary creates an electrical potential across the capillary as demonstrated in Figure 2.15. In the case of glass or fused quarts, the charge on the surface is negative; therefore, the mobile charges will be primarily positive causing a positive current in the direction of flow. The streaming potential can be measured with a high impedance voltmeter as a function of pressure. If the potential is measured as a function of pressure, the Smoluchowski equation can be used to calculate the zeta potential [Hun81]

$$\zeta = \frac{4\pi\lambda_o E_s}{\varepsilon P}. \tag{2.6}$$

If the usual mixed units are used, the equation is

$$\zeta(\text{mV}) = \frac{0.1\eta(\text{poise}) \times \lambda_o(1/\Omega \cdot \text{cm}) \times 100}{8.854 \times 10^{-12}(\text{C}/\text{V} \cdot \text{m}) \times \varepsilon} \frac{E_s(\text{mV})}{P(\text{dyne}/\text{cm}^2)}$$

where ζ and E_s are the zeta and streaming potentials, respectively, both measured in mV, P is the pressure drop across the capillary in cm Hg, the conductivity of the elution, λ, is in units of $\Omega^{-1}\text{cm}^{-1}$, and ε is the dielectric constant of the elution.

Equation (2.6) is only valid for solutions in which all or almost all of the current generated due to streaming is carried through the bulk liquid. For solutions having ionic concentrations less than 10^{-3} M, the need to account for surface conduction is important [Rut47]. At low electrolyte concentrations, a large part of the current may be carried through the double layers near the capillary walls because of the higher charge density in that region. Equation (2.6) becomes [Hun88]

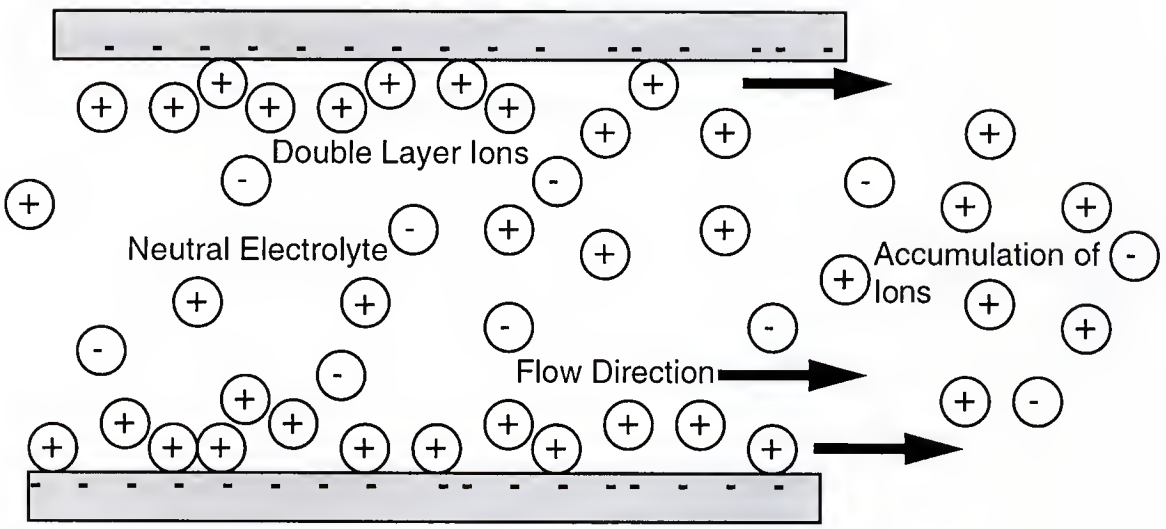

Figure 2.15. A schematic representation of the flow of ions under an applied hydrodynamic pressure which generate the potential across the capillary or streaming potential.

$$\zeta = \frac{4\pi(\lambda_o + 2\lambda_s/r)E_s}{\varepsilon P} \tag{2.7}$$

where the term $2\lambda s/r$ is the specific surface conductivity and r is the capillary radius or the distance between plates for a flat plate system. The variable λ_s is the conductance of a square section of material of unit area and constant thickness measured in Ω^{-1}. Briggs [Bri28] suggested a simpler procedure for correcting for surface conduction. The procedure involves measuring the resistance of the liquid in the capillary at low ionic concentration, R_{exp}, and compare with the value of resistance expected from measurements at high ionic concentration, R_{calc}, where surface conduction can be expected to be negligible. Equation (2.7) becomes

$$\zeta = \frac{4\pi\lambda_o E_s}{\varepsilon P} \cdot \frac{R_{calc}}{R_{exp}} \tag{2.8}$$

The general effect of accounting for surface conduction will give an increase in magnitude of the calculated value of zeta potential at low ionic concentration conditions.

Ball and Fuerstenau [Bal73] performed an extensive review of the streaming potential literature and found that the measurement should be performed over a sufficiently wide range of pressures to obtain an accurate estimate of the slope, E_s/P, the obtained slope should be linear, and the intercept of the slope should be zero. Ball and Fuerstenau [Bal73] and Hunter [Hun88, Hun93] have all stressed the importance of the linear dependence of the streaming potential, E_s, on the applied pressure, P. The linearity of the plot of streaming potential vs. applied pressure is a necessary first step to determine experimental reliability; however, unless surface conduction is accounted for, linearity does not ensure accuracy of the resulting zeta potential [Hun88]. The finite intercept of the slope is an indication of an asymmetry potential or rest potential which is said to be a function of the electrodes, including their preparation, treatment, and cleaning,

and of the electrolyte and its concentration [Bal73]. No electrode system, Pt, Au, Ag/AgCl, Ag/AgI, or calomel, has been found to eliminate the asymmetry potential completely.

Many authors have developed methods for eliminating asymmetry or rest potentials [Hun62, Mar30, Bul35, Hor77]. Hunter and Alexander [Hun62] found that the rest potential could be nullified when the liquid was stationary. Martin and Gortner [Mar30] and Bull [Bul35] avoided an asymmetry potential by working at high applied pressures where the asymmetry potential is negligible relative to the streaming potential. Horn and Onoda [Hor77] devised a resistance-capacitance (R-C) circuit to store the asymmetry potential in a large capacitor and subtract the potential from the streaming potential when flow begins.

2.5.2 Scanning Probe Microscopy

Scanning probe microscopy (SPM) offers a versatile range of techniques which can be employed to acquire information about a material surface. Topographical information can be acquired using Contact Mode Atomic Force Microscopy (AFM), TappingMode™ AFM, and Non-contact AFM. Other techniques can also acquire topographical information.

Contact Mode AFM measures topography by sliding the probe tip across the sample surface in air or in fluid. A laser is focused on the back side of the probe tip also known as the cantilever as shown in Figure 2.16. The laser reflects from the cantilever to a mirror onto a photodetector. The sample is mounted on the piezoelectric scanner which rasters the sample under the tip and surface interactions between the sample and tip cause the cantilever to deflect. Any motion of the cantilever is registered by the photodetector. The position of the laser spot is determined by the electronic circuitry which generates a voltage difference between the photodiode segments and a topographical image is the result.

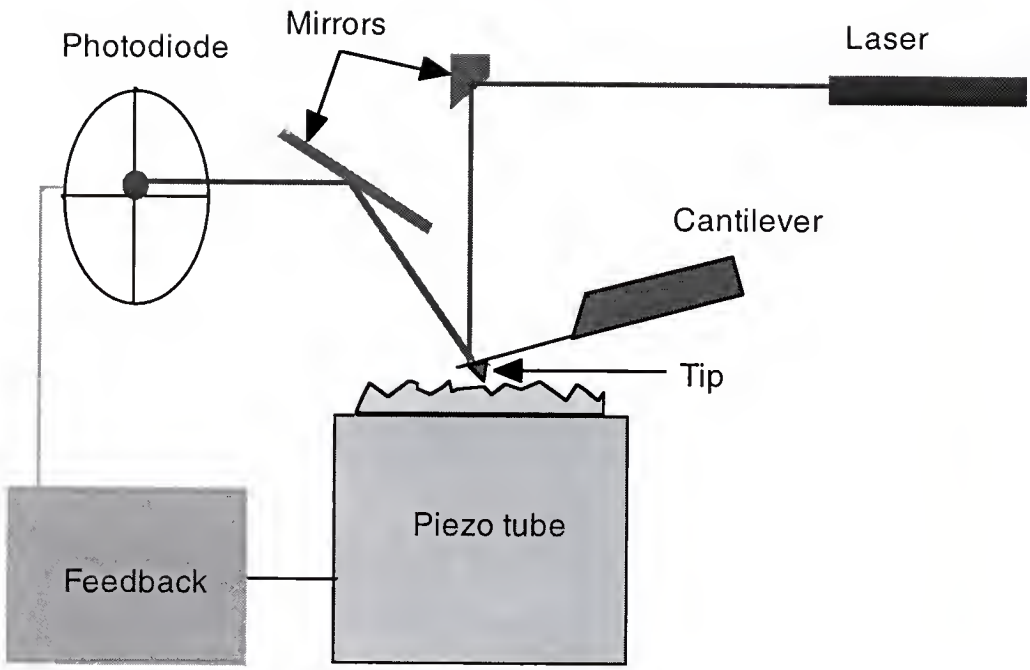

Figure 2.16. A schematic diagram of the SPM.

2.5.3 Scanning Electron Microscopy

Scanning electron microscopy (SEM) is a useful tool to analyze surface topography of materials. A focused electron beam is rastered across the sample exciting electrons in the atoms of which the sample is composed. As a result, both secondary and backscattered electrons are produced from the sample. A detector measures the intensity of the electrons versus position and displays this information on a cathode ray tube. Secondary electron contrast is due to the dependence on electron yield on the topography and the depth of secondary electron emission is about 100 Å. Because the sample must be electrical conductive to be analyzed using SEM, the samples need to be sputter coated with Au/Pd.

2.5.4 Fourier Transform Infrared Spectroscopy

Infrared spectroscopy (IR) is a useful tool to study polymers and organic materials as well as inorganic materials. Fourier transform infrared spectroscopy (FT-IR) uses the principles of interferometry to study bond vibration in materials. Electromagnetic radiation in the infrared region (7.8×10^{-5} to 0.1 cm) is passed through or reflected off the sample. The radiation excites molecular bonds to higher vibrational levels, absorbing energy. The absorbed energy corresponds to particular vibrational frequencies characteristic of a molecule or molecular group. Therefore, the IR technique is useful in determining unknown materials, determining bond orientation, and quantitative and qualitative analysis of bond types [Mar86].

Attenuated total reflectance (ATR) spectroscopy also called internal reflection spectroscopy (IRS) may be the most widely utilized adaptation of IR to study inorganic material surfaces. ATR is performed by coupling the incident electromagnetic radiation into an IR transparent crystal of high refractive index, as shown in Figure 2.17. When the beam reaches the interface between the crystal and the materials to be analyzed, it is

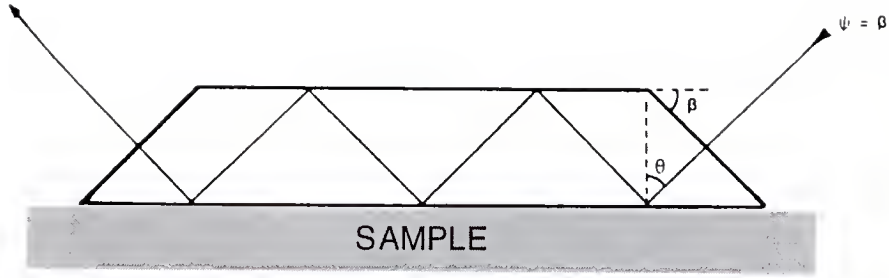

Figure 2.17. Multiple internal reflection within the internal reflection element which is coupled to the sample.

internally reflected. However, 100% internal reflection does not occur and some part of the wave travels into the sample material to a depth governed by the wavelength of radiation, the IR crystal, and the refractive index properties of the sample [Knu85]. Figure 2.18 is a plot of wavenumber vs. sampling depth for a thallium bromide-thallium iodide (KRS-5) IR crystal having a 45° incident angle coupled to a sample assumed to have an index of refraction of 1.5. As can be seen from Figure 2.18, the sampling depth increases as function of increasing wavelength (decreasing wavenumber) over the mid-infrared region.

2.5.5 Particle Size Determination

Many techniques exist to measure particle size. These techniques include microscopy, sedimentation methods, electrical pulse counting, light scattering methods, hydrodynamic methods, and electroacoustics. Each of these techniques has its advantages and limitations, which may be dependent on size, density, optical properties, or other parameters.

Electrical pulse counting is able to count the number of particles in a known amount of solution by drawing the suspension through a very small orifice that has an electrode on either side of it as shown schematically in Figure 2.19 [Hun93]. When a particle passes through the orifice, interference with the current flowing between the two electrodes occurs and the resistance changes. The number of changes in current and the magnitude of change are recorded. Because the change in current is proportional to the volume of the particle passing through the orifice, the result is a value of particle size when calibrated against a dispersion of known particle size. The number of current changes acts as a particle counter generating a particle size distribution.

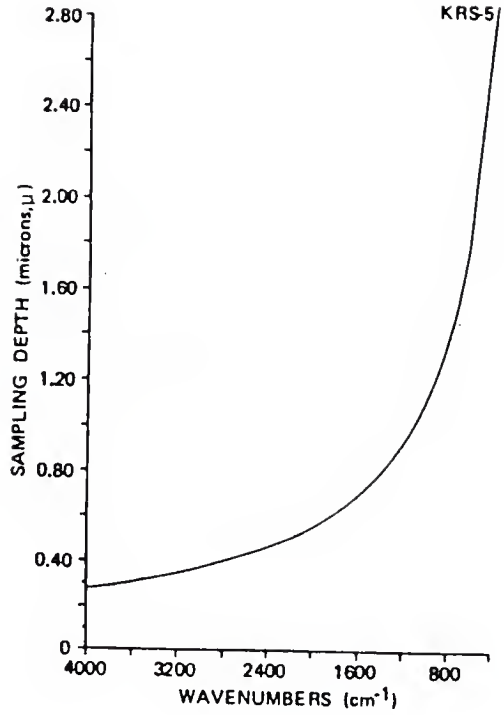

Figure 2.18. Sampling depth as a function of wavenumber for the KRS-5 internal reflection element having a 45° incident angle [Knu85].

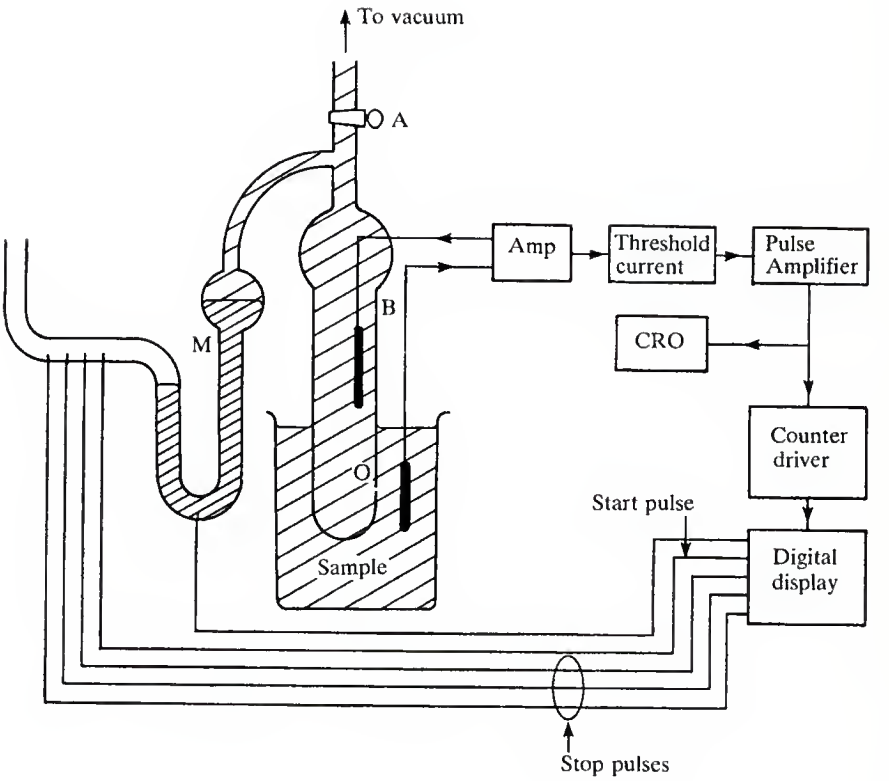

Figure 2.19. A schamatic diagram of a Coulter counter, electrical pulse counting instrument [Hun93].

2.5.6 X-Ray Diffraction

X-Ray diffraction (XRD) is a tool used to investigate the arrangement of atoms in a crystal. XRD is useful for identifying compounds in crystalline materials, determining crystallographic information of metals, ceramics, and polymers, and performing quantitative phase analysis. A monochromatic or near monochromatic beam of x-rays is focused on a specimen. The incident x-rays are diffracted by the lattice atoms in the crystal according to Bragg's Law [Cul78]

$$n\lambda = 2d\sin\Theta, \tag{2.9}$$

where n is the order number, λ is the wavelength of the incident x-rays, d is the interplanar spacing, and Θ is half of the angle of diffraction. A scintillation detector is moved through some angle at a given rate and the number of counts or intensity is recorded The resulting pattern is a plot of x-ray intensity vs. angle (2Θ) measured with respect to the incident beam. Because the crystal structure is periodic, the in-phase scattered electrons create an increase in intensity.

CHAPTER 3
DEVELOPMENT AND CHARACTERIZATION OF MODEL COM PARTICLES

3.1 Introduction

Calcium oxalate monohydrate (COM) is the most thermodynamically stable form of calcium oxalate and is a major component of human calcium oxalate calculi [Pri47, Deg81a]. Stone formation in the urinary tract takes place opportunistically with an unfortunate, simultaneous convergence of factors that may be achieved by several pathways for a stone to form [Bro92, Ada95]. Many theories have been proposed to explain the critical factor(s) responsible for the formation of urinary stones [Bro92, Ada95, Fin78a, Fin84, Rob86]. Kidney stone disease may take place as a consequence of injury, supersaturation (particularly hyperoxaluria), nucleation, and growth mechanisms, which may include adhesion on epithelial cell surfaces and aggregation. All of the previously mentioned factors may play a role in contributing to stone formation. Nonetheless, stone formation remains an idiopathic disease with no one risk factor providing an obvious cause for stones in most cases. However, both the *in vivo* and *in vitro* evidence indicates that the presence of particles is a necessary but insufficient condition for stone formation. From this perspective, the formation and presence of crystallites may be a typical renal function directed at concentrating oxalate for more effective, irreversible elimination from the body.

The abnormal stone-forming condition results from the aggregation and further growth of such pre-existing crystallites [Fle78, Rya81a, Ada81, Deg91, Edy86, Edy87a, Har86a, Har86b, Kok90, Rob85, Scu86a, Scu86b]. Indeed, it has been found that while the solid phase in the urine of normal individuals is made up mainly of individual crystals,

large aggregates are often found in stone formers [Fle78]. Therefore, both crystal growth and aggregation are generally regarded as important steps in the formation of calcium oxalate renal stones [Fle78, Rya81a]. Numerous studies have shown that the aggregation and/or adhesion of COM particles may potentially lead to the ultra-structures typical of kidney stones [Ada81, Deg91, Edy86, Edy87a, Har86a, Har86b, Kok90, Rob85, Scu86a, Scu86b]. Kok et al. [Kok90] reported that precipitation alone of COM particles cannot account for the large size particles necessary to cause blockage of the urinary tract. Aggregation is therefore the only possible mechanism whereby a stone may reach a size as large as 0.64 cm, the maximum size that can pass through an average adult male urethra [Fin78b].

Aggregation is the process whereby crystals bind one to another to produce large clusters. The actual mechanism(s) of aggregation within the biophysical environment of the human kidney is uncertain; however, Adair et al. [Ada95] have classified six aggregation mechanisms acting alone or in concert which may contribute to stone formation: (a) coagulation in simple electrolyte solutions; (b) secondary minimum coagulation; (c) heterocoagulation of particles with different surface charge polarity; (d) polymer bridging flocculation; (e) secondary nucleation and growth; and (f) flocculation via immiscible amphiphilic molecules. The previously mentioned mechanisms, which are summarized in Figure 3.1, stress the importance of knowing the environmental conditions in the urinary system for formation of calcium oxalate calculi. For example, citrate can retard the crystallization of stone-forming calcium salts by two broad means [Cha91]. First, citrate complexes calcium and reduces the ionic calcium concentration available for precipitation in urine, thereby lowering the supersaturation. Second, citrate can directly inhibit crystallization of both calcium oxalate and calcium phosphate at the growing crystal-solution interface. Thus, citrate has been shown to inhibit spontaneous precipitation of calcium oxalate and to retard agglomeration of pre-formed calcium oxalate crystals. Citrate is believed to also have a modest inhibitory effect against crystal growth

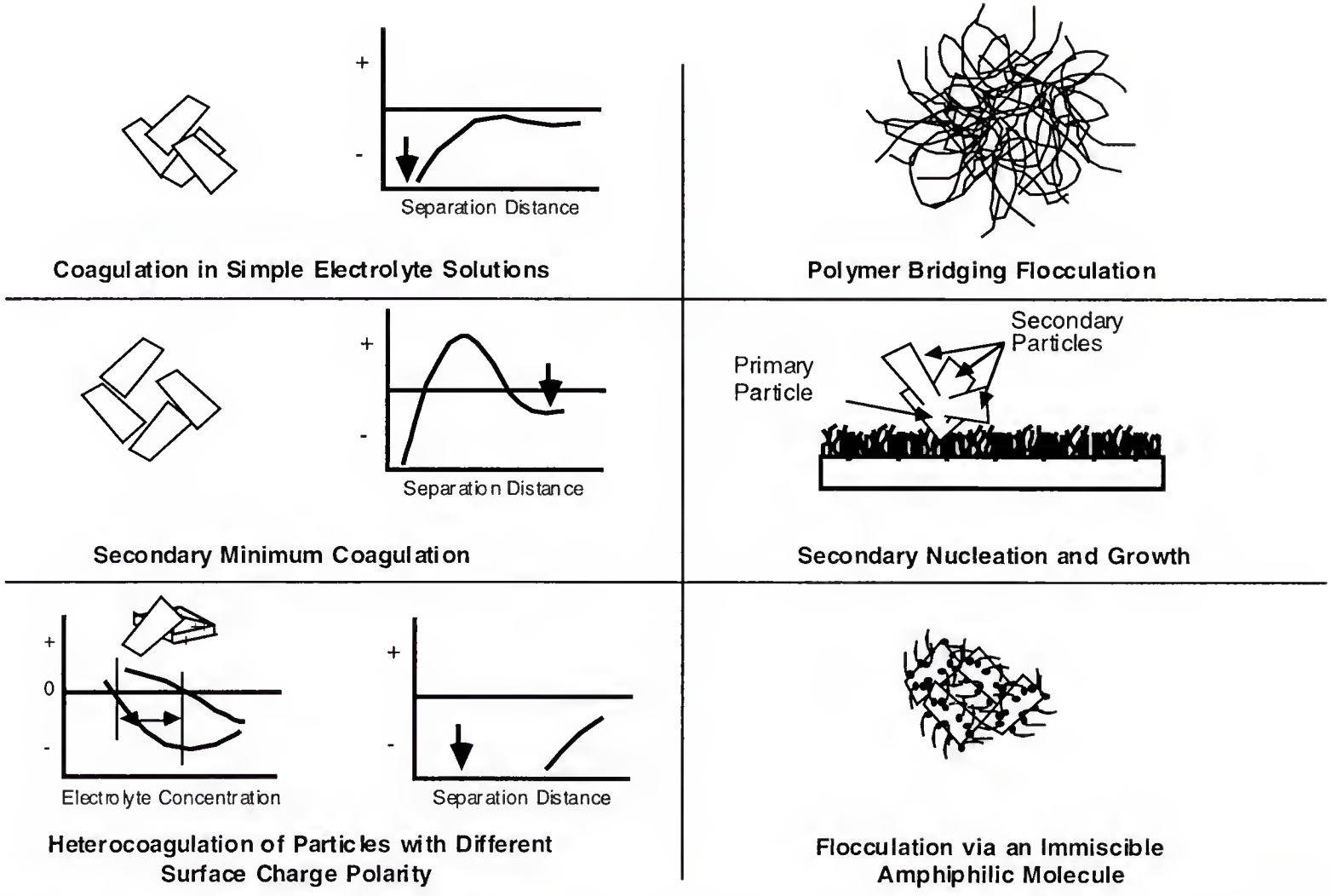

Figure 3.1. Possible aggregation mechanisms for particles in the urinary environment (from Adair *et al.* [Ada95]).

of calcium oxalate. Cody and Cody [Cod94] reported habit modification of COM crystals grown with citrate. Interpenetrating crystals grown in distilled water without citrate have sharply-angled tips and are flattened parallel to the (010) face whereas crystals grown with citrate have rounded tips and are flattened on the $(10\bar{1})$ face.

Few papers have dealt with the theoretical equilibrium shapes of COM crystals synthesized under different conditions or the atomic structure at specific faces [Deg91, Cod94]. Furthermore, little, if anything, is known at the atomic-molecular level about the interaction between COM particles and important species such Ca^{2+}, $C_2O_4^{2-}$, citrate, dicitrate, and urea, which are common in the urinary system and known to play a role in stone disease. Deganello's work [Deg91] is an exception to the lack of data on the interaction between some species and COM crystals. Adsorption of nephrocalcin, a protein found by Nakagawa and co-workers [Nak83, Nak87] in human urine, even at the lowest concentration tested, affects the habit while also inhibiting the growth of COM. The nephrocalcin protein promotes the preferential development of the $(10\bar{1})$ faces to such an extent that the length to width ratio of the crystals decreases by approximately a factor of three. In the course of this process, the apical planes eventually disappear and the size of the crystals decrease. Diminution of crystal size eventually becomes extreme when nephrocalcin reaches a concentration between 1 to 2×10^{-5} M.

Mandel [Man94] reported that the molecular surface structures on the prominent crystal growth faces of COM are very important in determining potential long-range molecular bonding interactions between the crystals and the lipid-rich regions in the inner medullary collecting duct (IMCD) cell plasma membrane. Mandel [Man94] also reported on epitaxial matching calculations for the high temperature form of COM, calcium oxalate dihydrate (COD), hydroxyapatite (HA), and uric acid (UA) crystal lattices against the dimensional repeating lattice of phospholipid headgroup structures. The Mandel study suggests that COD-COM epitaxy may be important relative to COD-lipid interactions in crystal attachment and stone development. Therefore, the molecular modeling between

specific surfaces of the COM crystal and these additives provide important insight for specific adsorption sites on COM surfaces, and the growth and aggregation mechanisms of COM crystals in the urinary system. Other research suggesting the crystallographic importance of COM was performed by Habeger et al. [Hab97]. A crystallographic dependence of COM crystals on adhesion to fused quartz glass substrates was observed. A variation in electrostatic charge as a function of crystallographic habit on the theoretical COM surface has been used to justify the differences in adhesive strength observed [Hab97].

In the current work, morphological forms of COM crystals synthesized in different conditions have been studied by using the commercial computer programs, SHAPE© and ATOMS©. The computer program SHAPE© has been used to determine the face indices of the synthesized COM crystals and generate the equilibrium shape as a function of central distance. The computer program ATOMS© has been used to generate the surface atomic structure of COM crystals as a function of habit plane.

Certain characteristics in a particle system are desirable to rigorously study theoretical growth and aggregation, and adhesion mechanisms. Ideally, the particles should be spherical. If spheres cannot be produced, a crystallographically definable morphology should be produced so that the habit planes can be identified. The theoretical study of growth and aggregation depends on well-defined particle morphologies. Unfortunately, COM has a monoclinic crystal structure whose inherent asymmetry does not lend itself to the formation of spherical particles. Therefore, the individual COM particles should be at least uniform with narrow particle size and shape distributions. Several different particle size ranges is also desirable. Thus, the objective in the current work is to prepare COM particles by several different methods followed by careful characterization to deduce the habit planes and atomic surface structure. Lastly, characterization of the particles having the most consistent COM morphology will be conducted.

3.2 Preparation and Characterization of Calcium Oxalate Monohydrate Particles under Different Conditions

Reagent grade chemicals were used in all precipitation studies without further purification. All solutions were prepared with deionized water (specific conductivity less than 10 μmho•cm^{-1}) which was provided by a Milli-Q high purity system (Millipore Corporation, Bedford, MA) and were passed through a 0.2 μm filter. For identification purposes, precipitated COM particles were designated by the negative logarithms of the initial Ca^{+2} and $C_2O_4^{-2}$ molar concentrations, respectively (e.g., particles prepared from 10^{-3} M Ca^{+2} and 10^{-3} M $C_2O_4^{-2}$ were designated "33" particles).

3.2.1 COM particles ("33" particles) without seeds

Reagent grade potassium oxalate monohydrate ($K_2C_2O_4$•H_2O) (Fisher Scientific Inc., Fair Lawn, NJ) was used to prepare stock 1 molar (M) $K_2C_2O_4$ solution at 25°C. After equilibration, stock solutions were passed through a 0.22 μm filter (MAGNA, nylon, supported, plain, MSI, Westboro, MA). Reagent grade calcium chloride dihydrate ($CaCl_2$•$2H_2O$) (Fisher Scientific Inc., Fair Lawn, NJ) was used to prepare 0.01 M $CaCl_2$ solution at 25°C. The $CaCl_2$ solution was prepared the day of use to prevent $CaCO_3$ formation through reaction with CO_2 from the atmosphere. Diluted solutions of $K_2C_2O_4$ and $CaCl_2$ solutions were volumetrically prepared from the stock solutions.

A schematic representation of the processing steps for the preparation of COM crystals ("33" particles) without seeds is given in Figure 3.2. Precipitation studies were performed by mixing equal volumes (10 liter (ℓ)) of 10^{-3} M $CaCl_2$ and 10^{-3} M $K_2C_2O_4$ solutions at 25°C. Crystals of COM were aged for at least 24 hours without stirring. Solutions containing precipitated crystals were 0.22 μm filtered. The filtrate was washed with a solution saturated with COM to prevent dissolution of the precipitate during washing. After washing, the recovered powders were freeze dried (Freeze Drier 4.5, Labconco Corp., Kansas City, MO) and stored in a desiccator.

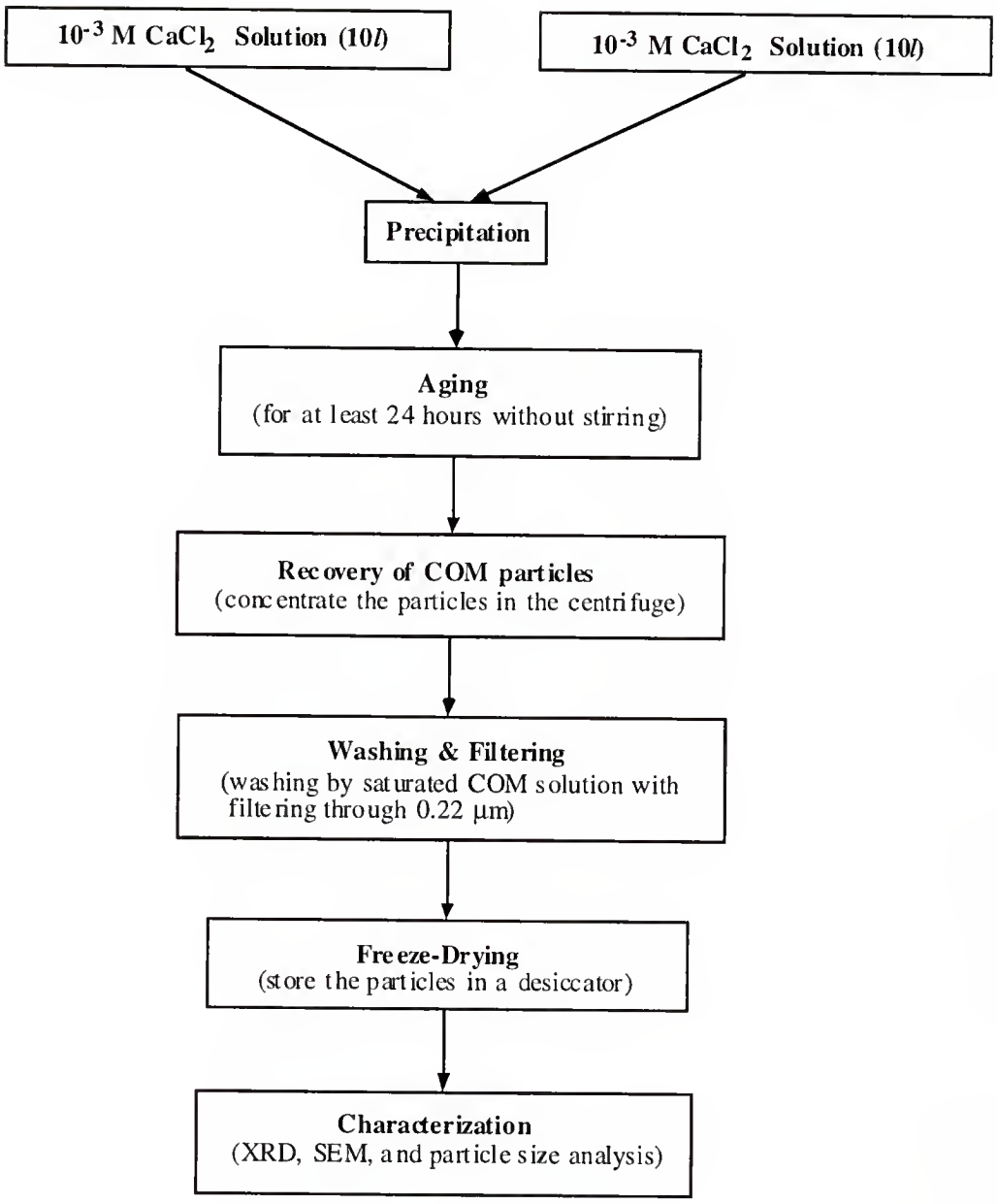
10^{-3} M $CaCl_2$ Solution (10*l*)
10^{-3} M $CaCl_2$ Solution (10*l*)
Precipitation
Aging
(for at least 24 hours without stirring)
Recovery of COM particles
(concentrate the particles in the centrifuge)
Washing & Filtering
(washing by saturated COM solution with filtering through 0.22 μm)
Freeze-Drying
(store the particles in a desiccator)
Characterization
(XRD, SEM, and particle size analysis)

Figure 3.2. Schematic representation of processing steps for the preparation of COM crystals ("33" particles) without seeds.

3.2.2 COM particles with seeds

Seed crystals ("00" particles) of COM were prepared by mixing equal volumes (50 ml) of 1 M $CaCl_2$ and 1 M $K_2C_2O_4$ solutions at 25°C. These seed crystals were aged for at least 24 hours without stirring. Crystals were concentrated by centrifugation and then washed with saturated COM solution. After washing, the recovered powders were freeze dried and stored in a desiccator. The seed suspension was prepared by dispersing 0.1 g of seed crystals in 5 ml isopropanol for a crystal growth experiment. The dispersion was treated by ultrasonication for 3 minutes to break up agglomerates.

A processing schematic for the preparation of COM crystals ("33" particles) with seeds is given in Figure 3.3. Precipitation studies were performed by mixing equal volumes (500 ml) of 10^{-3} M $CaCl_2$ and 10^{-3} M $K_2C_2O_4$ solutions at 25°C with various amounts of seed crystals. Crystals of COM were aged for at least 24 hours without stirring. Crystals were filtered 0.22 μm and then washed with a solution saturated with COM. The recovered powders were freeze dried and stored in a desiccator.

3.2.3 COM particles precipitated from homogeneous solution at 90°C

Gordon, Salutsky, and Willard have reported a recipe for the production of COM by the thermal decomposition of dimethyl oxalate [Gor59]. The goal of this section was to duplicate this procedure and analyze the nature of the particles. Ammonium acetate (CH_3COONH_4) (Fisher Scientific Inc., Fair Lawn, NJ) and acetic acid (CH_3COOH) (Fisher Scientific Inc., Fair Lawn, NJ) were used to prepare stock 2.5 M CH_3COONH_4 (aq) and 2.5 M CH_3COOH (aq) solution at 25°C. A buffer solution at pH 2.7 was prepared by mixing equal volumes (500 ml) of the 2.5 M CH_3COONH_4 (aq) and CH_3COOH (aq) stock solutions at 25°C. After equilibration, stock solutions were passed through a 0.22 μm filter.

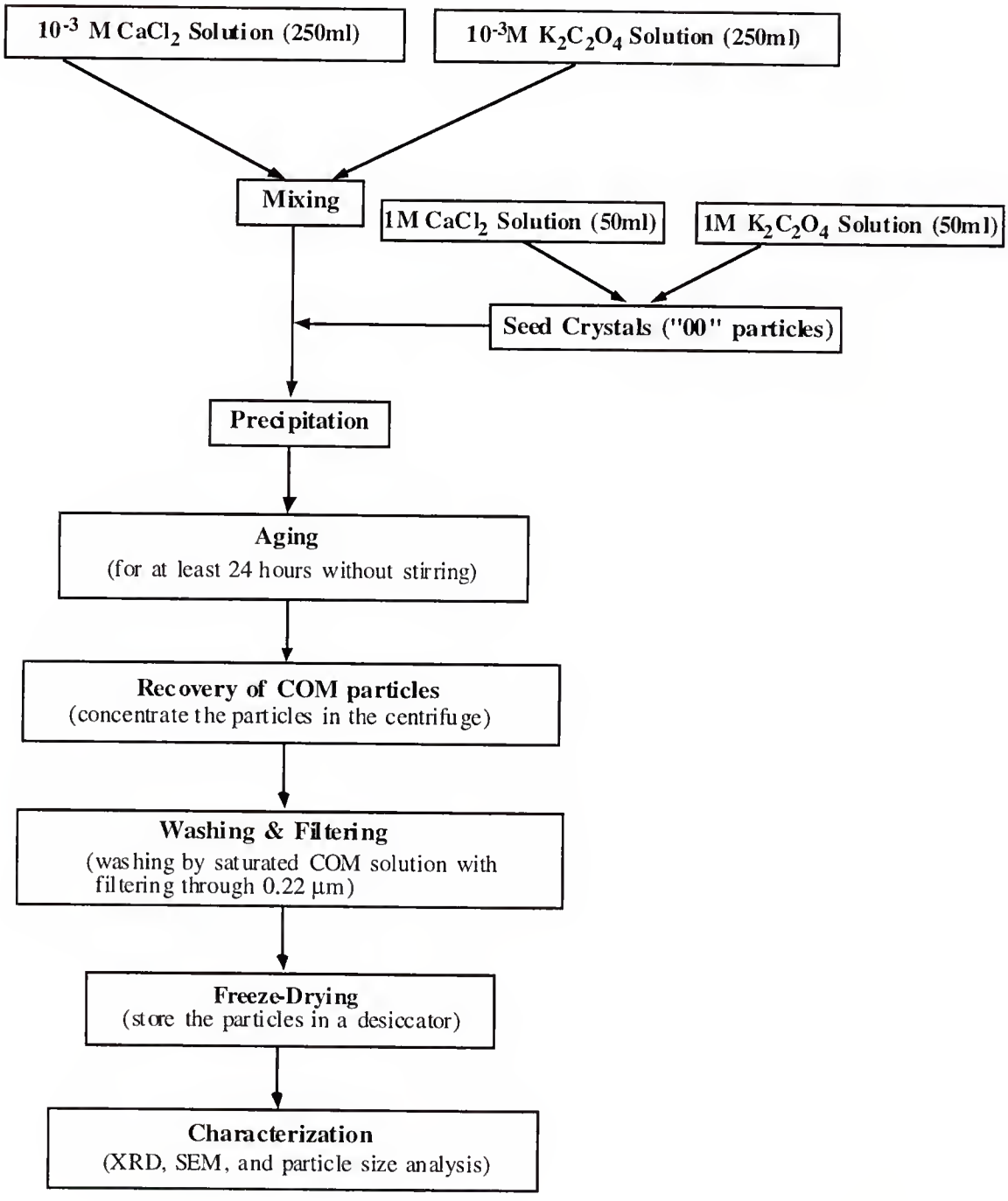
10^{-3} M $CaCl_2$ Solution (250ml)
10^{-3}M $K_2C_2O_4$ Solution (250ml)
Mixing
1M $CaCl_2$ Solution (50ml)
1M $K_2C_2O_4$ Solution (50ml)
Seed Crystals ("00" particles)
Precipitation
Aging
(for at least 24 hours without stirring)
Recovery of COM particles
(concentrate the particles in the centrifuge)
Washing & Filtering
(washing by saturated COM solution with filtering through 0.22 μm)
Freeze-Drying
(store the particles in a desiccator)
Characterization
(XRD, SEM, and particle size analysis)

Figure 3.3. Schematic representation of processing steps for the preparation of COM crystals ("33" particles) with seeds.

A schematic representation of processing steps for the preparation of COM crystals aged at 90°C is given in Figure 3.4. Reagent grade $CaCl_2 \cdot 2H_2O$ was used to prepare 0.01 M $CaCl_2$ solution at 25°C. The $CaCl_2$ solution was prepared the day of use to prevent $CaCO_3$ formation through CO_2 from the atmosphere. The dilute $CaCl_2$ solution were volumetrically prepared to obtain $2.5x10^{-3}$ M $CaCl_2$ solution. The pH of the dilute $CaCl_2$ solution was adjusted to 4.7 by adding 0.01 M HCl solution. After equilibration, the dilute $CaCl_2$ solution was filtered (0.22 μm). The $2.5x10^{-3}$ M $CaCl_2$ solution (150 ml) was rapidly mixed with buffer solution (100 ml) in a flask and 10 g of dimethyl oxalate ($CH_3OCOCOOCH_3$) (Fisher Scientific Inc., Fair Lawn, NJ) was added. The flask was tightly closed and heated at 90°C for 1 hour in an oven to equilibrate. The holding time at 90°C was 2.5 hours. After thermal treatment, the solution was rapidly cooled to room temperature in an ice bath. Crystals were collected via centrifugation followed by washing with saturated COM solution previously passed through a 0.22 μm filter. After washing, the recovered particles were freeze dried and stored in a desiccator.

3.2.4 Characterization

The dried, recovered powders were analyzed for phase composition using x-ray diffraction (XRD) (APD3720, CuKα, fine tube, 40kV-20mA, Philips Electronics, Mahwah, NJ) over a 2θ range from 10-70° at rate of 2.4°/min.

The morphology of the synthesized crystals were observed using scanning electron microscopy (SEM) (JSM 6400, JEOL, Boston, MA).

Particle size analysis of typical COM particles without seeds was performed using an electrical sensing zone technique (ELZONE 80XY, 95 μm aperture, Particle Data Incorporated, Elhurst, IL).

Zeta potential determination was performed using Rank Particle Microelectrophoresis (Apparatus Mark II, Rank Brothers, Cambridge, ENGLAND) as a

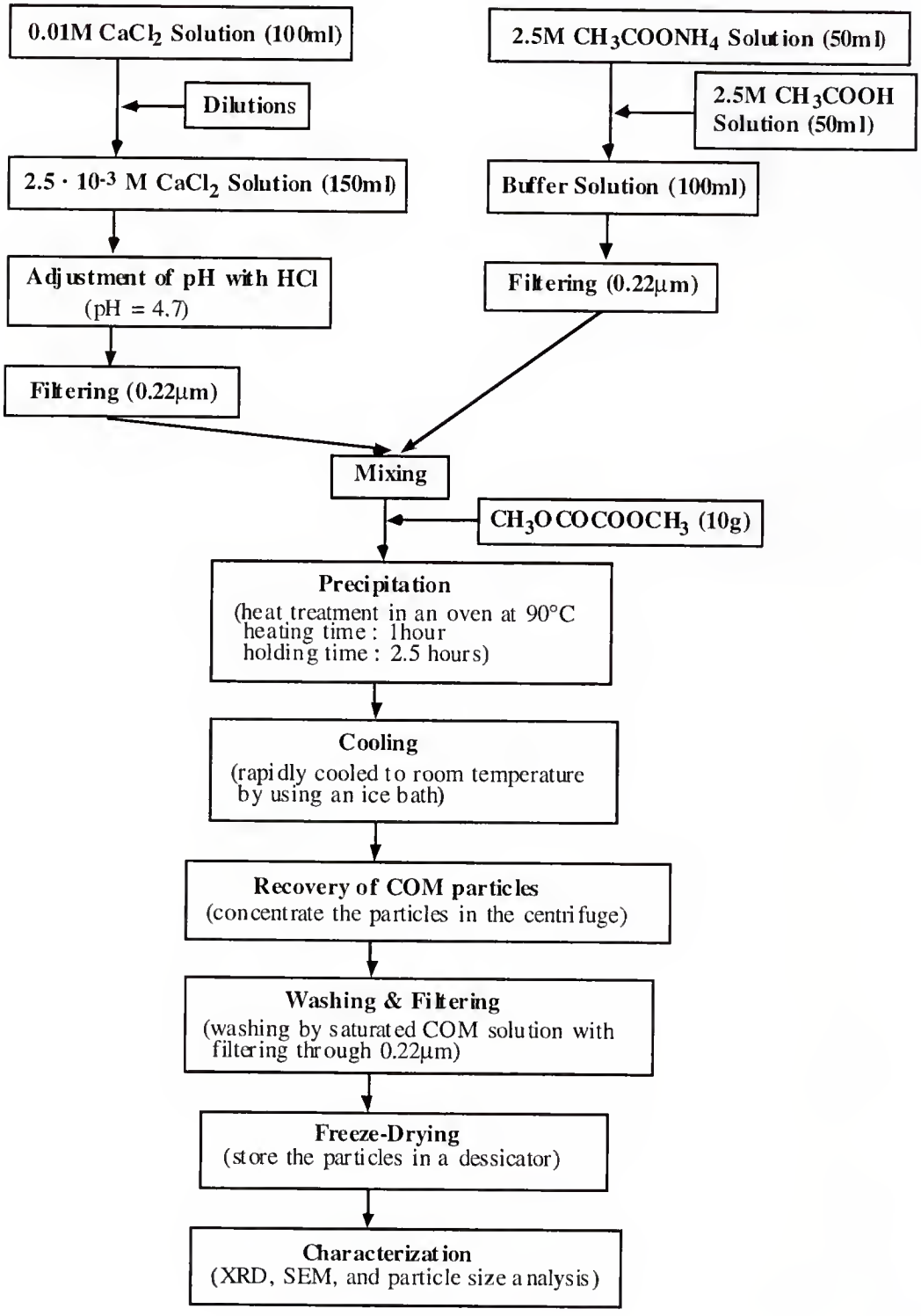

Figure 3.4. Schematic representation of processing steps for the preparation of COM crystals ("32" particles) with heat treatment at 90°C.

function of pH in COM saturated solution and in an artificial urine ion solution (AUIS) buffered to pH 6.0 at 37°C. The composition of the AUIS is given in Table 3.1.

Scanning probe microscopy (SPM) (MultiMode™, Digital Instruments, Santa Barbara, CA) was performed on the two major crystallographic surfaces of COM to determine surface roughness using a Nanoscope III controller. The J-type scanner was operated in contact mode using a Si_3N_4 cantilever having a spring constant of 0.12 N/m in saturated COM solution at 25°C.

3.2.5 Crystal and Atomic Structure Modeling Using the Computer Programs SHAPE© and ATOMS©

Based on crystallographic data including space groups and lattice parameters, the computer program SHAPE© (Macintosh version 4.0, SHAPE Software, Kingsport TN) was used to determine the face indices of the COM particles synthesized under various conditions and to generate the equilibrium shape of the crystals as a function of the central distance [Coc61]. The central distance is the perpendicular distance from the center of the crystal to the faces of the corresponding form. The greater the distance, the less prominent the form (the smaller the area of the faces of that form in the final shape). Form factors in the program are the least number of face indices needed to generate the desired equilibrium shape. Twins of COM particles were drawn using the "twin option" and "epitaxy option" in SHAPE©.

The theoretical atomic structure of COM was displayed using the computer program ATOMS© (Macintosh version 2.0, SHAPE Software, Kingsport TN). The slice option of the computer program ATOMS© was used in the process of analyzing and predicting surface structure as a function of habit plane. To draw an individual surface atomic structure using this option, it is necessary to enter the crystal class, the space group, the corresponding unit cell parameters, and the face indices and atomic coordinates. From the crystal class and space group, the program determines what symmetry

Table 3.1. Composition of artificial urine ion solution

Compound	Solution Concentration (M)
NaCl	0.10554
$NaHPO_4 \cdot 2H_2O$	0.03654
$Na_3C_6H_5O_7 \cdot 2H_2O$	0.00321
$MgSO_4$	0.0038476
Na_2SO_4	0.016952
KCl	0.06374
$CaCl_2 \cdot 2H_2O$	0.001
$Na_2C_2O_4$	0.00131
NH_4Cl	0.03632
NH_4OH	0.00062
NaOH	0.005

operators to use in the calculations. In addition to the indices of the face and input atoms, several other parameters were specified. The thickness of the slice is in fractions of the d-spacing. Thus, atoms present to a certain depth of unit cell were drawn with the "slice option" as a function of habit plane based on the atomic coordinates of the high and low temperature structures.

3.3 Results and Discussion

First, differing reports regarding lattice parameters for COM need to be reconciled. Table 3.2 summarizes crystallographic data proposed by various authors [Deg81a, Taz80, Coc61, Coc62, Deg80]. From Table 3.2, the unit cell parameters reported by Cocco [Coc61] and Tozzoli and Domeneghetti [Taz80] can be seen to have similar values in contrast to the unit cell parameters of the *a* and *c* axes reported by Deganello and Piro [Deg81a]. The equilibrium structures of COM were generated the crystallographic data proposed by Deganello and Piro [Deg81a] and Tozzoli and Domeneghetti [Taz80], as shown in Figure 3.5. Based on comparisons made between the theoretical equilibrium shape and the morphological form of the experimentally derived crystals, the equilibrium shape of COM crystals modeled using the lattice parameters of Deganello and Piro [Deg81a] can be more easily reconciled to the morphology of the experimentally synthesized COM crystals.

It is also necessary to mention conflicting papers regarding COM atomic coordinates. Table 3.3 shows atomic coordinates proposed by various authors [Deg81a, Taz80, Coc62]. From this table, the atomic coordinates reported by Cocco and Sabelli [Coc62] and Tozzoli and Domeneghetti [Taz80] have similar positions but only the *x* coordinates for carbon(1), carbon(2), oxygen(1), oxygen(3), and calcium(1) are different. The atomic coordinates reported by Deganello and Piro [Deg81a] are quite different from those of the previously mentioned authors. The equilibrium atomic structures of COM were generated using the three different atomic coordinates. Based on the comparison

Table 3.2. Values of the lattice parameters of calcium oxalate monohydrate

Authors	a (Å)	b (Å)	c (Å)	B (°)	Space Group
Cocco and Sabelli [Coc62]	6.24	14.58	9.89	107	$P2_1/c$
Tazzoli and Domeneghetti [Taz80]	6.290(1)	14.583(1)	10.116(1)	109.46(2)	$P2_1/c$
Deganello and Piro [Deg81a]	9.9763(3)	14.5884(4)	6.2913(3)	107.05(2)	$P2_1/n$

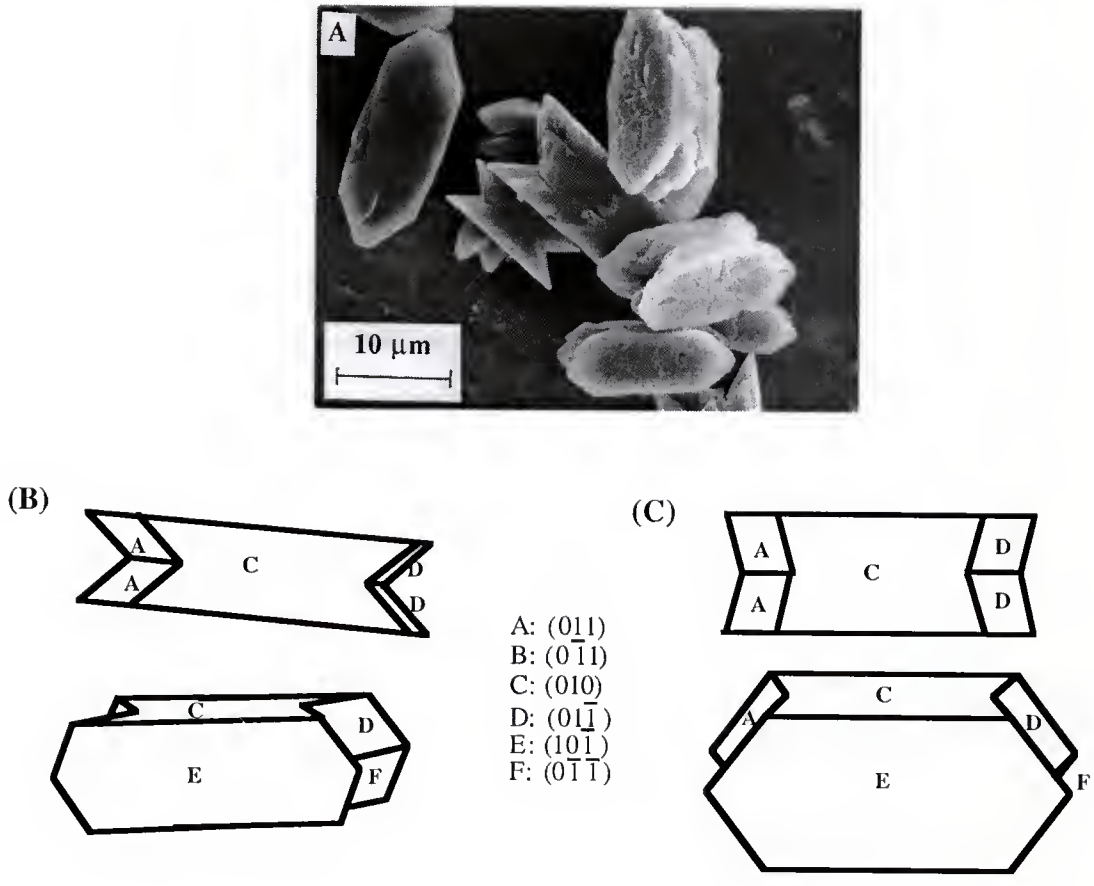

Figure 3.5. (A) SEM photomicrograph and (B) and (C) theoretical equilibrium shapes of the COM crystals precipitated without seeds. (B) The equilibrium shape of COM crystals based on the crystallographic data of Deganello and Piro [Deg81a] and (C) the equilibrium shape of COM crystals based on the crystallographic data of Tazzoli and Domeneghetti [Taz80].

Table 3.3. Atomic coordinates of Whewellite ($CaC_2O_4 \cdot H_2O$)

Atom	Cocco and Sabelli [Coc62]			Tazzoli and Domeneghetti [Taz80]			Deganello and Piro [Deg81a]		
	x	y	z	x	y	z	x	y	z
C(1)	0.0079	0.3220	0.2513	0.9832	0.3201	0.2452	-0.2452	0.3201	-0.2620
C(2)	0.0012	0.4296	0.2540	1.0009	0.4270	0.2492	-0.2493	0.4270	-0.2481
C(3)	0.5421	0.1103	0.1852	0.5189	0.1266	0.1812	-0.1812	-0.1264	0.3377
C(4)	0.4822	0.1279	0.3200	0.4505	0.1173	0.3131	-0.3130	-0.1175	0.1375
O(1)	0.0279	0.2811	0.1486	0.9756	0.2826	0.1322	-0.1322	-0.2826	-0.1566
O(2)	0.9981	0.4671	0.1389	1.0066	0.4659	0.1395	0.1359	0.4660	0.1329
O(3)	0.0301	0.2844	0.3727	0.9799	0.2819	0.3550	0.3555	0.2819	0.3751
O(4)	0.9911	0.4669	0.3605	1.0073	0.4658	0.3614	-0.3614	-0.4658	-0.3541
O(5)	0.3827	0.1212	0.0727	0.3614	0.1418	0.0690	0.0690	0.1418	0.2924
O(6)	0.7546	0.1261	0.1995	0.7245	0.1227	0.1974	-0.1975	-0.1226	0.5271
O(7)	0.2690	0.1275	0.3017	0.2438	0.1229	0.2957	-0.2958	-0.1229	-0.0519
O(8)	0.6398	0.1170	0.4376	0.6073	0.1068	0.4264	-0.4263	-0.1066	0.1809
Ca(1)	0.0049	0.1227	0.0639	0.9676	0.1243	0.0546	-0.0546	-0.1243	-0.0870
Ca(2)	0.0305	0.1263	0.4438	0.9968	0.1236	0.4357	-0.4357	-0.1236	-0.4389
W(1)	0.4032	0.4013	0.1059	0.3932	0.3459	0.1022	-0.6023	-0.1542	-0.2090
W(2)	0.6084	0.3461	0.3977	0.5913	0.3829	0.3908	0.1093	-0.1172	-0.2940
H(1)				0.487	0.372	0.051			
H(2)				0.510	0.364	0.426			
H(3)				0.530	0.367	0.320			

between the theoretical atomic structures generated using ATOMS© and the atomic structures from the papers by Deganello and Piro [Deg81a] and Tazzoli and Domeneghetti [Taz80], the (010) and (100) planes generated with the atomic coordinates published by Cocco and Sabelli [Coc62] are exactly reconciled to the layering sequence reported by Deganello and Piro [Deg81a] and Tozzoli and Domeneghetti [Taz80] as shown in Figure 3.6(A) and (B). However, the (010) and (100) planes generated with the atomic coordinates by Tozzoli and Domeneghetti [Taz80] are not reconciled to the layering sequence reported by Deganello and Piro [Deg81a] and Tozzoli and Domeneghetti [Taz80]. The atomic structures of some oxalate ions are incomplete as shown in Figure 3.6(C) and (D). Furthermore, the (010) and (100) planes generated with the atomic coordinates of Deganello and Piro [Deg81a] are completely different from the layering sequence reported by Deganello and Piro [Deg81a] and Tozzoli and Domeneghetti [Taz80] as shown in Figure 3.6(E) and (F). Thus, the atomic coordinates of Cocco and Sabelli [Coc62] were used in computer simulations of atomic structure as a function of habit plane.

3.3.1 COM particles ("33" particles) without seeds

The COM crystals grown in distilled water without seeds are shown in 3. 5(A). The interpenetrating crystals have sharply-angled tips and a distinctive shape. Figure 3.5(B) shows the equilibrium shapes of these interpenetrating twins with labeled face indices. For the twin operation, the individual crystal is reproduced according to the reflection on $(\bar{1}01)$. The crystallographic form factors and central distances for the interpenetrating twins used in SHAPE© calculations are listed in Table 3.4. Determinations made from observations of the computer calculation and the morphological form of the experimentally derived particles, the {010} and $\{10\bar{1}\}$ faces appear to be dominant.

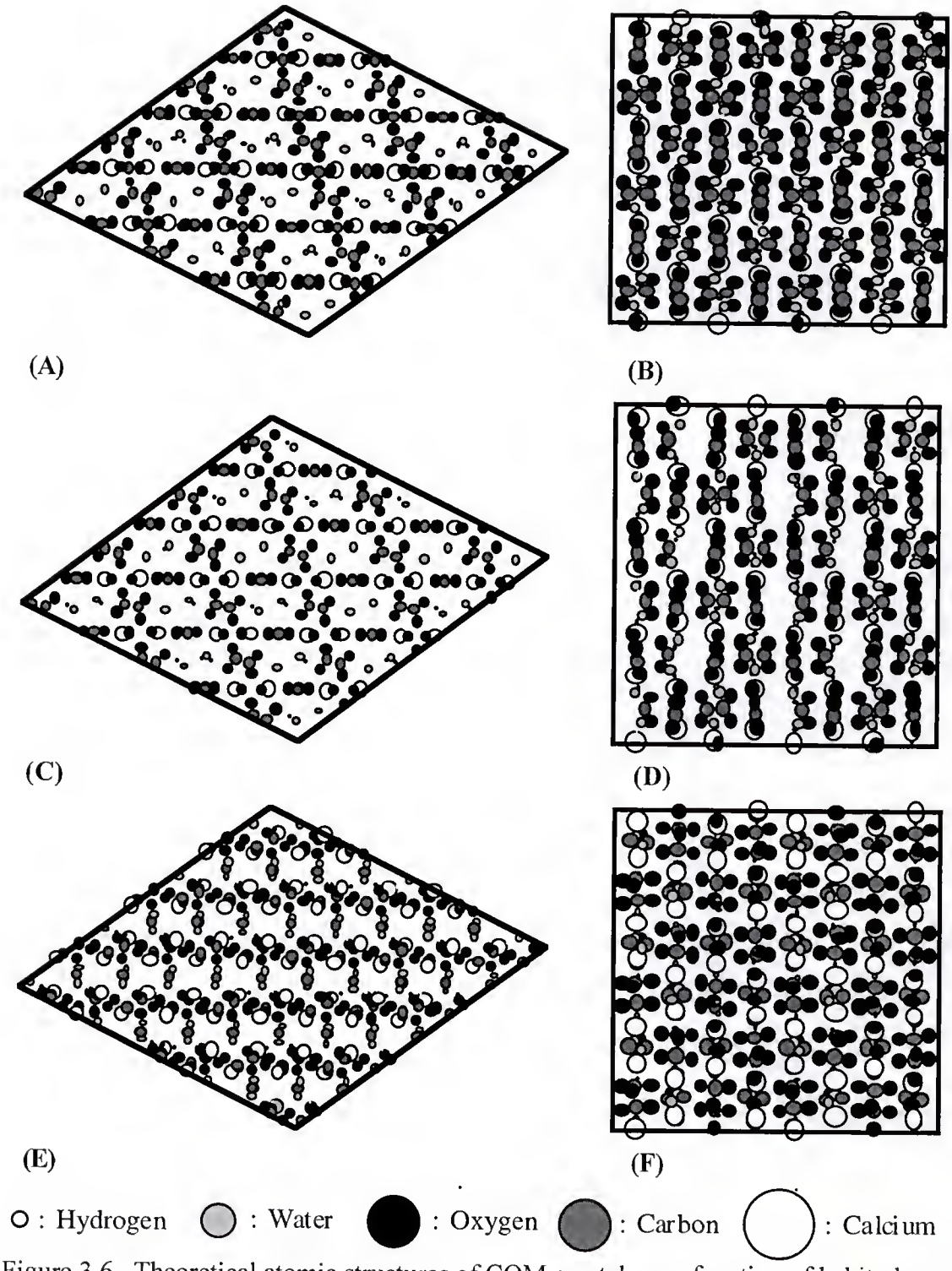

Figure 3.6. Theoretical atomic structures of COM crystals as a function of habit plane: (A) and (B) are the (010) and (100) planes, respectively, drawn using Cocco and Sabelli [Coc62] atomic coordinates; (C) and (D) are the (010) and (100) planes, respectively, drawn using Tazzoli and Domeneghetti [Taz80] atomic coordinates; (E) and (F) are the (010) and (100) planes, respectively, drawn using Deganello and Piro [Deg81a] atomic coordinates.

Table 3.4. Crystal forms and corresponding central distance values used to generate the theoretical shape of COM crystals

	Forms	Face Indices	Central Distance (shape with (010) plane)	Central Distance (shape with (001) plane)
33 COM Crystals*	1	010	4.0	
	2	011	6.0	
	3	$10\bar{1}$	3.0	
00 COM Seed Crystals	1	010/001	4.0	2.0
	2	011	2.0	2.0
	3	$10\bar{1}$	0.5	0.5
32 COM Crystals† (Aged at 90°C)	1	010/001	2.0	2.0
	2	011	4.0	4.0
	3	$10\bar{1}$	1.0	1.0

The equilibrium shape of the interpenetrating twin is generated according to the reflection on the $(10\bar{1})$.
The equilibrium shape of the contact twin is generated according to the epitaxial operation. The host crystal is specified by the face (001) and the vector [010]and the guest crystal is specified by the face $(00\bar{1})$ and the vector $[0\bar{1}0]$. The central distance for the epitactic face (001) is 2.0.

3.3.2 COM particles ("33" particles) with seeds

The seed crystals ("00" particles) precipitated by mixing equal volumes (50 ml) of 1 M $CaCl_2$ and 1 M $K_2C_2O_4$ solutions are shown in Figure 3.7(A). The particle size varies between 100-500 nm. Although the shape and size are not uniform, the crystals are composed of submicron size particles suitable for seed materials. Figure 3.7(B) shows the equilibrium shapes of the seed crystals with face indices as calculated by SHAPE© with the crystallographic form factors and central distances for COM seed crystals listed in Table 3.4. The $\{10\bar{1}\}$ faces appear to be dominant based on the computer calculation and the morphological form of the experimentally derived particles. Also, only the equilibrium shape generated with the (001) face was reconciled with the morphology of experimentally prepared seed crystals as shown in Figure 3.7(B).

Figure 3.7(C) shows that the influence of seed particles on the size of COM crystals grown in distilled water. These interpenetrating crystals produced with 0.1 ml of seeding suspension have similar shape to the COM crystals grown without seeds, but are smaller in size. The maximum size of the particles is about 1 μm. Thus, it is demonstrated that the presence of seed particles may provide a low energy epitaxial surface in solution to lower the overall surface energy contribution to the nucleation barrier, increasing nucleation frequency, and reducing the particle size of COM crystals without changing the particle morphology. Also, the seeding studies suggest the possibility of controlling the size of the COM crystals ("33" particles) by controlling the amount of seed materials. From the morphological difference between seed crystals and COM crystals synthesized with seeds, the effect of seed crystals can be gauged from two aspects: (1) the presence of seed crystals in the solution system probably lowers the surface energy barrier of the system to the nucleation and growth of particles, and (2) the transformation in this case is not only influenced by the number of added seed crystals,

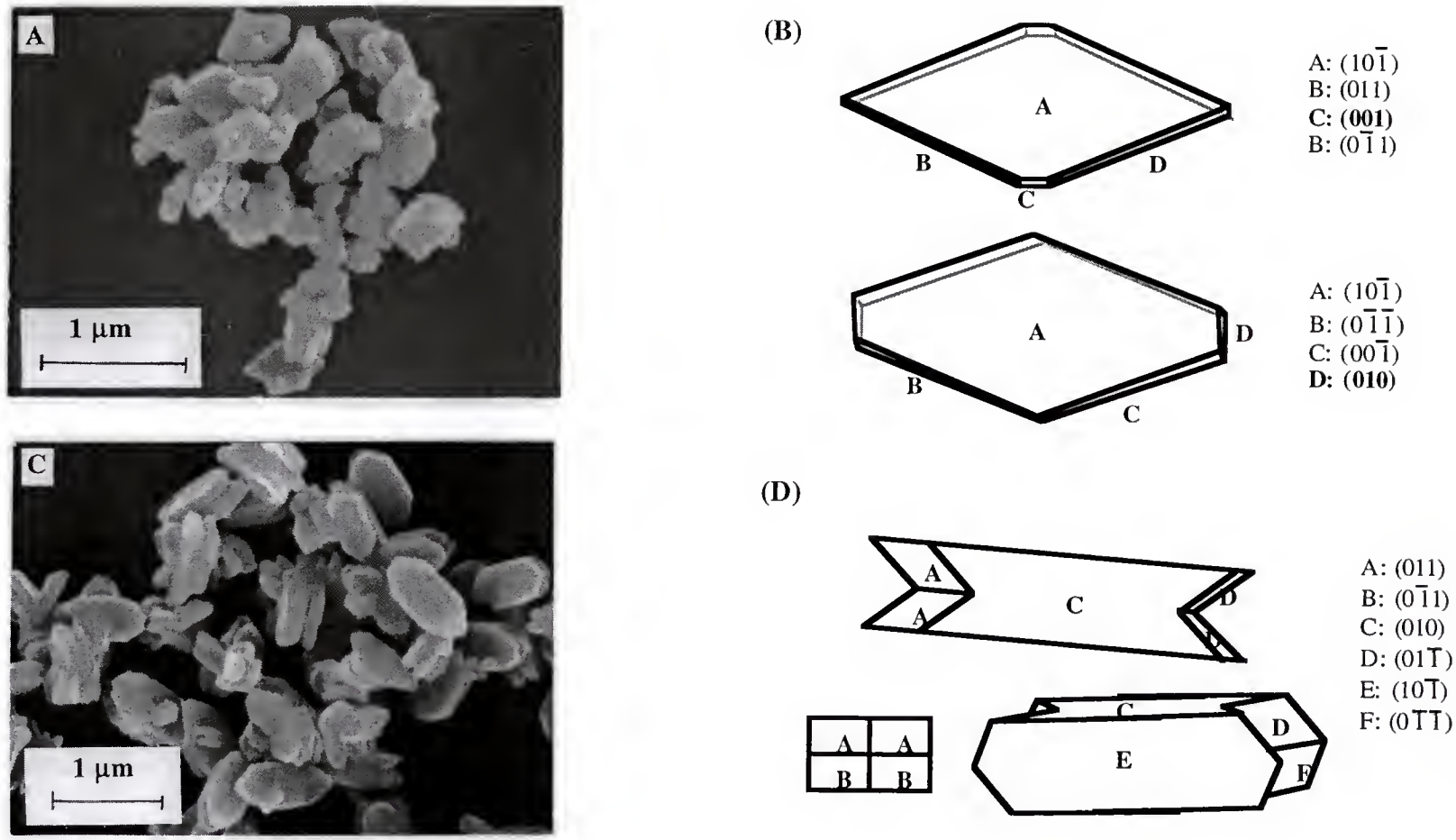

Figure 3.7. SEM photomicrographs and theoretical equilibrium shapes of seed crystals and the COM crystals precipitated using seeds: (A) seed crystals, (B) equilibrium shapes of seed crystals generated with the (001) and (010) faces, respectively, (C) COM crystals grown using seeds, and (D) equilibrium shape of COM crystals.

but also by forming larger numbers of nuclei due to the seeds and possibly secondary nucleation [Nyv85, Ran88].

3.3.3 COM particles precipitated from homogeneous solution at 90°C

Habit modification of COM crystals grown with structurally specific additives gives further demonstration of specific preferential binding. The COM crystals which were made using dimethyl oxalate decomposition from 2.5×10^{-3} M $CaCl_2$ solution at 90°C are shown in Figure 3.8(A). Habit modification is obvious for the COM crystals grown by dimethyl oxalate decomposition.

Figure 3.8(B) shows the equilibrium shapes of an individual COM crystal and contact twin with face indices. The crystallographic form factors and central distances for COM crystals are listed in Table 3.4. For the contact twins, the individual crystal is reproduced according to the epitaxial operation in SHAPE©. The host crystal is specified by the (001) face and the [010] vector and the guest crystal is specified by the $(00\bar{1})$ face and the $[0\bar{1}0]$ vector. The central distance for the epitactic face (001) is 2.0. The $\{10\bar{1}\}$ faces appear to be dominant when comparing the computer calculation to the morphological form of the experimentally derived particles. Also, the equilibrium shape generated with the (001) face more closely resembles the experimentally prepared COM crystals in contrast to the equilibrium shape generated with the (010) face, as shown in Figure 3.8(B) and (C).

3.3.4 Atomic structures of COM particles as a function of habit plane for the high temperature form

Equilibrium atomic structures of COM particles were generated as a function of habit plane to predict the atomic structures of specific surfaces. In whewellite, there exist two different crystal structures: a high temperature structure (stability range 318-415 K) and a low temperature structure (stability range 293-318 K) [Deg81b, Deg80]. Table 3.5 and

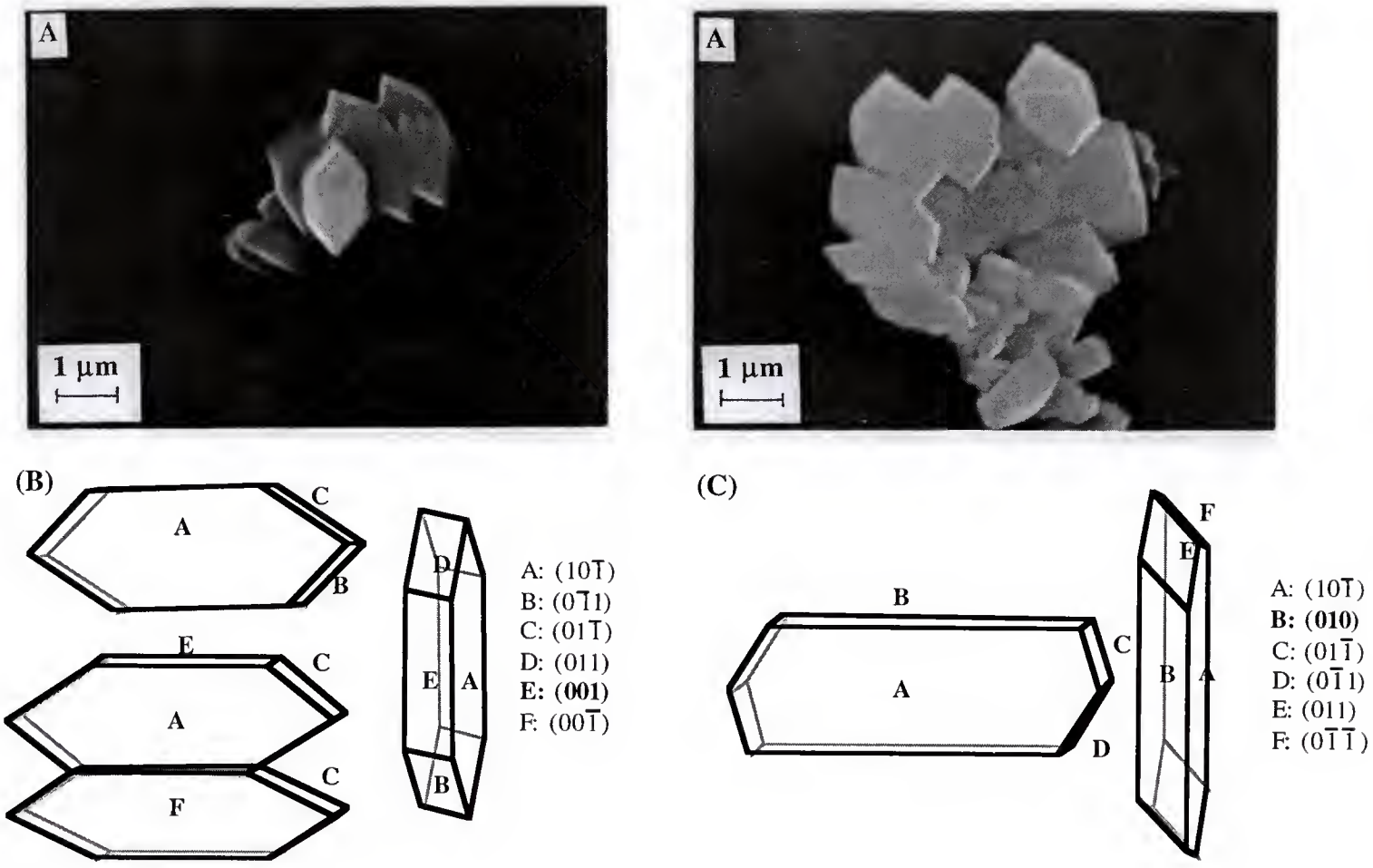

Figure 3.8. SEM photomicrograph and theoretical equilibrium shapes of the COM crystals precipitated from homogeneous solution at 90°C: (A) COM crystals, (B) equilibrium shapes of an individual COM crystal and a crystal with a twin generated on the (001) face, and (C) equilibrium shapes of COM crystals generated using the (010) face as the dominant face.

Table 3.5. Values of the crystallographic data for the high temperature form [Deg81b, Deg80] of Whewellite ($CaC_2O_4 \cdot H_2O$)

	High Temperature Form
a (Å)	9.978(1)
b (Å)	7.295(1)
c (Å)	6.292(1)
Space Group	I2/m
Stability Range (K)	318-425
Ca/Ox Ratio	
(010)	0.958
$(10\bar{1})$	1.658

Table 3.6 summarize the crystallographic data and atomic coordinates of the high temperature form. Based on the crystallographic data and atomic coordinates, Figure 3.9 shows the equilibrium atomic structures of specific habit planes for the high temperature form. Habeger et al. [Hab97] has shown that the ratio of calcium atoms to oxalate molecules may have an important implication in the adhesion properties of the different crystal faces in a model environment. The ratio of calcium ions to oxalate ions is 0.958 in the (010) plane whereas the ratio of calcium ions to oxalate ions is 1.658 in the $(10\bar{1})$ plane for the high temperature form. Although the temperature in the human body cannot produce the high temperature phase of COM, the adsorbtion of ions or molecules may stabilize the high temperature structure at lower temperatures. The stabilization of the high temperature structure of COM in the urinary system may have a large implication in that the $(10\bar{1})$ has a $Ca^{+2}/C_2O_4^{-2}>1$, making the crystal face positively charged and able to electrostatically interact with predominately negatively charged biosurfaces found in the human body.

3.3.5 Characterization of COM crystals

The morphologies reported herein were determined to be phase pure COM by XRD. A typical XRD pattern is shown in Figure 3.10.

As shown by SEM of the various COM morphologies, the "33" particle synthesizes without seeds were the most consistent morphology produced. Visually, they had very few differently shaped particles and a relatively narrow size distribution relative to the other particle morphologies synthesized. Therefore further characterization will only involve the "33" COM particles synthesized without seeds and further mention of COM particles refers only to this particular morphology.

Peakfit software was used to fit a log normal curve to the experimentally produced particle size distribution. The particle size distribution was determined using an electrical zone sensing technique which results in an equivalent spherical diameter vs. frequency

Table 3.6. Atomic coordinates for high temperature form [Deg81b] of Whewellite ($CaC_2O_4 \cdot H_2O$)

	High Temperature Form		
Atom	x	y	z
C(1)	-0.0652	0.0	0.3984
C(2)	0.0	0.3937	0.0
O(1)	0.1105	-0.3157	0.1096
O(2)	-0.0493	0.0	0.2119
O(3)	-0.1783	0.0	0.4454
Ca(1)	0.1903	0.0	0.1751
Ca(2)			
W(1)	-0.3552	0.0	0.0438
H(1)	0.45	0.0	0.04
H(2)	-0.33	0.05	0.2

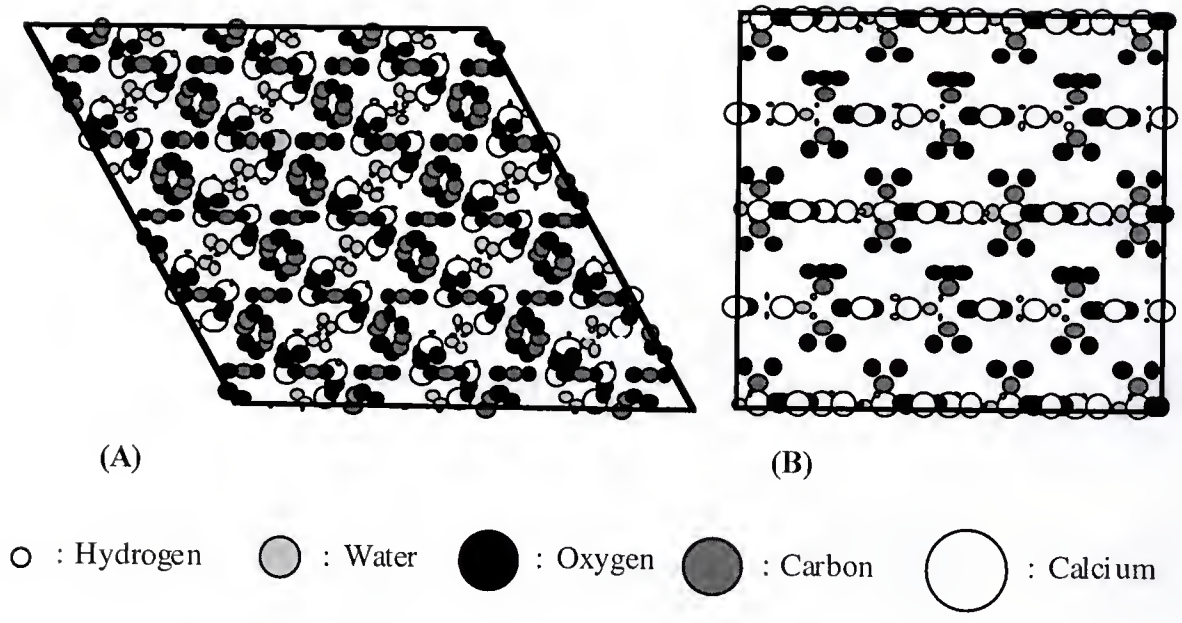

Figure 3.9. Theoretical atomic high temperature structure [Deg81b] (stability range: 318-415 K) of COM crystals as a function of habit plane, (A) (010) plane and (B) $(10\bar{1})$.

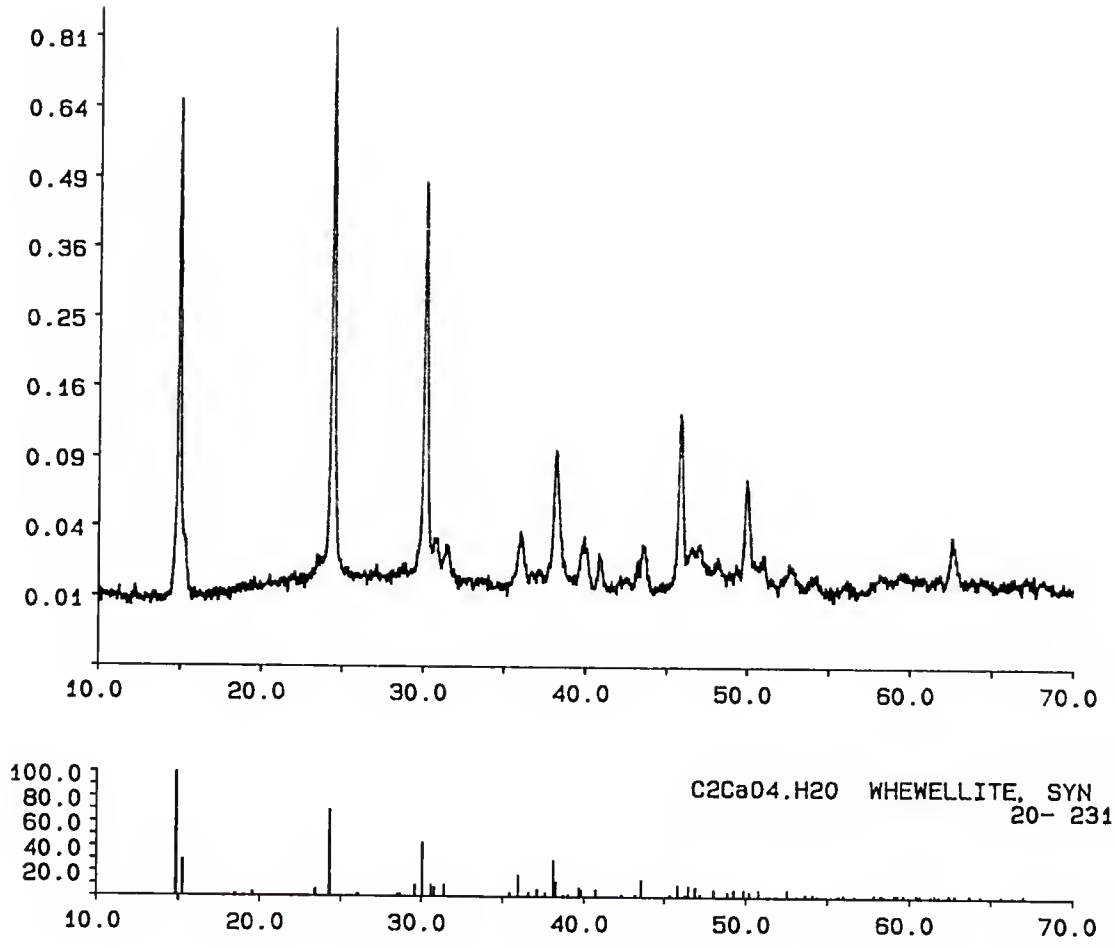

Figure 3.10 A (top) typical experimental COM x-ray diffraction pattern and (bottom) the JCPDS file for the mineral whewellite, $CaC_2O_4 \cdot 2H_2O$.

distribution as shown in Figure 3.11. The mean and standard deviation in particle size is 13.04 μm and 1.27 μm, respectively. The least square regression coefficient of the curve fit is 0.98.

For purposes of calculation, the relative dimensions of the COM particles were measured by analyzing multiple particles from SEM photomicrographs. The relative sizes illustrated in Figure 3.12 were used calculating surface areas of the two major crystallographic faces given the equivalent spherical diameter, refer to Appendix A.

Zeta potential of the COM crystals was determined as a function of pH in saturated COM solution as shown in Figure 3.13. Also on Figure 3.13, one data point representing the zeta potential of COM crystals in 10% AUIS at the buffered pH of 6.0.

The zeta potential values for COM in saturated COM solution and in 10% AUIS at pH 6 are -32 mV and -21 mV, respectively. As can be seen from Figure 3.13, the lower ionic strength, $5x10^{-6}$ M, COM saturated solution has a higher zeta potential than the higher ionic strength, $3.71x10^{-2}$ M, 10% artificial urine at pH 6. This effect is expected and is due to compression of the electrical double layer.

As the ionic strength of the electrolyte the COM crystals are suspended in increases (i.e., 10% AUIS to 50% AUIS to 100% AUIS), the value of zeta potential will decrease. When the ionic strength becomes high, the measurement of zeta potential using Rank Particle Microelectrophoresis becomes impossible. Compression of the electrical double layer is extreme and the potential distribution near the particle surface drops rapidly as a function of distance into the solvent, Figure 2.5. Therefore the particles do not move under the applied electric field and measurements of electrophoretic mobility cannot be made.

Contact mode scanning probe microscopy (SPM) was performed on both the (010) and $(10\bar{1})$ crystallographic faces of a COM particle in saturated COM solution at 25°C to determine the surface roughness. The r_a values or the mean roughness values for

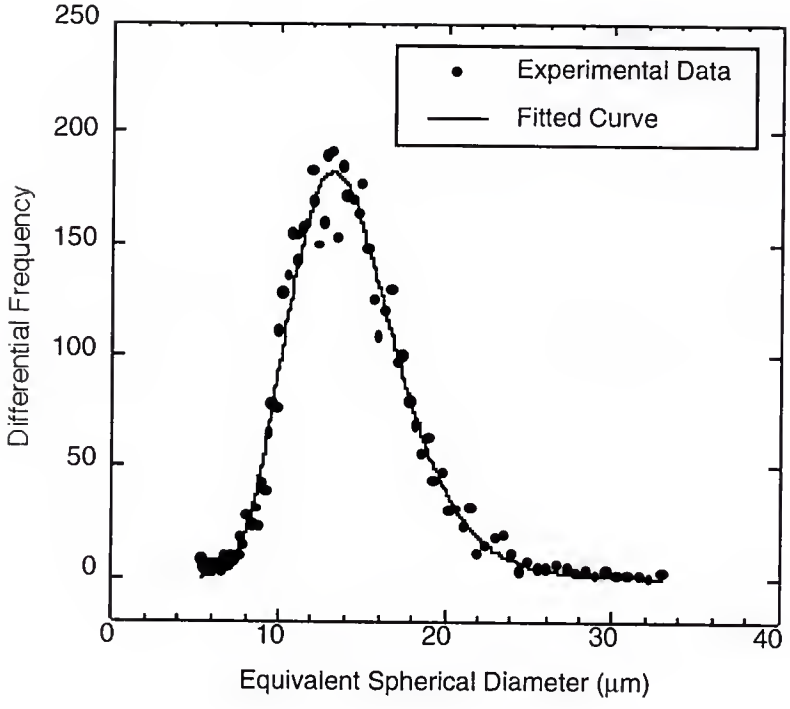

Figure 3.11. The differential frequency vs. equivalent spherical diameter particle size distribution of the experimentally produced COM crystals grown without seeds fit to a log-normal probability distribution.

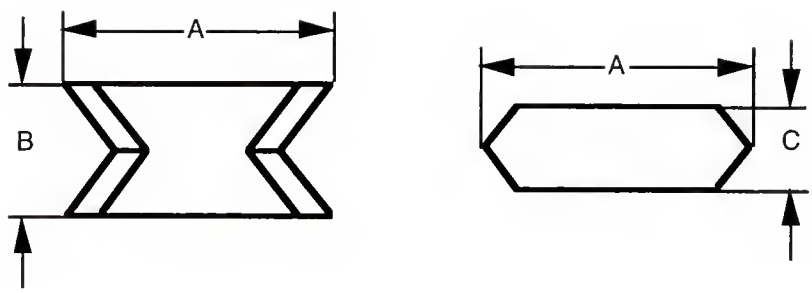

Figure 3.12. The relative linear dimensions of experimentally produced COM crystals.

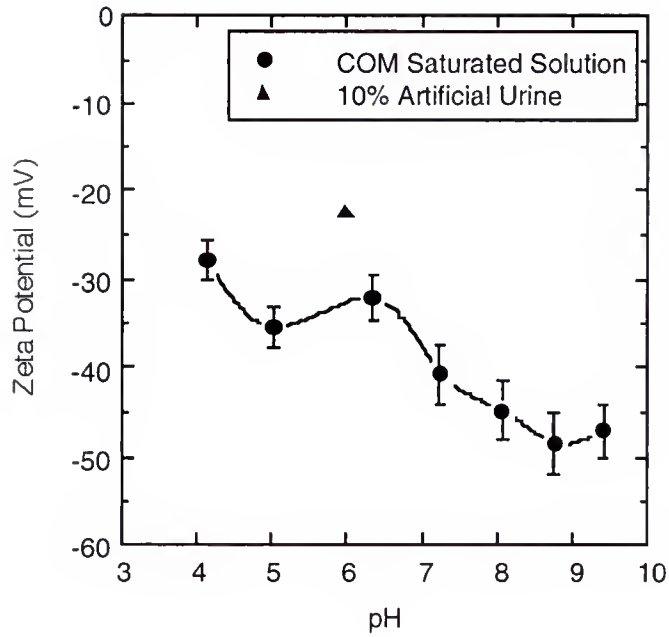

Figure 3.13 Zeta potential as a function of pH for COM in saturated COM solution and zeta potential at pH 6 for COM in 10% AUIS.

the COM (010), Figure 3.14, and ($10\bar{1}$), Figure 3.15, are 91nm and 81 nm, respectively, over a scan area of 5 μm by 5 μm. The high surface roughness of the COM crystal may be due to the growth mechanism of the twinned COM crystal. The crystals have a growth ledge at the twin boundary where the crystal may grow more rapidly on one half of the twin boundary but not on the other causing the roughness to be large across this boundary.

3.4 Conclusions

The equilibrium shapes with face indices of calcium oxalate monohydrate (COM) particles synthesized in different conditions have been successfully generated using the computer program SHAPE©. Computer calculations of theoretical crystallographic shapes have been reconciled to the observed shapes of experimentally synthesized COM particles under various conditions. Also, the seeding studies suggest that it is possible to control the size of COM crystals ("33" particles) by controlling the amount of seed materials. The computer program SHAPE© was demonstrated to be a useful tool to determine the face indices of COM crystals. The equilibrium shape of COM crystals based on the lattice parameters of Deganello and Piro [Deg81a] is reconciled to the morphology of the experimentally synthesized COM crystals from the comparison between the calculated shape and the morphological form of the experimentally derived particles.

Based on the face indices of the equilibrium shapes and atomic coordinates, the atomic structures of COM particles as a function of habit plane have also been generated by using the computer program ATOMS©. From the comparison between the theoretical atomic structures generated by ATOMS©, the (010) and (100) planes generated with the atomic coordinates published by Cocco and Sabelli [Coc62] are reconciled to the layering sequence reported by Deganello and Piro [Deg81a] and Tozzoli and Domeneghetti [Taz80].

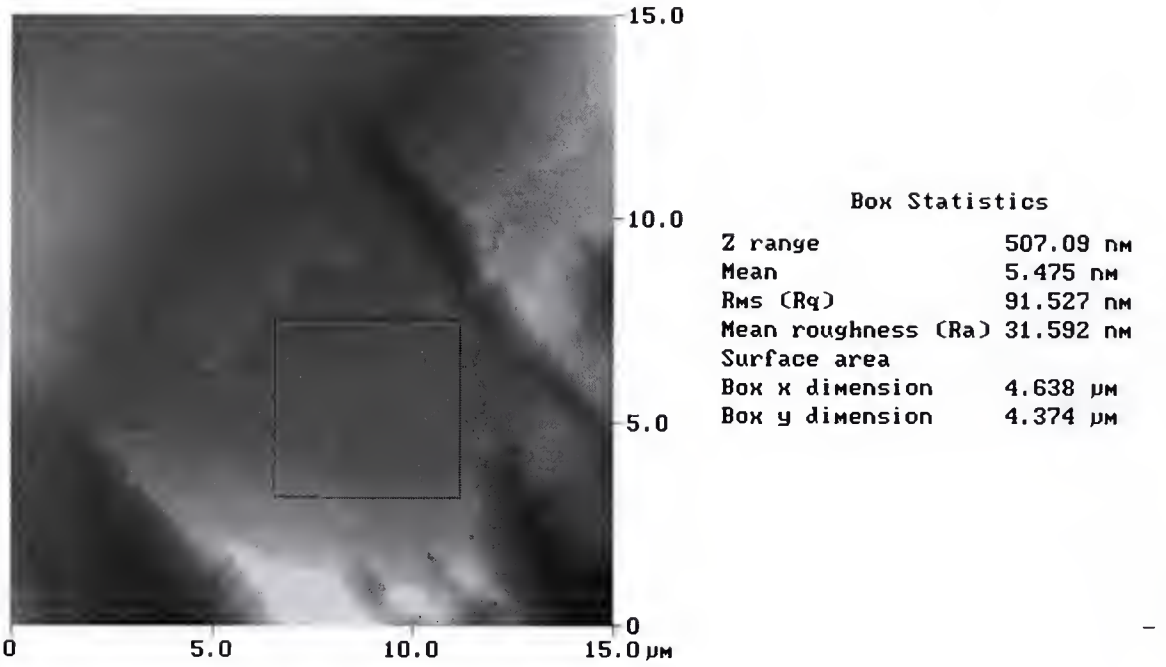

Figure 3.14 Contact mode SPM scan of the COM (010) crystallographic face showing the surface roughness.

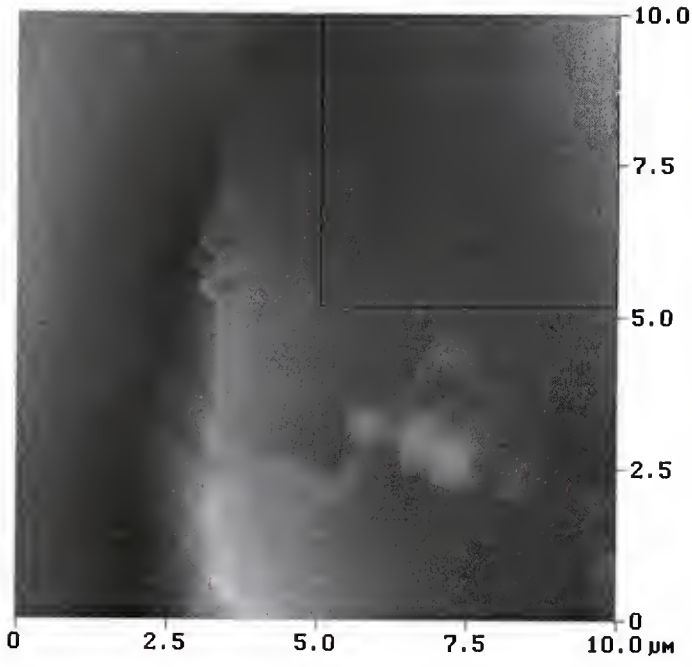

Box Statistics

Z range	1.025 µm
Mean	-6.614 nm
Rms (Rq)	175.45 nm
Mean roughness (Ra)	81.202 nm
Surface area	
Box x dimension	4.951 µm
Box y dimension	4.834 µm

Figure 3.15 Contact mode SPM scan of the COM ($10\bar{1}$) crystallographic face showing the surface roughness.

CHAPTER 4
EVALUATION OF THE CALCIUM OXALATE MOMOHYDRATE HAMAKER CONSTANT BASED ON STATIC DIELECTRIC CONSTANT DETERMINATION AND ELECTRONIC POLARIZATION

4.1 Introduction

The ability to predict calcium oxalate monohydrate (COM) stability with respect to aggregation and adhesion for patients suffering from a kidney stone is of great importance. Since COM crystals are a major component of many types of urinary stones, the accurate predictions for COM aggregation in the urinary environment can aid in the treatment of such stone occurrences. Many of the interactions that take place in the prediction and urinary environment are dominated by van der Waals forces due to the relatively high ionic strength in the urinary environment, which tends to collapse the electrical double layer and hence diminishes electrostatic effects. In fact, Boeve et al. [Boe94] have measured the zeta potential for COM in an artificial urinary ion environment (ionic strength 0.33 M) to be <5 mV.

Both aggregation of like particles and adhesion of particles to unlike surfaces can potentially lead to the production of a kidney stone [Fin84]. Therefore an accurate value of the Hamaker constant for the material COM is important in predicting the van der Waals interactions with like and unlike materials. COM crystals have been shown previously to adhere to unlike materials such as fused quartz [Chapter 5] and various protein substrates [Chapter 6]. The adhesion of COM crystals to the fused quartz and protein substrates occurred in a relatively low ionic strength (~$2x10^{-4}$ M) environment, in spite of an electrostatic repulsive interaction between the two materials. This

demonstrates the importance of understanding the nature of van der Waals interactions and of knowing the value of the Hamaker constant. Other aspects of particle dispersion, such as those arising from surface energy, which may contribute to the total interaction energy are beyond the scope of this study and will not be considered herein.

The origin of the van der Waals attractive forces and the calculation of the Hamaker constant have been discussed in several reviews and, therefore, will only be briefly summarized [Hou80, Isr92]. The attractive van der Waals forces are composed of multiple intermolecular interactions between the ions, molecules, and electrons that make up the particles interacting across a dielectric medium such as water. The mutual attraction between interacting particles arise from harmonic oscillations at the molecular, atomic, or subatomic level. There are three primary sources of such intermolecular interactions depending upon the nature of the interacting species. Some of the more important specific interactions are known as the Keesom, Debye, and London interactions. The Keesom interactions are due to molecular dipoles in the particles. Debye interactions occur when molecular dipoles in one particle induce electronic polarization in the other interacting particle. As such, Keesom and Debye interactions only take place if a material has one or more dipoles present within its structure. In contrast, London interactions are more ubiquitous because London interactions are due to mutual electronic polarization with all atoms, of course, composed of electrons. Lifshitz and co-workers demonstrated that an understanding of the dielectric constant over as broad a frequency range as possible is required to reconcile all of the various possible intermolecular interactions between particles in order to calculate the most accurate Hamaker constant [Hou80, Isr92].

The objective of the present work is to evaluate and increase the accuracy of the value of the Hamaker constant of COM previously calculated by Adair et al. [Ada91] taking into account only electronic polarization. The re-evaluation will use the Tabor-Winterton relationship, incorporating new dielectric data for COM [Hou80, Isr92]. The

Tabor-Winterton relationship for dissimilar materials interacting across a medium is [Hou80, Isr92],

$$A_{132} \approx \frac{3}{4}kT\left(\frac{\kappa_1-\kappa_3}{\kappa_1+\kappa_3}\right)\left(\frac{\kappa_2-\kappa_3}{\kappa_2+\kappa_3}\right) + \frac{3h\nu_e}{8\sqrt{2}}\left[\frac{\left(n_1^2-n_3^2\right)\left(n_2^2-n_3^2\right)}{\left(n_1^2+n_3^2\right)^{1/2}\left(n_1^2+n_3^2\right)^{1/2}\left[\left(n_1^2+n_3^2\right)^{1/2}+\left(n_2^2-n_3^2\right)^{1/2}\right]}\right] \tag{4.1}$$

where κ and n refer to the static dielectric constant and the index of refraction at the characteristic frequency, ν_e, for electronic polarization., respectively. The subscripts 1 and 2 represent the interacting materials, and the subscript 3 represents the medium. The Tabor-Winterton relationship is based on Lifshitz theory and assumes that the electronic relaxation frequency, ν_e, is the same for all materials. This assumption will not generally lead to too large an error since the value of ν_e for many materials is ~$3x10^{15}$ Hz.

A simplified version of the Tabor-Winterton relationship [Tab69] is shown in equation (4.2). This equation may be used to calculate the Hamaker constant for the interaction of identical materials across a medium such as for the COM-water-COM system [Hou80, Isr92],

$$A_{131} = \frac{3}{4}kT\left(\frac{\kappa_1-\kappa_3}{\kappa_1+\kappa_3}\right)^2 + \frac{3h\nu_e}{16\sqrt{2}}\frac{\left(n_1^2-n_3^2\right)^2}{\left(n_1^2+n_3^2\right)^{3/2}}, \tag{4.2}$$

where A_{131} is the Hamaker constant for the interaction of material 1 (COM) with material 1 across a dielectric medium, material 3 (water). Table 4.1 shows the index of refraction values as a function of optical direction and wavelength for COM which were used in a prior Hamaker constant calculation based solely on electronic polarization [Ada91]. In

Table 4.1. Index of refraction for COM as a function of optical direction and wavelength [Pal51].

Optical Direction	Wavelength (nm)		
	535.0	589.0	670.8
α	1.4939	1.4909	1.4878
β	1.5599	1.554	1.5513
γ	1.6567	1.6502	1.645

equation (4.2), the second term on the right hand side accounts for electronic polarization while the first term accommodates static polarization terms.

Before using the Tabor-Winterton relationship, absorption data in the microwave and infrared (IR) region of the electromagnetic spectrum is needed if the static dielectric constant is much larger than the dielectric constant (i.e., n^2) for electronic polarization. The absorption in the IR often can be extrapolated to zero frequency and hence the static dielectric constant of the material may be determined. The dielectric constant of a material can be deconvoluted from the dielectric properties of a composite using mixing rules, which are shown in Table 4.2 [8]. In the current work, the dielectric constant of a COM/silicone composite was measured and the COM dielectric constant was determined from dielectric mixing rules. Because the particles could not be grown to a large enough size to measure the single crystal properties and the production of large amounts of well-crystallized particles is inefficient and time consuming, composites as a function of solids loading of the dispersed COM particles in a matrix of known dielectric constant, Eccosil® 5019, were produced to measure the dielectric properties of COM. A number of silane coupling agents were examined to determine which material best dispersed COM in silicone. The dielectric constant was then used to calculate the Hamaker constant of COM using equations (4.1) or (4.2).

4.2 Materials and Methods

COM particles were produced by the procedure described in Chapter 3.2.1.1. COM powder was dispersed in silicone (Eccosil® 5019, Emerson and Cuming™, Inc., Woburn, MA), using the silane coupling agents (Petrarch Systems Inc., Bristol, PA. The COM particles must be homogeneously dispersed in the matrix to be properly described by the composite mixing rules. In order to achieve good COM particle dispersion in the silicone matrix, a number of silane coupling agents were tested: 3-aminopropyltriethoxysilane (APTES); 2-(3,4 epoxycyclohexyl) ethyltrimethoxysilane

Table 4.2. The composite mixing rules evaluated, where κ is the is the static dielectric constant of the composite and v_c and v_d are the volume fractions of the continuous and dispersed phases, respectively, and κ_c and κ_d are the static dielectric constants for the continuous and dispersed phases, respectively.

Mixing Rule	Mathematic Relationship
Series	$\kappa = v_d\kappa_d + v_c\kappa_c$
Parallel	$\frac{1}{\kappa} = \frac{1}{\kappa_d} + \frac{1}{\kappa_c}$
Maxwell	$\kappa = \frac{v_c\kappa_c\left(\frac{2}{3} + \frac{\kappa_d}{3\kappa_c}\right) + v_d\kappa_d}{v_c\left(\frac{2}{3} + \frac{\kappa_d}{3\kappa_c}\right) + v_d}$
Lichtenecker	$\log(\kappa) = v_d \log(\kappa_d) + v_c \log(\kappa_c)$

(ECHEMS); (3-glycidoxypropyl) trimethoxysilane (GPTMS); isobutyltrimethoxysilane (IBTMS); 3-methacryloxypropyltrimethoxysilane (MPS); 3-(n-styrylmethyl-2-aminoethylamino) propyltrimethoxysilane hydrochloride (SMAEPS); and vinyltriacetoxysilane (VAS). Table 4.3 shows the molecular structures of the silane coupling agents. A typical grafting solution to graft the coupling agent to COM surfaces consisted of 0.6 M coupling agent, 0.33 M methanol, 0.002 M acetic acid, 0.00285 M deionized water, and 9.4 M toluene was prepared and equilibrated for 1 hour at 25°C. 0.05 g of COM crystals was added to the solution containing the coupling agent and sonicated for 1 minute. One hour after sonication the particles were filtered from solution using 0.22 μm filter paper. The crystals were dried overnight under vacuum.

It is important that the COM particles are well-dispersed in the silicone rubber matrix. Therefore, low solids loading (~0.01 v/o solids) samples were prepared with COM particles with each of the grafted coupling agents in the silicone rubber by hand mixing. A drop of the low solids loading mixture was placed on a glass serological ring slide, a cover slip placed over the ring and the composite mixture allowed to cure in place. The relatively transparent composites were then examined with optical microscopy to evaluate which silane coupling agent was most effective in dispersing the COM particles in the silicon rubber.

COM crystals with the silane coupling agent which gave the best dispersion in the preliminary experiments were mixed with Eccosil® 5019 in concentrations of 10, 20, 25, and 30 volume percent and cast into 22 mm diameter pellets approximately 4 mm thick. The samples were cured at room temperature under a vacuum to remove any entrapped air. Final samples were cut from the 22 mm pellets using a 5 mm diameter brass cork borer. The samples were electroded using a conductive silver paint. A multi-frequency LCR meter (4274A, Hewlett Packard, Rockville, MD) was used in conjunction with a computer controlled temperature chamber (MK 2300, Delta Design Inc., San Diego, CA) to measure the capacitance and dissipation factor as a function of temperature and

Table 4.3. Molecular structures of the silane coupling agents used to disperse COM in Eccosil® 5019 silicone.

Product Acronym	Molecular Name	Molecular Structure
APTES	3-aminopropyltriethoxysilane	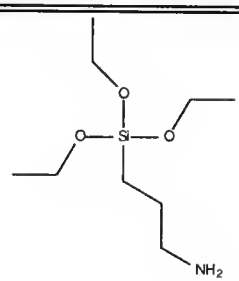
ECHEMS	2-(3,4-epoxycyclohexyl) ethyltrimethoxysilane	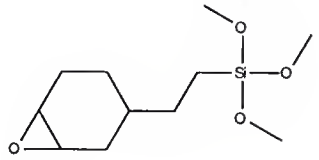
GPTMS	3-(glycidopropyl)trimethoxysilane	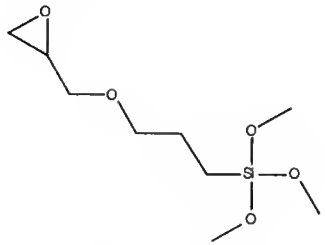
IBTMS	isobutyltrimethoxysilane	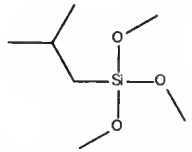

Table 4.3 (cont.).

Product Acronym	Molecular Name	Molecular Structure
MPS	3-methacryloxypropyltrimethoxysilane	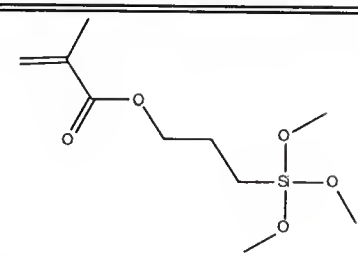
SMAEPS	3-(n-styrylmethyl-2-aminoethylamino) propyltrimethoxysilane hydrochloride	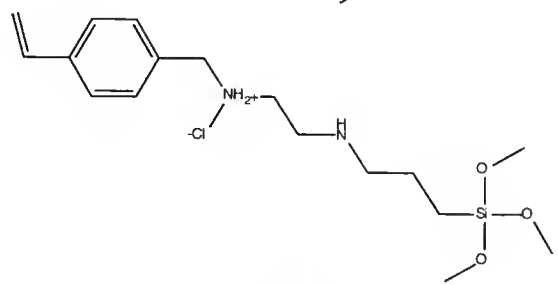
VAS	vinyltriacetoxysilane	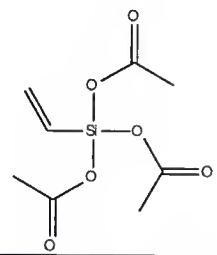

frequency (~100 Hz to 1 MHz). The equipment calculates dielectric permittivity from the capacitance, sample geometry, and permittivity of air. All measurements followed the American Standards and Testing Materials (ASTM) designation D150-81. An extrapolation to zero frequency gave the value of the dielectric constant at the "static" frequency for the composite, κ_1. The dielectric constant of Eccosil® 5019 at 1 MHz is 2.8. The dielectric constant of water at 37°C is 73.4 [Arc90].

Based on the solids loading of COM crystals in the polymer, a suitable mixing rule was used to deconvolute the composite properties into the particle and polymer dielectric properties [Yar87]. Four different composite mixing rules, series, parallel, Maxwell's, and Lichtenecker's (or logarithmic), were used to determine the static dielectric constant for COM. The mixing rule giving the best fit to the data was used in the final calculation of the COM Hamaker constant. The fit was performed using the Math Curve Fitter in SigmaPlot® version 5 for Macintosh software (Jandel Scientific, San Rafael, CA).

Values of refractive index as a function of frequency were used to construct Cauchy plots for each optical direction of COM and for water [Pal51]. A straight line fit to the data yielded a linear equation from which values of the main electronic absorption frequency typically in the UV, ν_{uv}, the dielectric constant at the UV characteristic frequency, ε_{uv}, and the index of refraction at the characteristic frequency, n_o, were determined.

The values of refractive index and dielectric constant were substituted into equation (4.2) to determine the Hamaker constants of COM crystals interacting with like optical directions (i.e., for interactions such as αCOM-H_2O-αCOM). The index of refraction of water at 37°C is 1.322 [Tho85]. Equation (4.1) was used to calculate Hamaker constants of COM crystals interacting with unlike optical directions (i.e., for interactions such as αCOM-H_2O-βCOM).

4.3 Results and Discussion

Figure 4.1 shows SEM micrographs of some of the COM particle dispersions in Eccosil® 5019. Relatively poor dispersion was exhibited by COM in Eccosil® in the absence of a coupling agent, as shown in Figure 4.1a. The COM particles were unevenly distributed throughout the matrix, and a large number of small agglomerates were present. Figure 4.1b shows the sample containing SMAEPS coupling agent. Very poor dispersion was obtained in this case, as indicated by the gray area on the right of the photomicrograph, which is a large mass of agglomerated COM particles. This is because the probably styryl group reacts poorly with the silicone rubber matrix as well as the charged groups (Table 4.3). This composite was obviously inhomogeneous and not suitable for dielectric measurement. The best dispersion of COM in Eccosil® resulted from the use of GPTMS, as shown in Figure 4.1c. This coupling agent has a glycido group which reacts favorably with the silicon rubber matrix. The GPTMS sample was composed of a relatively high number concentration of particles evenly distributed throughout the sample. All other COM particles treated with the coupling agents in Table 4.3 did not provide as good dispersion as the GPTMS. Therefore the coupling agent GPTMS was used in the remainder of the experiments for evaluation of the composite dielectric properties at higher solids loading.

The four composite rules of mixing used in the determination of the static dielectric constant are shown in Table 4.2. The rules were evaluated for their ability to deconvolute the dielectric constant of COM from COM/silicone composite properties. Figure 4.2 shows the fits of all of the mixing rules to the experimental data. Based on the minimization of the sum of squared differences between the measured and predicted values generated using the SigmaPlot® software, the series relationship gave the best fit overall. The dielectric value generated for the parallel mixing rule, 7.8×10^6, is not physically relevant, therefore this particular mixing rule was discarded. Table 4.4 gives

(A)

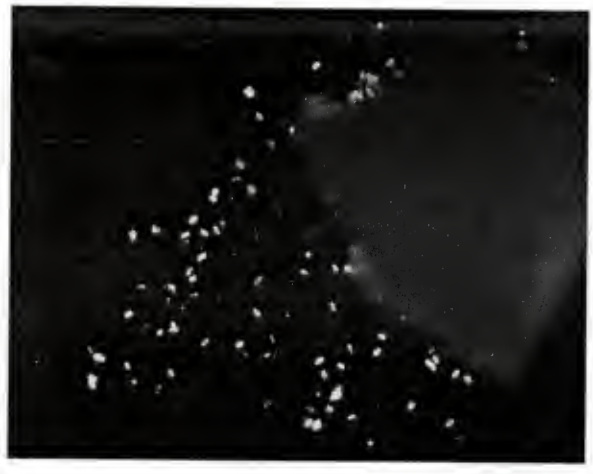

(B)

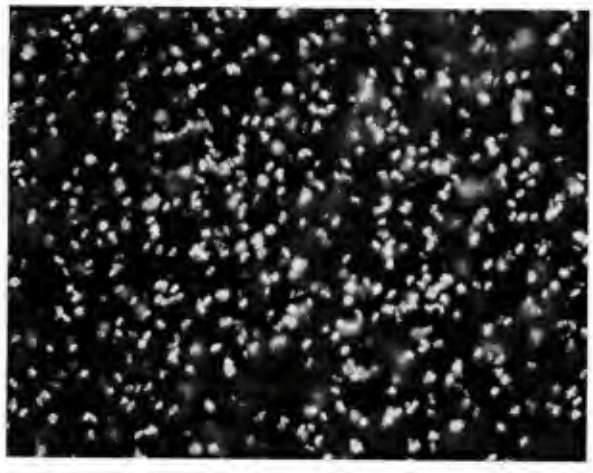

(C)

Figure 4.1. Optical photomicrographs of COM particles dispersed in Eccosil® 5019 using (A) no coupling agent, (B) SMAEPS coupling agent, and (C) GPTMS coupling agent (bar=100 μm).

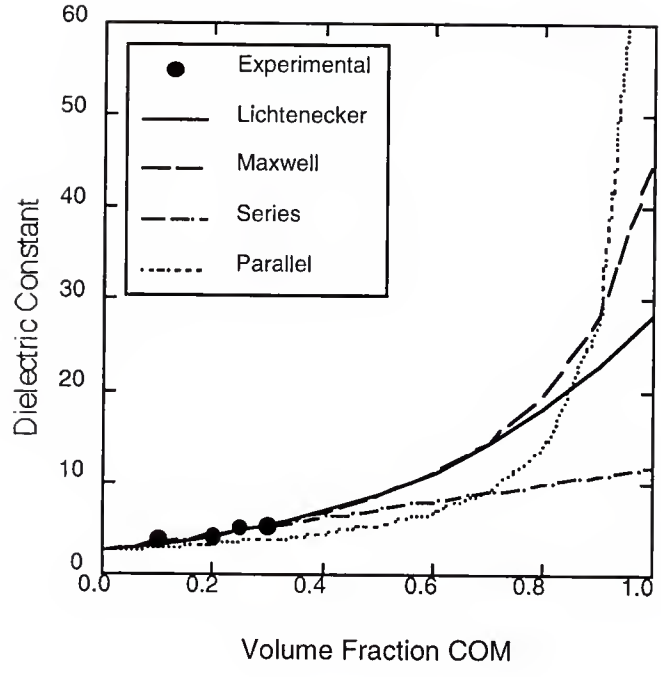

Figure 4.2. The composite mixing rules fit to experimental dielectric data.

Table 4.4. Dielectric constant values of COM determined by fitting the mixing rules to the experimental data.

	Composite Mixing Rule			
	Lichtenecker	Maxwell	parallel	series
Dielectric Constant	28.9	46.1	7800000	11.8
Regression Coefficient	0.75	0.77	NA	0.80

NA-not applicable

the values of the dielectric constants and the value of the nonlinear regression coefficient determined using a best fit of each of the above equations to the experimental data. The series model, although designed to represent the extreme case of alternating phases of a composite which are perpendicular to the electrode materials, gave the best description of the data, with a nonlinear regression coefficient of 0.80. The composite, shown in Figure 4.1c, obviously should not be represented by the series mixing model. Maxwell's mixing model, which was theoretically derived to describe a matrix containing small spherical inclusions [Von54], may be a closer representation of the COM/silicone composite than the series model; although, COM particles are not spherical. Although the Lichtenecker model has been previously invoked to describe systems of irregularly shaped inclusions [Mon47] similar to the COM/silicone composite, in the present work it gave the lowest regression coefficient, 0.75.

The series, Maxwell, and Lichtenecker models describe similar dielectric behavior up to ~35 volume percent (v/o) dispersed phase. Above this concentration the differences between the models become discernible, however in this work none of the composites were prepared with a content exceeding 30 v/o mixtures of COM with silicone rubber were too viscous to cast samples above 30 v/o COM. A composite having a dispersed phase of ~50 v/o may be used to distinguish the series model from the Maxwell and Lichtenecker models. Furthermore, the Maxwell and Lichtenecker models may be discernible at ~80 v/o dispersed phase, where the deviation between models becomes larger. However, a homogeneous composite with more than a 40 v/o dispersed phase is very difficult to prepare and such a large content of dispersed phase may exceed the percolation limit of the composite.

A large discrepancy in dielectric constant of ~75% resulted from the series, Lichtenecker, and Maxwell mixing rules, however this translates to a difference of only ~10% (1.6×10^{-21} J) in a calculated Hamaker constant. Since the Lichtenecker model has been shown to describe composites of the COM/silicone type [Mon47], and given the

difficulty in preparing a composite with a large second phase content, the Lichtenecker mixing model was used to describe the composite dielectric properties.

In order to calculate the Hamaker constant using the Tabor-Winterton relationship, experimental data involving both the static dielectric response and the absorption spectra in the ultraviolet frequency regime ($\omega > 10^{16}$ rad/s) must be known [Hou80]. Plots of $[n(\omega)^2-1]$ vs. $[(n(\omega)^2-1)*\omega]$, known as Cauchy plots [Hou80], were constructed for each optical direction of COM and for water, as shown in Figure 4.3. The Cauchy plot gives a straight line with slope equal to $1/\omega_{uv}^2$ and intercept equal to c_{uv}, where ω_{uv} (rad/s) is the characteristic frequency in the ultraviolet region of the electromagnetic spectrum and c_{uv} is the oscillator strength. The corresponding refractive index and dielectric constant at the UV characteristic frequency were determined using the equations [Hou80],

$$c_{uv} = n_o^2 - 1 \tag{4.3}$$

and

$$\varepsilon_{uv} = n_o^2, \tag{4.4}$$

respectively. All of the linear regression coefficients of the line fit were between 0.98 and 1. Table 4.5 gives the values of UV characteristic frequency, the dielectric constant at the UV characteristic frequency, and the index of refraction at the UV characteristic frequency for water and the three optical directions of COM. The dielectric data determined for water compares very well with the values determined by Hough and White [Hou80].

Because large absorbance exist at frequencies lower than 10^{16} rad/s for COM, the value of ε_{uv} determined from optical data will estimate the constant (i.e., the value of $(\varepsilon_o - n^2)$ is significantly larger than zero). When the static dielectric constant is significantly larger than the dielectric constant in the visible the infrared term, n^2, of the absorption

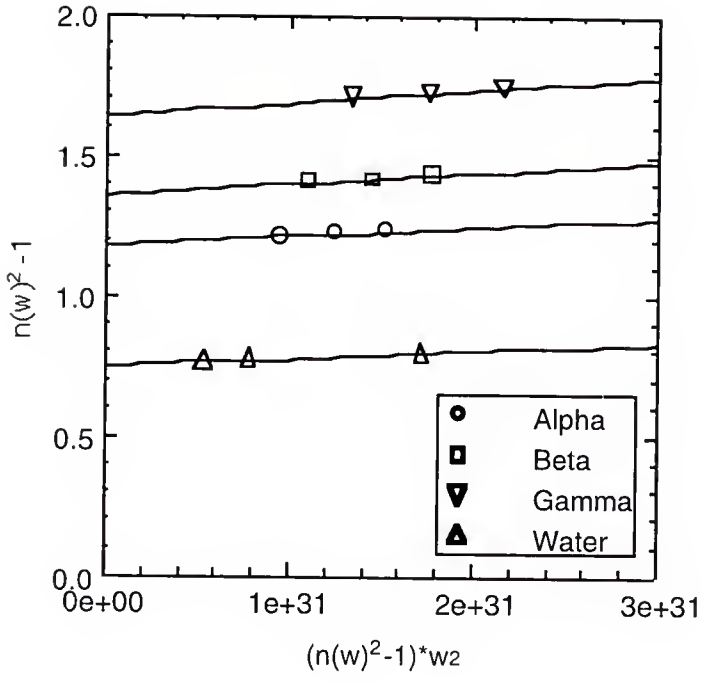

Figure 4.3. Cauchy plots for water and COM as a function of optical direction.

Table 4.5. Calculated values of the UV characteristic frequency and corresponding dielectric constants and refractive indices as a function of crystallographic direction determined from Cauchy plots.

Material	ω_{uv} ($x10^{16}$ rad/s)	ν_{uv} ($x10^{15}$ Hz)	ε_{uv}	n_o
α-COM	1.77	2.8	2.183	1.477
β-COM	1.58	2.51	2.361	1.5376
γ-COM	1.46	2.32	2.642	1.625
water	1.87	2.98	1.7475	1.322

spectra cannot be ignored [4]. In the current calculations, the value of the Hamaker constant due to contributions at zero frequency (~$1.68x10^{-21}$ J) is less than one order of magnitude lower than the Hamaker constant due to contributions at higher frequencies, (~8-24)$x10^{-21}$ J. Due to the equally strong dependence on both the zero and non-zero frequency terms of the Tabor-Winterton relationship, measurement of the dielectric properties of the COM/silicone composite and subsequent deconvolution to the COM static dielectric constant is important.

The calculations were performed using the assumption made by Tabor and Winterton that the UV characteristic frequency of most materials is approximately $3x10^{15}$ Hz. The values of the characteristic frequency for COM and water, shown in Table 4.5, are slightly lower than the assumed value of Tabor and Winterton at (2.32-2.98)$x10^{15}$ Hz. This assumption led to an increase of 11% in the Hamaker constant over the value of the Hamaker constant calculated if the actual determined values of characteristic frequency for the interacting materials were averaged together.

Table 4.6 compares previously published values by Adair et al. [Ada91] to the current values calculated using the Tabor-Winterton relationship. The average current value of, 13.7 (±5.90)$x10^{-21}$ J, compares favorably to the previously published value of, 11.4 (±3.42)$x10^{-21}$ J. Thus the addition of the static dielectric constant increases the Hamaker constant by about 15 percent. The improved accuracy of the COM Hamaker constant will allow increased reliability and confidence in calculating COM aggregation stability in the urinary environment.

4.4 Conclusions

The Hamaker constant of COM was determined using the Tabor-Winterton relationship. The dielectric constant of COM was deconvoluted from a COM/silicone composite using various mixing rules. The series mixing rule yielded the highest nonlinear regression coefficient, however the composites were clearly not representative of the

series model. Therefore the Lichtenecker model, previously shown to describe irregularly shaped inclusions in a matrix [Mon47], was used and a value of 28.9 for the COM dielectric constant was determined. Plots of refractive index as a function of optical direction and wavelength were used to generate the ultraviolet absorption frequency and the dielectric and refractive index at the UV absorption frequency for use in the Hamaker constant calculation. The resulting value of the Hamaker constant, 13.7 ($\pm$5.90)x10^{-21} J, compares well with previously published values of 11.4 ($\pm$3.42)x10^{-21} J determined using the Gregory approximation.

Table 4.6. Comparison of A_{131} calculated for COM using Gregory's approximation vs. the Tabor-Winterton relationship. *Data taken from Adair et al.[Ada91].

Type of Interaction	A_{131} from Gregory's Approximation* ($x10^{-21}$ J)	A_{131} from Tabor-Winterton Relationship ($x10^{-21}$ J)
α-H_2O-α	7.13	6.98
β-H_2O-β	11.3	12.6
γ-H_2O-γ	16.3	23.5
α-H_2O-β	8.99	9.33
α-H_2O-γ	10.8	12.7
β-H_2O-γ	13.6	17.1
Average ± 95% Confidence Interval	11.4 ± 3.42 J	13.7 ± 5.90 J

CHAPTER 5
DEVELOPMENT OF THE DYNAMIC WET CELL AND STREAMING POTENTIAL MEASUREMENTS

5.1 Introduction

The study of adhering materials is fundamental and very broad in application. For example, the adhesion of Fe_2O_3 to a glass substrate with and without a layer of gelatin [Ryd95], of red blood cells to glass [Moh74], of human fibroblasts to glass [van92], of submicrometer particles to silicon [Bus93], and of bacteria to glass [Bus92] have all been measured using a hydrodynamic technique. Adhesion is particularly important in human kidney stone disease and other pathological biomineralization processes. Numerous studies have shown that the adhesion of calcium oxalate monohydrate (COM) particles to the wall of a kidney tubule may eventually lead to stone formation [Fin78a, Fin84, Kok90]. *In vivo* calcium oxalate particle attachment to a nephron wall has also been exhibited in a rat animal model [Kha91]. However, the actual mechanism(s) of adhesion within the biophysical environment of the human kidney is not well understood.

In past studies, researchers have used many techniques to evaluate adhesion [Vis76, Cor66, Zim82]. These include rotating discs [Kri94], packed columns [Kal87], centrifugation methods [Kor60], vibrating methods [Der61], the surface force apparatus [Isr78], and a hydrodynamic method utilizing parallel plates [Pel82, Pel84]. The most recent technique for measuring the force with which a particle adheres to a surface is the scanning probe microscope (SPM) [Duc91]. These and other adhesion techniques are best suited to specific material systems. Therefore, further discussion will be limited to only the hydrodynamic parallel-plate adhesion measuring technique, which is considered to be most suitable for the measurement of COM crystals in model biological systems.

Many researchers have studied COM crystals interacting with kidney cells using *in vitro* experiments [Big96, Man91, Man94, Lei96, Ebi95, Ver96]. However, these studies were static in nature, lacking the hydrodynamic conditions that are found in the human kidney. The current adhesion investigation employs a measuring technique which is applicable to the study of kidney stone disease because the flow can easily be changed from laminar to peristaltic, and nearly any eluent can be used for the interacting medium. Also, a number of different substrates may be used, ranging from individual protein layers to actual cells under aseptic conditions. The result of this measuring technique is a quantitative value of the force per unit area with which a crystal adheres to a substrate designated as the adhesive strength.

In the current study, an apparatus was developed based on the principles of the capillary adhesion technique reported by Pelton et al. [Pel84, Pel82] to measure the adhesive strength between polystyrene spheres and a Pyrex substrate. A similar device to the current dynamic wet cell was developed by Hochmuth et al. [Hoc73] and has been used in many investigations to study both attachment and removal of cellular material to specific surfaces [Moh74, van92, Dor77, For84, Tru90]. However, in the current investigation, the adhesion of COM particles to a model fused silica surface was measured.

The apparatus shown in Figure 5.1 consists of an adhesion chamber incorporating two fused quartz slides separated by a spacer. The eluent flows through the dynamic wet cell at a specified rate which is calibrated against the pump drive. A camera mounted above the adhesion cell, which is connected to a monitor and video cassette recorder, records activity in the cell during each experiment.

The linear particle velocity, v, at a distance of one particle radius from the cell wall is calculated using the Poiseuille equation

$$v = \frac{2Q\left(R^2 - r^2\right)}{\pi R^4} \tag{5.1}$$

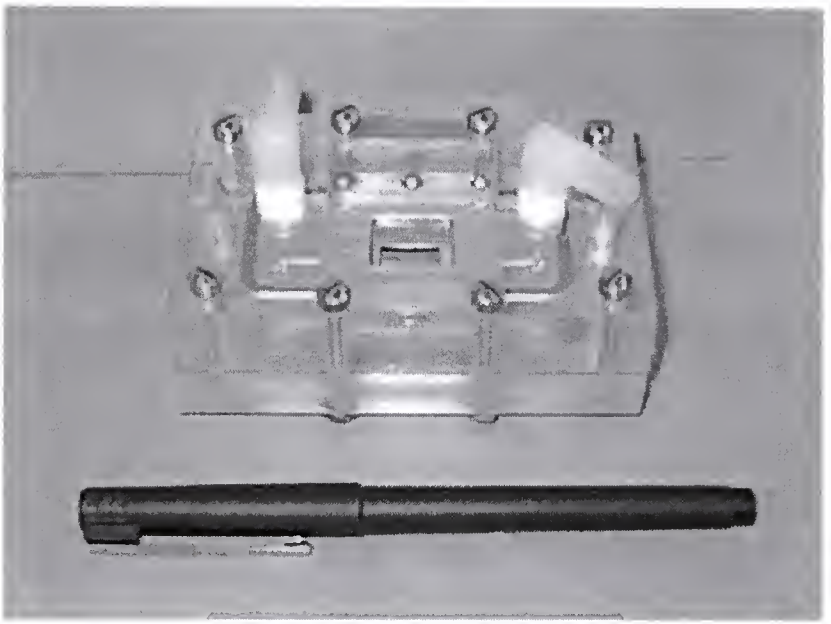

(A)

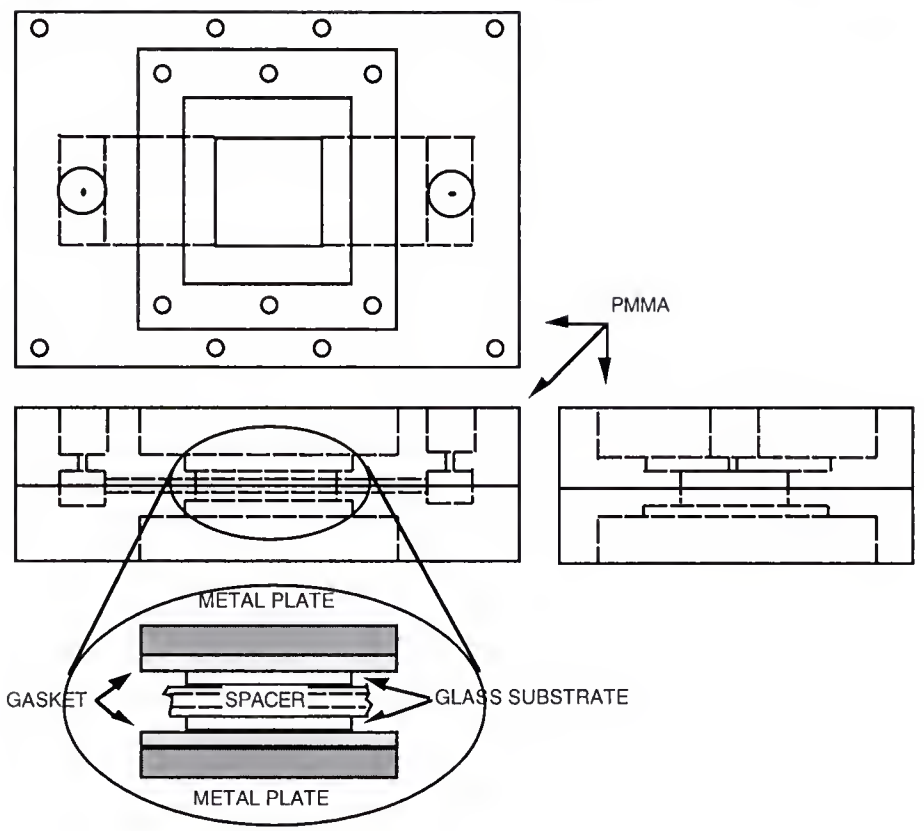

(B)

Figure 5.1. (A) A picture and (B) a schematic diagram of the dynamic wet cell developed to measure adhesion of particulate to surfaces. In (B), structural thru-holes have been omitted from the drawing to improve clarity.

where Q is the volumetric flow rate, r is the particle radius, and R is half the distance between the fused quartz slides. The corresponding displacement force acting at one particle radius, F_d, is calculated using the fluid properties, particle dimensions, and the calculated linear velocity from equation (5.1) using the formula [Gol67]

$$F_d = 1.7(6\pi\eta r v) \tag{5.2}$$

where η is the eluent viscosity, r is the particle radius, and v is the linear velocity.

An instrument to determine the zeta potential on a substrate by measuring the streaming potential was also developed to study the contribution of electrostatic interactions to the adhesion of COM to various substrates. The instrument was similar to the rectangular capillary used by van Wagenen and Andrade [van80] and was used to determine the charge on the surface of the substrate material, fused quartz, in saturated COM solution conditions.

5.2 Materials and Methods

5.2.1 Adhesion Measurements using the Dynamic Wet Cell

COM crystals prepared as described in Chapter 3 were used throughout the following adhesion experiments. A 0.2 volume percent (V/o) suspension of COM crystals in COM saturated solution was prepared and equilibrated in solution for 24 hours. Prior to assembly of the adhesion cell, the glass substrates were surface treated and a uniform silanol surface ensured [Ile79] by soaking in 1 M KOH, 1 M HNO_3, and 1 M KOH consecutively for 30 seconds each. Before and after each acid or base wash, the slides were washed with copious quantities of deionized water (>16 MΩ•cm). The treated slides were stored in deionized water until being used in the adhesion measurements.

Before adhesion measurements were performed, the COM suspension and the dynamic wet cell were equilibrated at 37°C using two temperature controlled water baths. During the adhesion experiment the dynamic wet cell and the eluent were maintained at 37°C. The suspension was sonicated for 3 minutes and shaken using a vortex mixer for 1 minute to minimize the presence of agglomerates. The suspension was then injected into the dynamic wet cell using an injection port adjacent to the entrance of the cell and the particles settled out of solution onto the spectroscopic grade, fused quartz substrate (CO Quartz, Esco Products, Oak Ridge, NJ) for 10 minutes. Given the size and density of the COM particles, 10 minutes is more than sufficient time for the COM particles to settle from solution based on the Stokes settling equation. Also, preliminary experiments showed that adhesion of COM to the fused quartz substrate did not change with increased residence time of contact between particle and glass before flow up to 60 minutes.

The number of particles adhering to the fused quartz as a function of flow rate was determined by videotaping the particles adhering to the lower substrate in the dynamic wet cell. A low light CCD camera (JE-3662HR, Javelin Electronics, Torrance, CA) was mounted to the eyepiece of the microscope head of a Rank Brothers electrophoresis device, normally configured to measure zeta potential in a capillary tube. In this case, the dynamic wet cell replaces the capillary tube. The total magnification of the microscope was 250x given by a 20x water immersion objective lens, 1.25x intermediate lens, and a 10x eyepiece. The camera output was connected to a video cassette recorder (Magnavox VR9342, Philips Consumer Electronics Co., Knoxville, TN) and to a real time video monitor (CVM14, Javelin Electronics, Torrance, CA). Taping proceeded continuously for the length of each experimental run. The flow rate was manually incrementally increased from 0 to 136 ml/min using a variable speed pump drive (Ismatec SA, Glattbrugg, Switzerland) with a gear pump (Micropump Corporation, Vancouver, WA). The high flow rates where necessary to produce shear stresses on the

COM particles between 3000 and 5000 Pa. An audio connection consisting of a microphone (Radio Shack 33-3003, Tandy Corporation, Fort Worth, TX) and microphone mixer (Radio Shack 32-1105A, Tandy Corporation, Fort Worth, TX) attached to the VCR and monitor allowed the operator to record the flow rate for subsequent analysis. The duration for each particular flow rate was approximately 1 minute. A picture and a schematic diagram of the dynamic wet cell supporting equipment are shown in Figure 5.2.

After completion of an adhesion experiment, the videotape was analyzed for the number of particles adhering to the substrate at each flow rate. An example of an experiment is illustrated in Figure 5.3. Also, the crystallographic orientation of each particle remaining after each particular flow rate was recorded. The force acting at one particle radius at each flow rate was calculated using equations (5.1) and (5.2) for particles in both the (010) and $(10\bar{1})$ particle orientation. The corresponding average strength on each particle was calculated using the displacement force and the average area of the crystal faces. The COM particles used in the current study have the specific ratio of crystallographic dimensions shown in Figure 5.4c. These ratios were determined from SEM analysis and used to calculate the average areas of the (010) and $(10\bar{1})$ crystallographic faces of the COM crystal which were both ~111 μm^2.

The COM crystallographic faces shown in Figure 5.4b were determined using x-ray data in the computer program SHAPE© (Shape Software, Kingsport, TN). Cody and Cody [Cod94] had previously indexed the faces correctly for the morphology of COM particles used in the experiments, which aided in the modeling. The fractional coordinates published by Cocco [Coc61] were input to the computer program ATOMS© (Shape Software, Kingsport, TN), to display the atomic structure as a function of crystallographic habit, as shown in Figure 5.5.

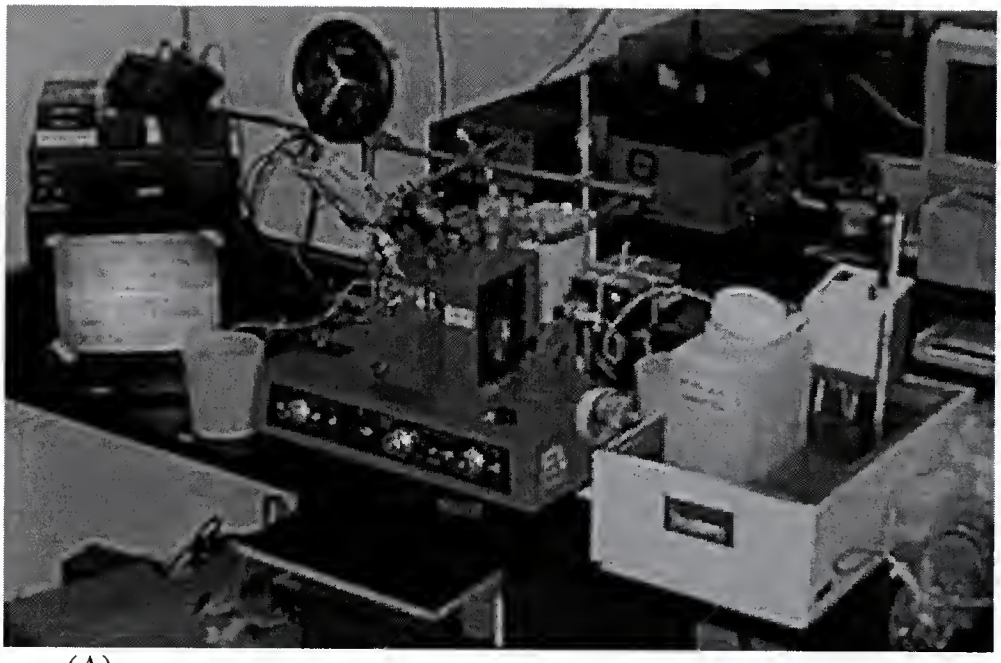

(A)

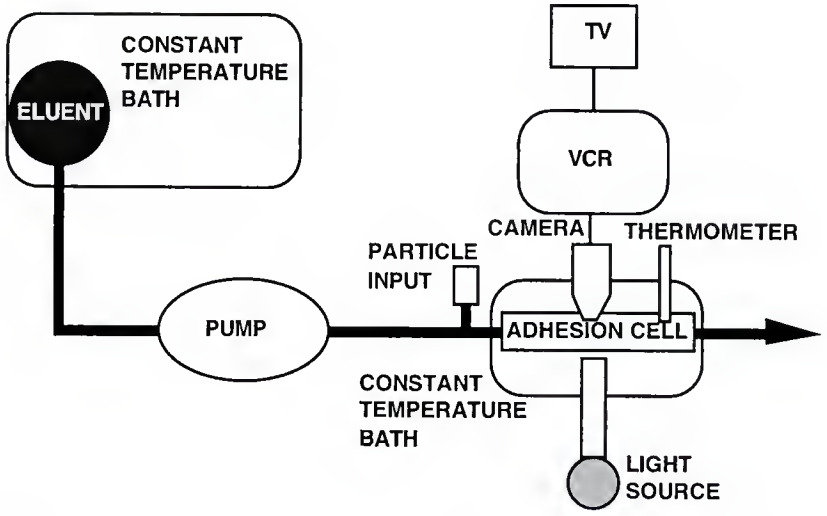

(B)

Figure 5.2. (A) A picture and (B) a schematic diagram of the dynamic wet cell supporting equipment.

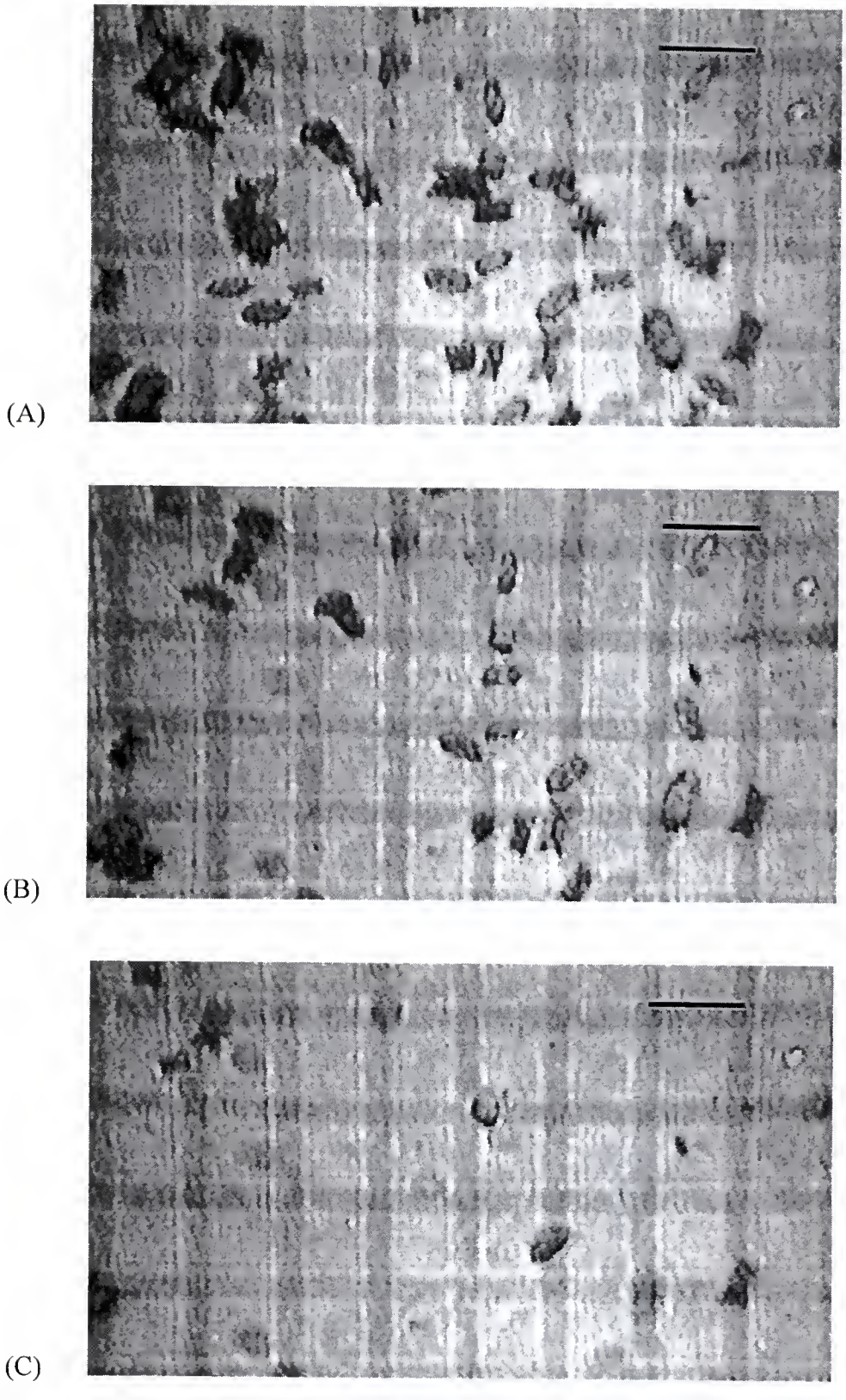

Figure 5.3. A time lapse sequence of events during an adhesion experiment. The flow rates are (A) 12 ml/min, (B) 53 ml/min, and (C) 108ml/min. (bar = 40 μm)

(A)

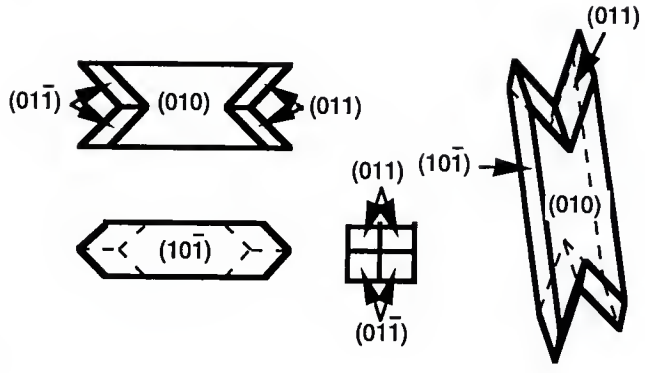

(B)

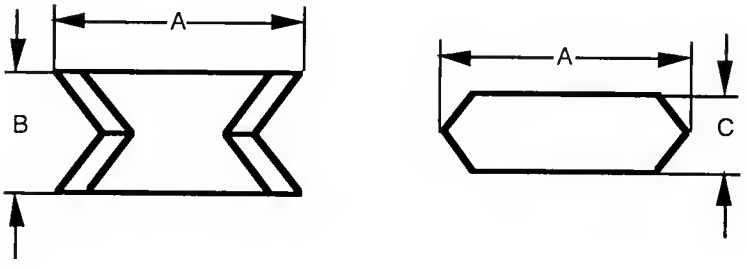

(C) A:B:C=1.0:0.43:0.35

Figure 5.4. COM particles of controlled morphology shown in a (A) scanning electron micrograph, (B) modeled using SHAPE© software showing the two dominant crystallographic faces, (010) and (10$\bar{1}$), and (C) demonstrating the relative crystallographic size ratios.

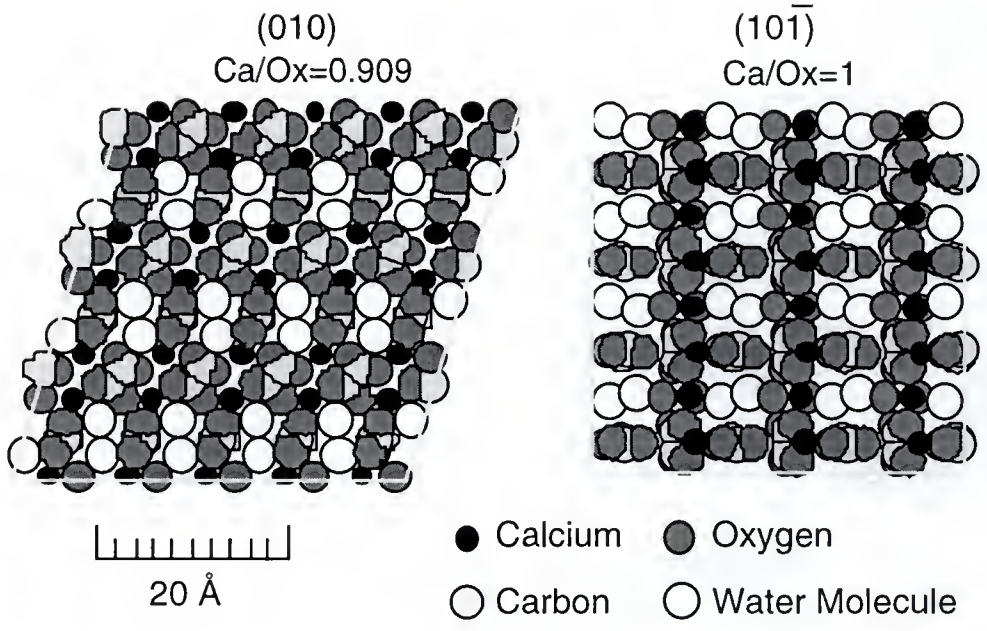

Figure 5.5. Theoretical (010) and (10$\bar{1}$) crystallographic planes of calcium oxalate monohydrate. The $Ca^{2+}/C_2O_4^{2-}$ ratio is given above each theoretical atomic structure.

5.2.2 Streaming Potential Measurement

The zeta potential of the fused quartz substrates was determined using a streaming potential instrument which was built in the laboratory. The streaming capillary consisted of two blocks of polymethylmethacrylate machine into the configuration shown in Figure 5.6. The cross sectional area of the rectangular capillary is 0.448 cm^2. The streaming cell was designed to use the same size substrates that are used in the dynamic wet cell. The only difference being the streaming cell used two more slides to increase the surface area interacting with the solution.

A platinum electrode is placed on each side of the streaming capillary shown in Figure 5.6 to measure the potential difference across the streaming channel. The electrodes consisted of woven platinum mesh. The leads to the electrodes are platinum wire and are woven into the mesh to eliminate any potentials which might arise due to soldering with another metal causing a galvanic cell. The platinum electrodes were blackened using a solution of 2% chloroplatanic acid (YSI 3140, YSI Incorporated, Yellow Springs, OH). Blackening is the process of depositing colloidal platinum on the surface of the platinum electrodes to increase the overall surface area and increase the sensitivity.

The electrodes were connected to a high impedance electrometer, $5x10^{13}$ Ω, (614 Electrometer, Keithly Instruments, Inc., Cleveland, OH). The output of the electrometer was connected to a resistance-capacitance (RC) circuit shown in Figure 5.7. The circuit developed by Horn and Onoda [Hor77] is used to subtract potentials due to asymmetrical electrodes and/or electrode polarization of the electrolyte. The output of the RC circuit is connected to a strip chart recorder to record the streaming potential. Figure 5.8 is a picture the actual instrument and a schematic diagram of the streaming potential instrument.

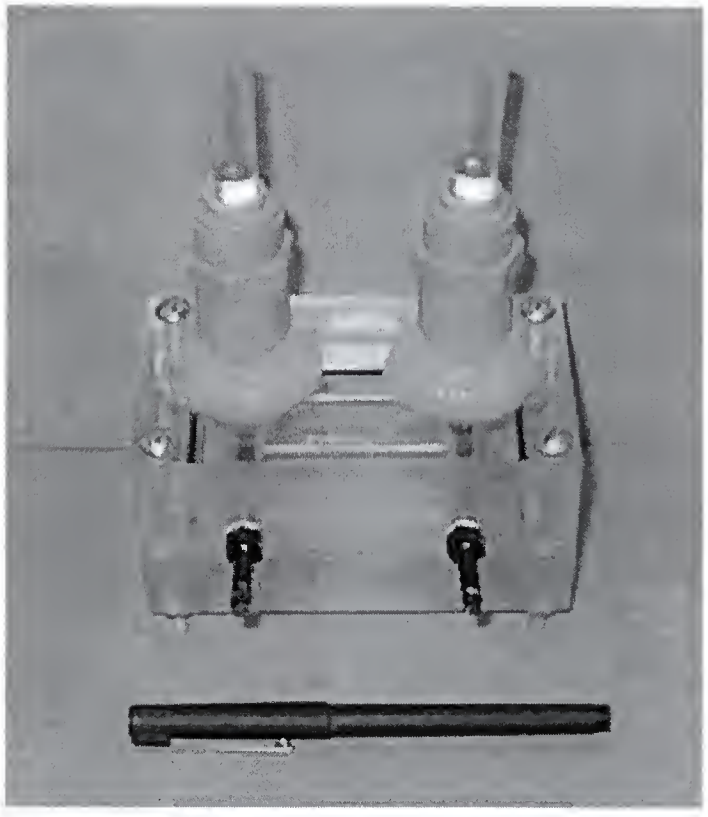

(A)

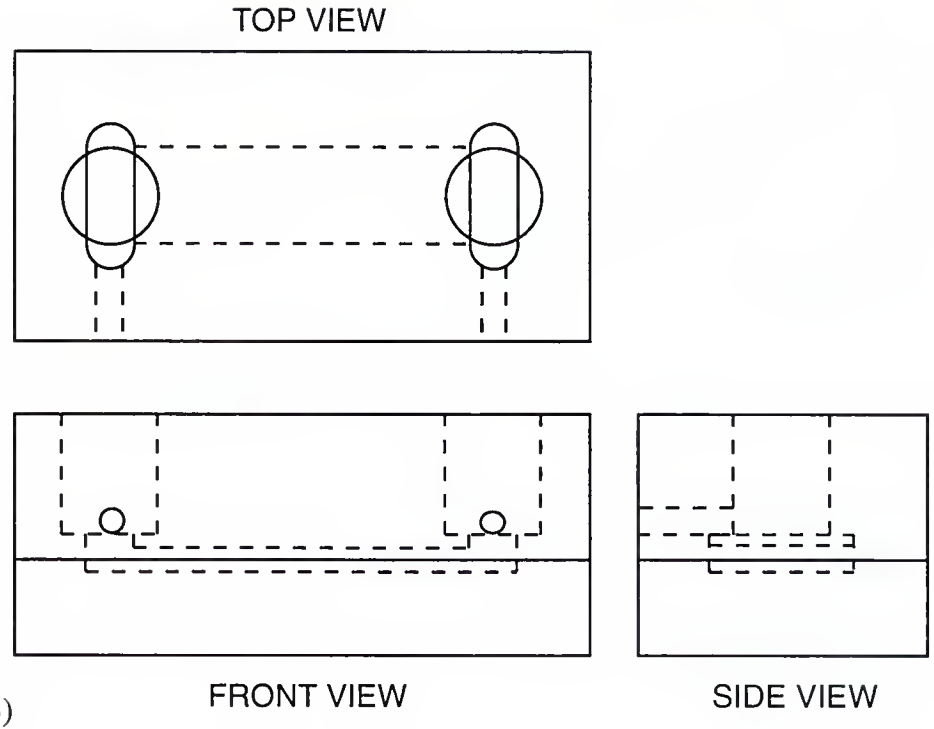

(B)

Figure 5.6. A (A) picture and a (B) schematic diagram of the streaming potential cell.

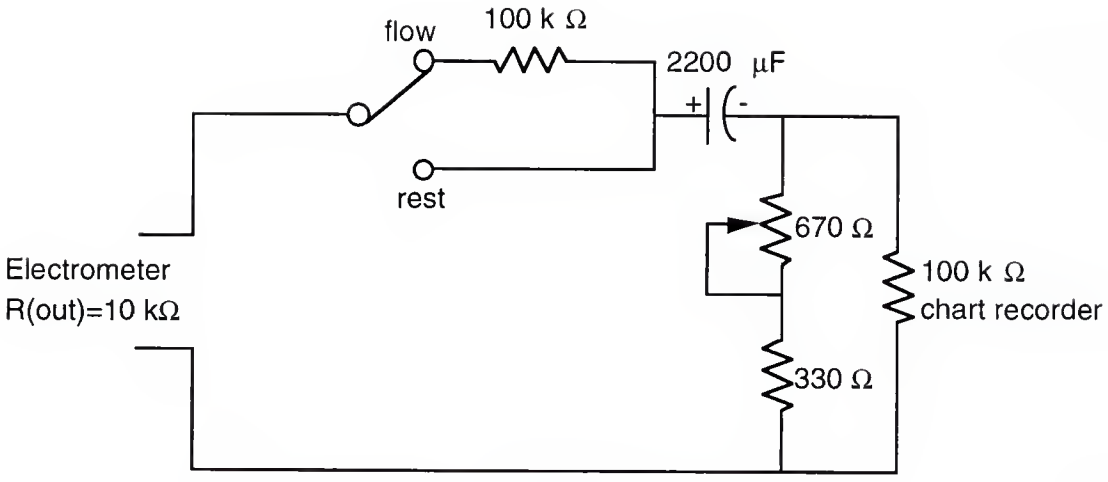

Figure 5.7. A diagram of the R-C circuit used to eliminate asymmetry and electrode polarizations [Hor77].

(A)

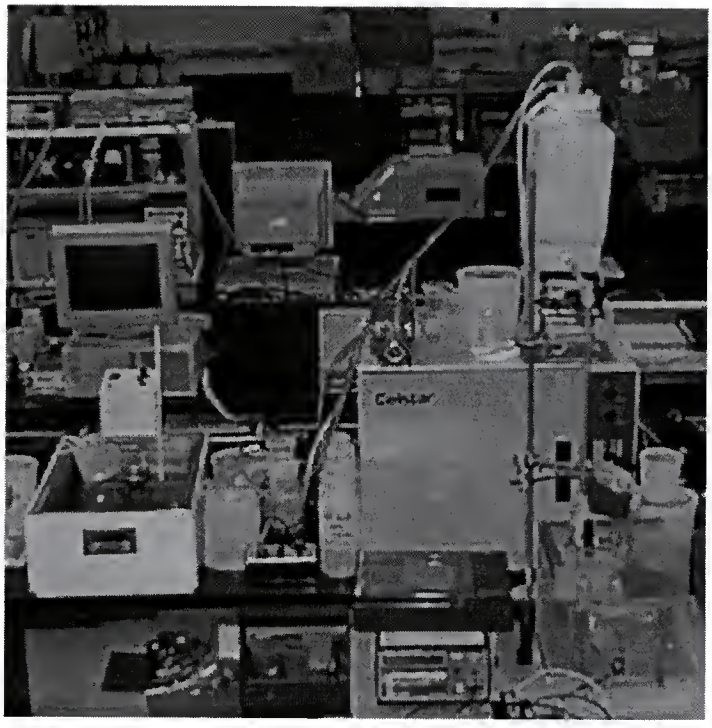

(B)

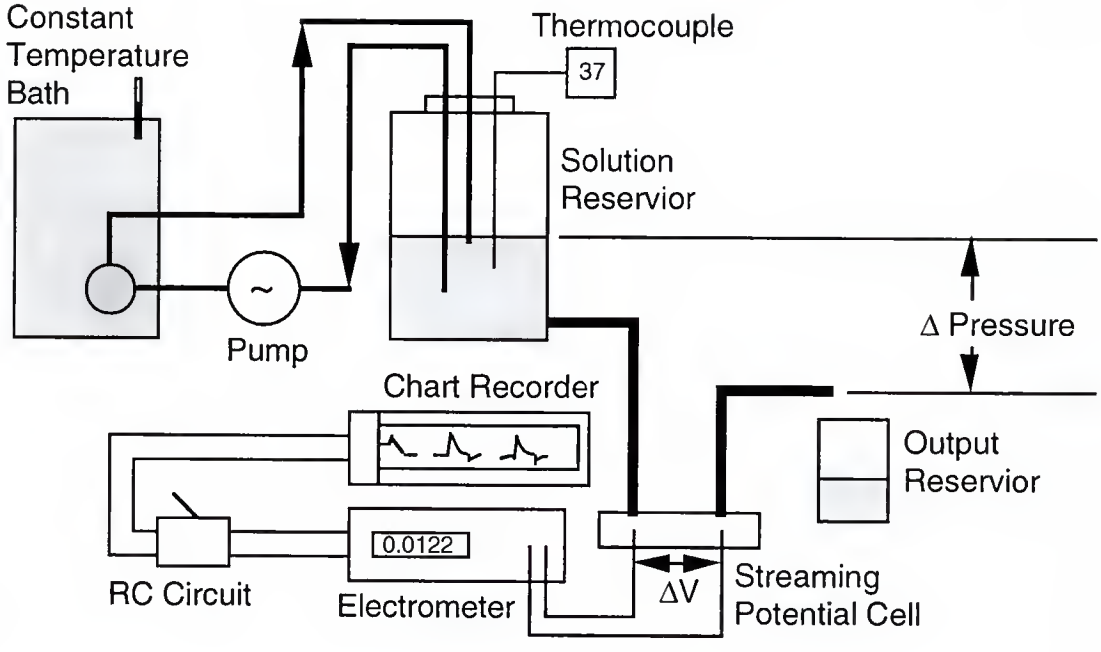

Figure 5.8. (A) A picture and (B) a schematic diagram of the streaming potential instrument including all of the supporting equipment: solution reservoir, streaming cell or capillary, solution collection reservoir, electrometer, R-C circuit, strip chart recorder, peristaltic pump, constant temperature bath, recirculating vessel, and thermocouple.

Streaming potentials, V_s, were recorded for various differences in pressure, ΔP, across the streaming capillary given by the difference in the pressure head of the holding reservoir and the output of the tubing as shown in Figure 5.8. The different pressures were calculated using the equation [Esk68]

$$\Delta P = \rho g \Delta h \tag{5.3}$$

where ρ is the density of H_2O at 37°C, 0.99375 g/cm^3 [Lid90], g is the acceleration due to gravity, and Δh is the measured height difference of pressure head and outlet. The only pressure drop in the system was assumed to be across the streaming capillary because the cross sectional area of that region was 65% smaller than the next smallest cross section in the system. The pressures were varied from 0.33 to 3.56 cm Hg. The resulting streaming potentials generated from the electrolyte flow were recorded. The streaming potential measurements were recorded at the unadjusted pH of the eluent (pH≈5.7) in COM saturated solution, at a temperature of 37±1°C.

To determine the effect of surface conduction a conductance meter (YSI Model 32, YSI Incorporated, Yellow Springs, OH) was connected across the streaming capillary. The bulk solution conductivity was measured using the same conductance meter and a conductivity probe (YSI 8417, YSI Incorporated, Yellow Springs, OH) having a cell constant of 1/cm.

From experimentally determined values of ΔP and V_s and material and liquid parameters, the zeta potential of the substrate was calculated using equation 2.6. Constants used in the calculation are shown in Table 5.1.

Streaming potential was also performed on the same fused quartz substrates using a commercial apparatus (PAAR EKA-Electro Kinetic Analyzer RV 4.0, Brookhaven Instruments Corporation, Holtsville, NY) yielding similar results.

Table 5.1 A list of the physical parameters necessary to calculate zeta potential from streaming potential.

Physical Parameters	Values
Temperature (°C)	37
Viscosity (Poise) [Lid90]	0.006917
Density (g/cm^3) [Lid90]	0.993075
Dielectric Constant [Lid90]	73.2
Specific Conductivity ($1/\Omega \cdot cm$)	2.48×10^{-6}

5.3 Results and Discussion

5.3.1 Dynamic Wet Cell

The dynamic wet cell was machined out of two pieces of poly (methyl-methacrylate) (PMMA) and is sealed with a rubber o-ring between the top and bottom of the cell. The entire dynamic wet cell was assembled as if an experiment was being performed and the volumetric flow rate as a function of dial number on the metered gear pump was calibrated. Figure 5.9 is a plot of dial setting on the metering pump vs. volumetric flow rate. The error bars represent the standard deviation for 5 individual experiments. A line was fit to the data to simplify the calculation of force and stress at a given flow rate or pump dial setting. The equation of the line is $y = 75.99x - 4.35$ and the least squared linear regression coefficient, r^2, is 0.9983. The fact that the intercept of the line is negative leads to a small underestimation in the applied hydrodynamic force of a few Pascals.

The dynamic wet cell was fashioned to promote laminar flow across most of the length of the cell. A reservoir was placed before and after the actual adhesion section of the cell to allow flow to enter the adhesion area with as little perturbation as possible. Reynolds numbers, R_e, were calculated for the range of flow rates and are shown in Figure 5.10 using the equation [van92a]

$$R_e = \rho \frac{Q}{(w+2h)\cdot \mu} \tag{5.4}$$

where Q is the volumetric flow rate, ρ is the fluid density, μ is the viscosity, w is the width of the flow chamber, and h is the half the distance between the parallel plates. As can be seen in Figure 5.10 the Reynolds numbers climb as high as 200 for the highest flow

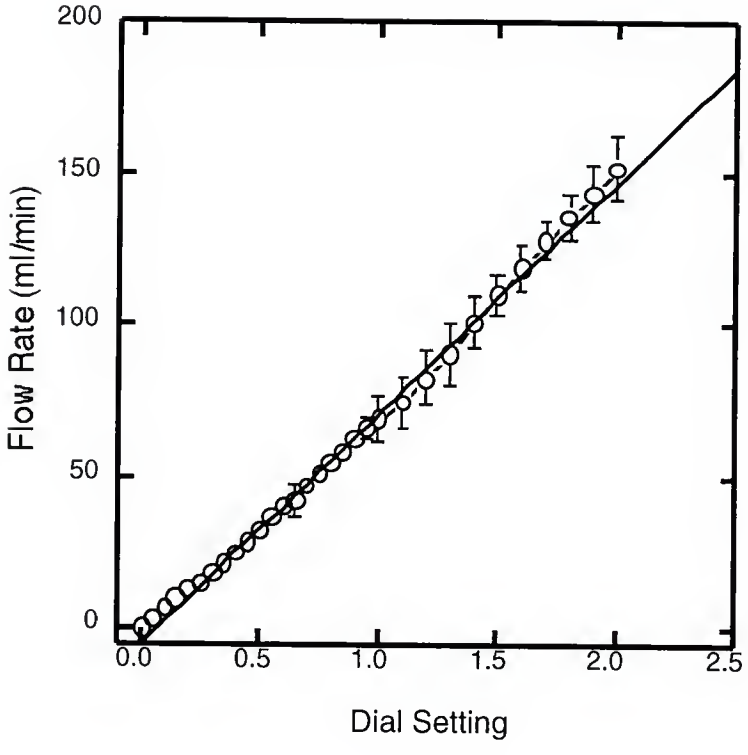

Figure 5.9. A plot of dial setting vs. volumetric flow rate used to calibrate the pump. The error bars represent the standard deviation of five individual experiments.

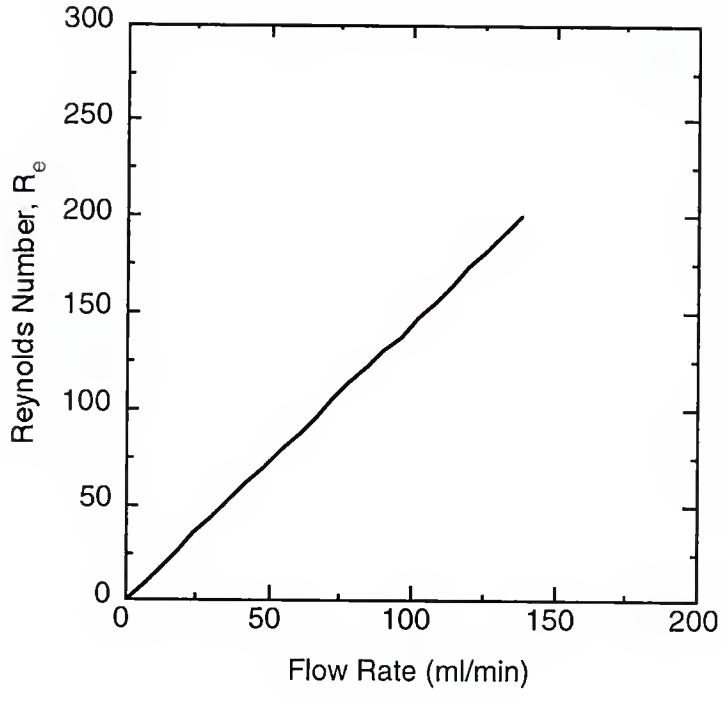

Figure 5.10. A plot of flow rate versus Reynolds number indicating the stable flow inside the dynamic wet cell at all experimental flow rates

rates achieved, 150 ml/min. Since the critical Reynolds number for laminar flow is approximately 2,300, every experimental flow rate produced laminar flow [Esk68]. Further calculations were performed to determine the distance into the cell for the flow to become laminar, L_e, at increasing flow rates using the equation [van92]

$$L_e = 0.026hR_e. \tag{5.5}$$

At the highest experimental flow rates, 150 ml/min, the calculations showed that a distance of 2.1 mm was necessary for the flow to become laminar. No particles within 4 mm of the inlet side of the flow chamber were measured.

5.3.2 Model COM Particles

COM particles with an average equivalent spherical diameter of 13.0 μm were produced. The particle size standard deviation was relatively narrow at 1.3 μm. To simplify the calculations of adhesion strength, the particle size was assumed to be monodisperse.

The experimental zeta potentials shown in Figure 5.11 demonstrate that the surface charge of the COM crystals is negative over the pH range investigated. This finding is not consistent with the results of Curreri, Onoda, and Finlayson, [Cur79b] who showed the surface charge to be positive across most of the pH range at saturated conditions. The differences in surface charge may be due to the differences in crystal morphology. The particle morphology on which Curreri et al. [Cur79b] performed zeta potential measurements was an aggregate of poorly defined particles, while the particle morphology used in the current study is well defined. Boeve et al. [Boe94], also, reported similar values of COM zeta potential to those determined here. The zeta potential of COM determined by Boeve et al. [Boe94] was -5 mV at a pH of 6.1 and an ionic strength of 0.33 M. The differences in magnitude of the zeta potentials between

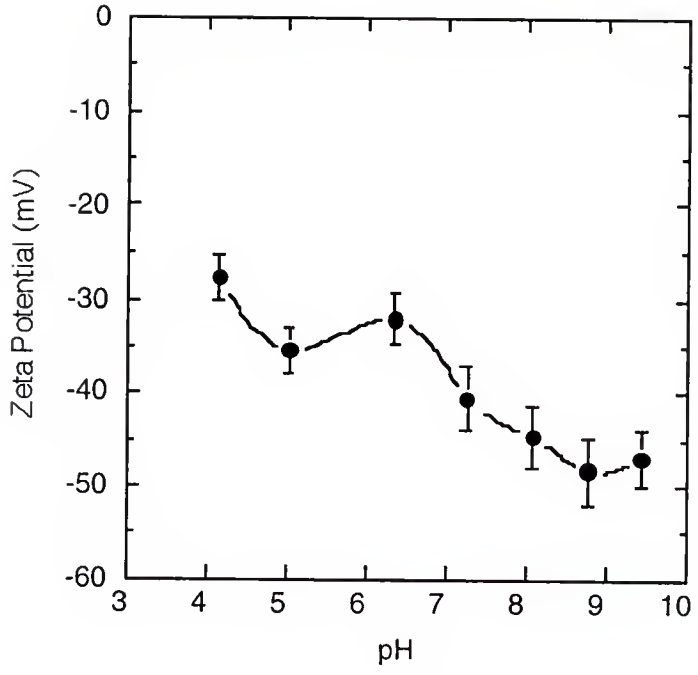

Figure 5.11. Experimentally determined zeta potential of COM particles in saturated calcium oxalate monohydrate solution. Each data point is the mean +/- 95% confidence interval. The ionic strength of the saturated COM solution was $8x10^{-6}$ M.

those currently measured and the potentials which Boeve et al. measured may be attributed to the differences in ionic strength. In the current investigation, the ionic strength of the COM saturated solution at 37°C is approximately $8x10^{-6}$ M determined using atomic absorption to measure the $[Ca^{2+}]$.

5.3.3 Streaming Potential

Just as flow dynamics were important in the development of the dynamic wet cell, they are also important for the measurement of streaming potential. Streaming potential theory utilizes the Poiseuille equations to describe laminar flow in a capillary. To determine if the flow in the currently developed streaming potential cell was laminar, Reynolds numbers were calculated for each driving pressure using the equations [Esk68]

$$u_{ave} = -\frac{h^2}{3\mu}\frac{\Delta P}{\Delta x} \tag{5.6}$$

and

$$R_e = \frac{\rho h u_{ave} \Delta P}{\mu} \tag{5.7}$$

where u_{ave} is the space average velocity. Figure 5.12 is a plot of the driving pressure vs. Reynolds number which shows that the flow is laminar even at the highest driving pressures, which is indicated by the Reynolds number being less than half of the critical Reynolds number of 2300.

A plot of ΔP vs. streaming potential was used to determine the experimental zeta potential of the fused quartz substrate as shown in Figure 5.13. A line fit to the data in Figure 5.13 has a least squared regression coefficient of 0.98 and an intercept of -3.88 mV. The good fit of the line is important because streaming potential is directly proportional

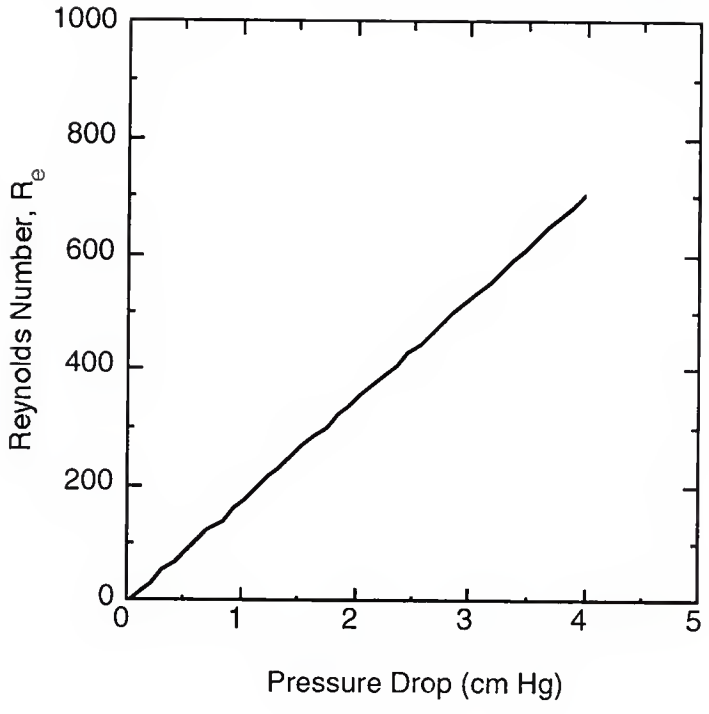

Figure 5.12. A plot of pressure drop or driving pressure across the streaming capillary indicating that the flow is laminar under all experimental flow conditions.

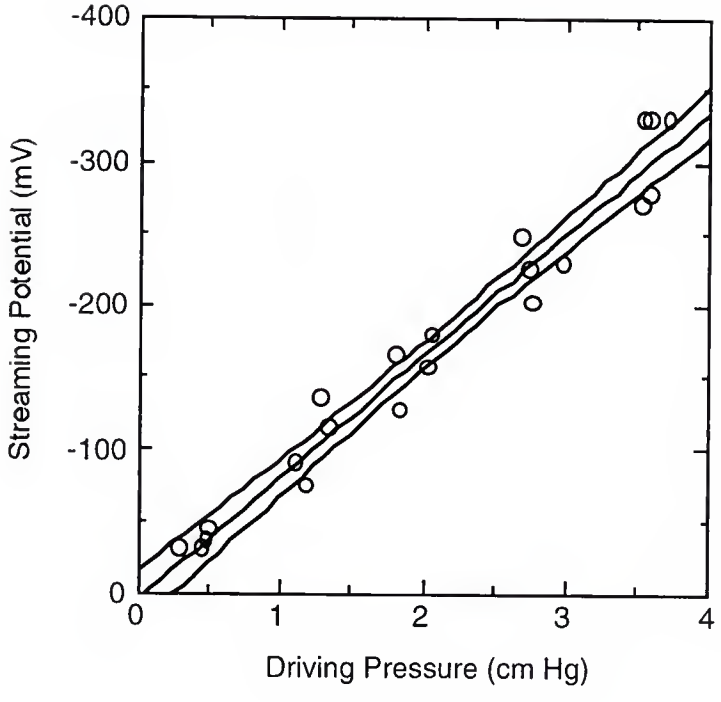

Figure 5.13. A plot of streaming potential vs. driving pressure for fused quartz in COM saturated solution showing a linear regression with an r^2=0.98 and 95% confidence limits.

to driving pressure (i.e., the pressure across the streaming potential capillary) as can be seen from equation 2.6. The fact that the intercept is low in magnitude is an indication of how well the background potentials are being eliminated using the circuitry of Horn and Onoda [Hor77, Bal73].

The zeta potential of the fused quartz substrate was measured to be -22±3 mV (mean±95% confidence interval) at 37°C and pH 5.7 using the previously described streaming potential instrument. The value of zeta potential would appear to be low when compared with other previously published values; however, the Brookhaven Instruments commercial streaming potential analyzer measured a zeta potential of -16.8±0.3 mV (mean±standard deviation) at 37°C and pH 6.8 on the same fused quartz material. Ranges of zeta potentials have been reported by various authors, such as -120 to -150 mV [Jon45] and -90 mV [Sca92] for similar ionic strength solution conditions on vitreous silica. Although the electrolyte concentration is similar to the experimentally used value, other authors used electrolytes which were 1:1 in valence of cation:valence to anion. Interestingly, many of the reports of zeta potential are determined at a single pressure. From the reported data one cannot determine if the experimental streaming potential is directly proportional with driving pressure or if the intercept is zero. Both of which are a must for accurate calculation of zeta potential according to Ball and Fuerstenau [Bal73].

Fairbrother and Mastin [Fai24] showed the zeta potential, -48 mV, to drop when using a $1x10^{-5}$ M 2:1 electrolyte. In the current experiments, the electrolyte, CaC_2O_4, is 2:2 in which both the co-ion and the counterion have a valence of 2. In coagulation theory, the electrolyte generally becomes a more effective coagulating agent when it contains multivalent ions. Also, the coagulation concentration is most importantly determined by the valency of the counterion [Hun93]. In the current case the counterion is Ca^{2+}. That is, as the valency of the electrolyte increases, the solution cannot support the charge and a decay of charge into the bulk solution occurs more rapidly, which is demonstrated in Figure 2.5.

As mentioned in Chapter 2.4.1.2, the effect of surface conduction at low ion strength conditions may underestimate the value of zeta potential. The method of Briggs [Bri28] was used to determine if surface conduction was effecting the measurement. The excess of the conductance (1/Ω) measured in the capillary (i.e., with the substrate in place) over the conductance of the bulk (i.e., just the electrolyte solution) is called the surface conductance [Woo46]. The experimentally measured conductance of the capillary or streaming cell was never larger than the conductance of the bulk electrolyte indicating that surface conduction is not effecting the experimental measurement of streaming potential.

5.3.4 Adhesion

The negative surface charge of the COM crystal is related to the atomic structure of the (010) and $(10\bar{1})$ crystallographic planes. These two planes make up much of the surface of the COM crystal. Both the (010) and $(10\bar{1})$ crystallographic planes are associated with more $C_2O_4^{2-}$ than Ca^{2+} (Figure 5.4) giving the particles a net negative theoretical surface charge, which corresponds to the experimentally determined zeta potential values. However, the $(10\bar{1})$ face should be more positive than the (010) face because of the larger $Ca^{2+}/C_2O_4^{2-}$ ratio for the former crystallographic face.
The adhesive strength of each of these two surfaces to the negatively charged fused quartz surface are not equivalent. The value of adhesion strength is taken as the value of applied stress at 50% of the initial particles adhering. This method is used to be consistent with previously published adhesion studies on other materials. The strength acting on the (010) surface at 50% adhering is 81 Pa while the strength acting on the $(10\bar{1})$ surface at 50% adhering is 170 Pa, as shown in Figure 5.14. Both atomic surfaces predominately contain oxalate ions; however, the $(10\bar{1})$ surface has a higher $Ca^{2+}/C_2O_4^{2-}$ ratio per unit area than does the (010) crystal plane, making the $(10\bar{1})$ more positive than the (010). Electrostatically, a greater repulsive force should exist between the (010) and fused quartz than between the $(10\bar{1})$ and fused quartz. The greater repulsive force between the (010)

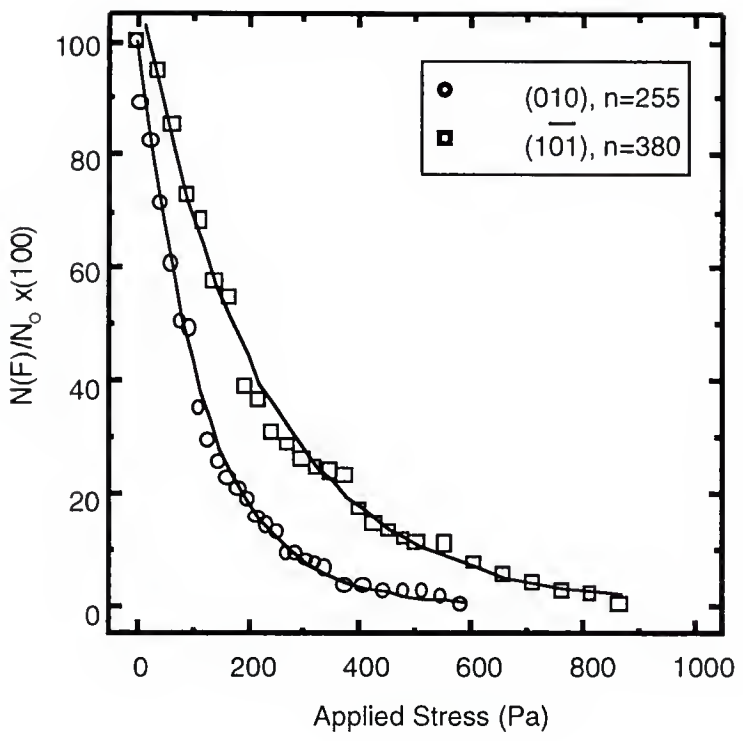

Figure 5.14. The probability of an initial particle on the (010), O, and on the (10$\bar{1}$), □, adhering versus the applied stress acting on the particle at failure as determined using the dynamic wet cell. The total number of particles counted that were lying on the (010) was n=255 and on the (10$\bar{1}$) was n=380.

and the fused quartz will enable the particles lying on the (010) surface to be removed at a lower hydrodynamic shear force than those lying on the $(10\bar{1})$, which is confirmed experimentally. Due to the relative crystallographic dimensions of COM, particles having the $(10\bar{1})$ in contact with the substrate will have a greater displacement force applied at a given flow rate than particles with the (010) in contact with the substrate. Although contact areas of the two crystallographic planes are approximately equal, particles with the $(10\bar{1})$ in contact with the substrate have a higher probability of adhering at a particular flow rate than those in the (010) orientation. This verifies that the $(10\bar{1})$ planes have a specific interaction, probability mediated by the greater incidence of Ca^{2+} in this crystallographic habit interacting with negatively charged sites on the SiO_2 [Ile79].

The curve of the percent of adhered particles vs. the applied stress shown in Figure 5.14 has an interesting shape. Many natural processes exhibit a normal distribution which would give a sigmoidal cumulative normal distribution [Ebd77]. Since the minimum stress that can be measured using the dynamic wet cell and COM particles is approximately 10 Pa, the cumulative normal distribution is truncated at the lower stresses and the sigmoidal shape may not be apparent. For materials having a higher adhesive strength, the cumulative distribution of percent adhering vs. applied stress appear to be sigmoidal in nature.

5.3.5 Theoretical Modeling of Interactions

The adhesion of the two negatively charged surfaces cannot be entirely attributed to electrostatic interactions. Adhesion between glass and COM particles is also due, at least in part, to van der Waals interactions and the force due to gravity. The van der Waals interactions between macroscopic bodies may be described using the Hamaker constant as described by the Tabor-Winterton relationship if both the index of refraction and the dielectric constant of the interacting materials are known [Tab80]. The van der Waals forces were estimated using the Hamaker constants for COM and fused quartz.

The A_{131} value for COM in water is 1.37×10^{-20} J [Chapter 4], while the A_{131} value for fused silica in water is 0.849×10^{-20} J [Hou80]. The Hamaker value for COM-H_2O-Glass was determined using the geometric mean [Isr92],

$$A_{132} \approx \sqrt{A_{131} A_{232}}, \tag{5.8}$$

resulting in a value of A_{132} for the COM-H_2O-fused quartz system of 1.08×10^{-20} J.

The van der Waals interaction energy is given by [Isr92]

$$V_A = -\frac{A_{132}}{12\pi d^2}, \tag{5.9}$$

where V_A is the energy due to van der Waals interactions, A_{132} is the Hamaker constant given above, and d is the separation distance between the interacting materials which is taken as the surface roughness of the two materials..

The average separation distance was estimated from the surface roughness of COM particles and the fused quartz substrates, measured using contact mode SPM in a COM saturated solution environment. The r_a value or mean roughness value of the fused quartz substrate is 0.87 nm over a 5x5 μm^2 area, Figure 5.15. The r_a values for the COM (010), Figure 3.14, and $(10\bar{1})$, Figure 3.15, are 32 nm and 81 nm, respectively, over a scan area of 5x5 μm^2. The high surface roughness of the COM crystal may be due to the growth mechanism of the twinned COM crystal. The crystals may have a growth ledge at the twin boundary where the atoms grow more rapidly on one half of the twin boundary but not on the other causing the roughness to be large across this boundary. However, if a section analysis is performed on the SPM images to determine roughness across the particle surface in an area without a twin boundary, values for roughness between 16 nm and 21 nm are measured.

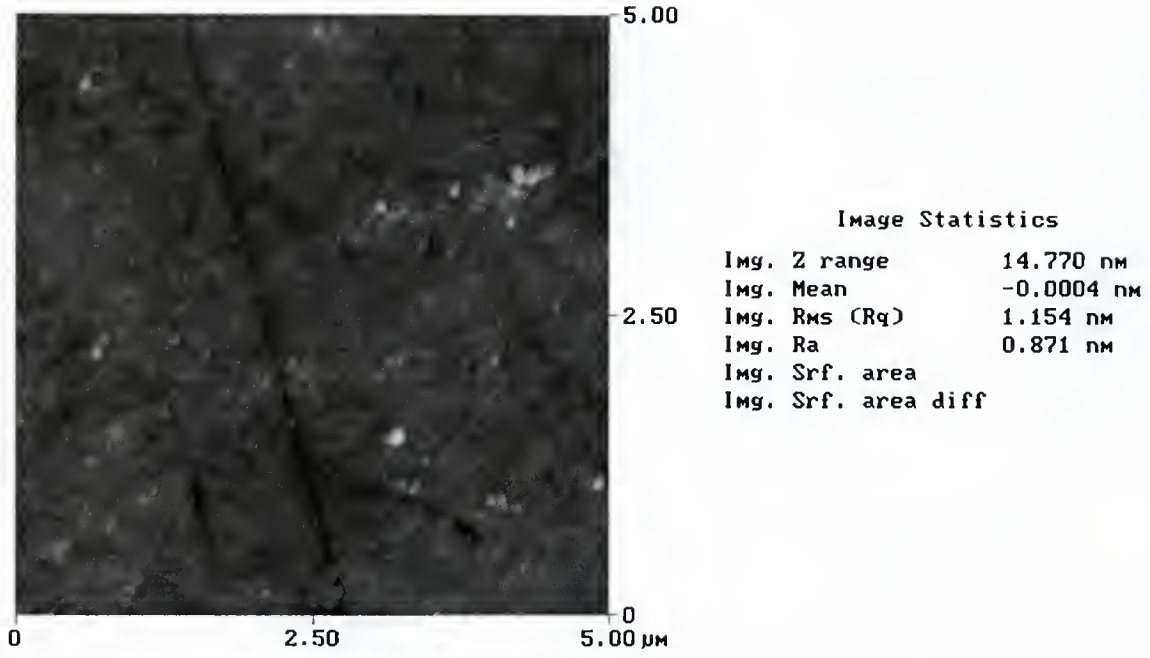

Figure 5.15. A scanning probe microscopy image of the fused quartz surface under a COM saturated solution liquid environment. Also given is the image roughness statistics which include the r_a or mean surface roughness of 0.871 nm.

To model the interactions due to the electrical double layers of the COM particle and fused quartz substrate a simplification of Derjaguin-Landau-Verwey-Overbeek (DLVO) [Der41, Ver48] theory was used. The simplified theory presented by Hogg, Healy, and Fuerstenau (HHF) [Hog66] uses the Debye-Hückel approximation for low surface potential and does not account for dipole and specific chemical interactions. The Debye-Hückel reciprocal length parameter, κ, for small surface potentials is given by [Isr92]

$$\kappa = \sqrt{\sum_i \frac{c_i e^2 z_i^2}{\varepsilon k T}} \tag{5.10}$$

where z is the valence of each ionic species, i, in solution, c is the concentration, ε is the dielectric constant of the suspending medium, e is the charge on a electron, k is Boltzmann's constant, and T is the absolute temperature.

Hogg et al. [Hog66] give the potential energy, V_R, between interacting flat double layers to be equal to the change in free energy of the double layer system when the plates are brought together from infinity. Thus,

$$V_R = \Delta G = G_{2d} - G_\infty \tag{5.11}$$

where G_{2d} is the free energy of the double layer system when the plates are separated by a distance $2d$ and G_∞ is the free energy of the double layer system when the plates are separated by a distance of infinity. The components of the total energy due to the interacting double layers are given as [Hog66]

$$G_{2d} = \frac{\varepsilon\kappa}{8\pi}\left[2\psi_{0_1}\psi_{0_2}\operatorname{csc}h 2\kappa d - \left(\psi_{0_1}^2 + \psi_{0_2}^2\right)\coth 2\kappa d\right] \tag{5.12}$$

and

$$G_{\infty} = -\frac{\varepsilon\kappa}{8\pi}\left(\psi_{0_1}^2 + \psi_{0_2}^2\right) \tag{5.13}$$

where ψ_{0_1} and ψ_{0_2} can be taken as the values of zeta potential for COM and fused quartz, respectively. Substituting for the free energy terms in eq. (5.11),

$$V_R = \frac{\varepsilon\kappa}{8\pi}\left[\left(\psi_{0_1}^2 + \psi_{0_2}^2\right)(1 - \coth 2\kappa d) + 2\psi_{0_1}\psi_{0_2}\,\mathrm{csc}\,h2\kappa d\right], \tag{5.14}$$

Equation (5.14) describes the potential energy of two interacting infinite, parallel, flat double layers as a function of the surface potential of each plate and the separation distance between the two plates.

The total interaction between COM and the substrate is given by

$$V_T = V_A + V_R, \tag{5.15}$$

where V_T is the total interaction potential, V_A is the potential due to van der Waals forces, and V_R is the potential due to the interacting electrical double layers.

The van der Waals potential, V_A, for the (010) crystallographic face of COM interacting with fused silica across water at a separation of 32 nm is thus $-30\text{x}10^{-8}$ J/m^2 calculated using eq. (5.11). The potential due to the interaction of the electrical double layers, V_R, at the same distance of separation, 32 nm, is $1058\text{x}10^{-10}$ J/m^2 calculated using eq. (5.14). Using eq. (5.15), the total interaction potential was calculated to be $-1919\text{x}10^{-10}$ J/m^2, which corresponds to an adhesive strength or adhesive pressure of 29 Pa. The theoretical adhesive strengths were determined by a simple differentiation of eq. (5.9) and eq. (5.14) with respect to separation distance. Similar calculations for the $(10\bar{1})$ face of COM interacting with fused silica across water were performed using the surface roughness as the separation distance and yielded a V_A=$-426\text{x}10^{-10}$ J/m^2, V_R=$6\text{x}10^{-10}$ J/m^2,

and V_T=-419x10^{-10} J/m^2. The theoretical total adhesive pressure for $(10\bar{1})$ COM interacting with fused silica is 1 Pa. The theoretical values of 29 Pa and 1 Pa are much lower than the experimentally measured adhesion values of 81 Pa and 170 Pa for the interaction of fused quartz with the (010) and $(10\bar{1})$ COM faces, respectively. If the separation distance used in the theoretical calculation is 20 nm, the value of adhesion strength is 98 Pa, which compares favorably with experimental results. Krupp [Kru67] determined that the adhesive strength or adhesive pressure for various interacting materials is between (2-30)x10^7 Pa for a separation of 0.4 nm. Israelachvili [Isr92] has shown comparable results for similar separation distances. However for separation distances on the order of 20 nm the adhesive stress values are considerably lower [Isr92] and comparable to the values of adhesive strength determined herein.

Gravitational forces were also calculated to determine their contribution to COM crystal adhesion using the average COM particle size and a particle density of, 2.2 g/cm^3, resulting in a strength equal to 1.2 Pa. This represents the force due to gravity of 1.1x10^{-10} N acting on one particle of mean particle size divided by the average area ~111 μm^2 of the (010) and $(10\bar{1})$ particle faces. Thus gravitational effects are insignificant when compared to the effects due to van der Waals and electrostatic interactions.

5.4 Conclusions

A device was designed and built and the methodology devoloped to measure the adhesion strength between a particle and substrate. A second device was designed and built and the methodology developed to measure the zeta potential on a flat substrate. The parallel plate adhesion technique is a suitable method for determining the adhesive strength between a particle and a substrate in a dynamic liquid environment. The van der Waals interactions were estimated and related to the adhesion between COM crystals and a fused quartz substrate. Correlations were made between the theoretical atomic surface structure of COM and the crystallographic dependence on adhesive strength. Theoretical

electrostatic considerations were invoked and are used to explain the crystallographic dependence. The application of this adhesion measuring technique to the study of kidney stone disease seems to be promising in that the importance of specific biological materials can be ranked with respect to their adhesive properties to COM crystals. Which, in turn, may allow researchers to focus on materials that have the greatest adhesion to COM.

CHAPTER 6
MEASUREMENT OF COM ADHESION TO MACROMOLECULAR SUBSTRATES

6.1 Introduction

Kidney stone disease has been described as an opportunistic disease which can rely on many causative mechanisms acting in concert [Fin78a, Fin84]. One of the possible mechanisms is the growth of an adherent particle, called a fixed particle, in the lumen of a nephron. Such an adherent particle can subsequently grow by secondary nucleation and growth and/or aggregation of crystallites to a size large enough to occlude a renal tubule, which is the basis of the fixed stone mechanism of kidney stone development. Finlayson and Reid [Fin78b] calculated the time for a COM crystal to grow to a large enough size to cause an occlusion and determined that the crystal would not have enough time to grow to such a size. Therefore, crystal attachment is a necessary process in kidney stone formation [Man91, Man94].

Riese, Mandel, and coworkers [Man94, Rie92, Rie88] have shown *in vitro* attachment of COM crystals to inner medullary collecting duct epithelial cells of the rat animal model in the static case (i.e., without the presence of flow). They also proposed that perturbations in the cell membrane structure with a loss in membrane polarity can enhance crystal attachment [Rie92]. *In vivo* crystal attachment to epithelial cells in the rat animal has been demonstrated by Khan et al. [Kha82]. Renal injury has also been implicated in fixed stone formation [Man91, Gil79, Kha84]. Khan [Kha82, Kha95b] has discussed that after attachment of a crystal to the epithelial cell surface that injury to the cell may occur but is not necessary to occur.

A few different results may ensue due to crystal attachment to the epithelial cell. The cell may die and be washed away in the urine flow taking with it the crystal. The cell may envelope the crystal and continue to function normally [Lie92, Lie93, Lie94] with no further growth of the crystal. However, if epithelial cell injury has occurred, basement membrane proteins may be accessible to adhere to COM crystals by sloughing of the cells leaving behind the exposed underlying architecture, the basement membrane. The basement membrane is a layer of proteins which underlies the epithelial sheet and will be discussed subsequently in more detail.

Depending on the extent of injury, other proteins common to the extracellular matrix found below the basement membrane may also be accessible for attachment to COM crystals. Khan et al. [Kha84] demonstrated the association of crystals to fibrillar macromolecular structures by scanning electron microscopy (SEM). Khan has also shown crystals passing through the basement membrane into the extracellular space near the papillary tip [Kha95b].

Researchers have shown the attachment of COM crystals to epithelial cells and fibrous proteins characteristic of those found in the basement membrane and extracellular matrix, yet the importance of these individual materials in kidney stone formation with respect to COM crystal adhesion is not known. The necessity to determine the important materials most responsible for COM crystal adhesion will allow researchers to focus their interests to those more important materials in the search for a possible cause and therefore relief from kidney stone formation.

In the current study, both structural extracellular matrix (ECM) proteins, collagen type I, and collagen type IV, and adhesive extracellular matrix glycoproteins, fibronectin and laminin, were examined. A positively charged, synthetic polymer, PEI was also investigated.

The collagen types of molecules are the most abundant of the ECM proteins. Type I is fibrillar in nature and can be found in a number of physiological sites These and

other types of collagen molecules may assemble into collagen fibrils which create mechanical stability for the skin, tendon, bone, and internal organs [Küh87a]. Collagen type IV is a nonfibril forming molecule which creates mechanical stability for the basement membrane and overlying cell architecture [Küh87b]. Laminin and fibronectin are two glycoproteins found in the basement membrane underlying the epithelial sheet. These two proteins aid in the mediation of cell attachment to the extracellular matrix [Alb89]. The collagen molecules, fibronectin, and laminin are not normally accessible to COM crystals in the urine unless injury to the renal epithelial wall has occurred.

In the current study, the adhesion of COM particles to different macromolecules was measured using a variation of the technique reported by Pelton et al. [Pel82, Pel84] to measure the adhesion between polystyrene spheres and a Pyrex substrate. A similar device was developed by Hochmuth et al. [Hoc73] and has been used extensively to study the adhesion of cellular material to surfaces [Dor77, For84, Moh74, Tru90, van92]. Details pertaining to the specific adhesion apparatus are described in Chapter 5 and will only be briefly be described herein. The apparatus consists of an adhesion chamber which incorporates two fused quartz slides separated by a teflon spacer. The eluent flows through the adhesion cell at a specified rate calibrated against the pump drive. The eluent is forced through the adhesion chamber using a variable speed pump drive connected to a gear pump. A camera mounted above the adhesion cell, which is connected to a monitor and video cassette recorder, records activity in the cell during an experiment.

The method utilizes the volumetric flow rate, adhesion cell and particle dimensions in Poiseuille's equation, to calculate the linear velocity at one particle radius from the cell wall such that,

$$v = \frac{2Q\left(R^2 - r^2\right)}{\pi R^4} \tag{6.1}$$

where v is the linear velocity and Q is the volumetric flow rate. Half the distance between the fused quartz slides is R and the particle radius is r. The corresponding displacement force acting at one particle radius, F_d, is calculated using the fluid properties, particle dimensions, and the calculated linear velocity from equation (6.1) such that [Gol67],

$$F_d = 1.7(6\pi\eta r v) \tag{6.2}$$

where η is the eluent viscosity, r the particle radius, and v the linear velocity.

6.2 Materials and Methods

6.2.1 Particle Synthesis and Characterization

COM particles were produced and characterized as described in Chapter 3.

6.2.2 Substrate Coating

Optical grade fused silica slides (spectroscopic grade, ESCO Products, Oak Ridge, NJ) were coated with a variety of macromolecules: polyethyleneimine (PEI) (Eastman Kodak Co., Rochester, NY), collagen type I (C7661, Sigma Chemical Co., St. Louis, MO), fibronectin (F1141, Sigma Chemical Co., St. Louis, MO), and MATRIGEL® Basement Membrane Matrix (40234C, Collaborative Biomedical Products, Bedford, MA). MATRIGEL® Basement Membrane Matrix consists of laminin, collagen type IV, heparan sulfate proteoglycans, entactin, and nidogen listed in descending order of quantity [Kle82]. Each slide was coated with the desired macromolecule to be used as the substrate on which the adhesion strength to COM would be determined. The procedures employed for coating the glass with all of the macromolecules, with the exception of PEI, are available from the protein suppliers.

The collagen I used was from rat tail and was in solid form from the vendor. A stock solution of 1 mg of solid collagen type I was dissolved in 1 ml of 0.1 M acetic acid ($HC_2H_3O_2$). The stock solution was further diluted to make a working solution to coat at a coverage of 10 $\mu g/cm^2$. The dilution occurred by adding 645.16 µl of the stock solution to 9.355 ml of 0.1 M acetic acid. Each 2.54 cm x 2.54 cm fused quartz slide was covered by 1 ml of the collagen type I working solution. The slide was stored 24 hr at 4°C with the protein solution on it. After the 24 hr, the remaining solution was aspirated or removed by suction. The slides then dried for 24 hr at 4°C before being used in adhesion experiments.

The fibronectin was 0.1% solution (1 mg protein/ml in 0.5 M NaCl, 0.05 M Tris buffer at pH 7.5) from bovine plasma. A working solution was prepared from the above solution by adding 32.08 µl of the fibronectin stock solution to 967.9 µl of Hank's Balanced Salt Solution (14175-095, Gibco BRL, Gaithersburg, MD). Each 2.54 cm x 2.54 cm fused quartz slide was covered by 2 ml of the fibronectin working solution to make the protein coverage on each slide 10 $\mu g/cm^2$. The slides sat for 1 hr under the protein solution, the remaining solution was aspirated and the slides were stored at 4°C until used.

The material MATRIGEL® Basement Membrane Matrix is a solubilized basement membrane extracted from the Engelbreth-Holm-Swarm mouse sarcoma or tumor. The protein mixture arrives as a stock solution at a concentration of 13.8 mg protein/ml. The protein mixture must remain frozen until use. The MATRIGEL® Basement Membrane Matrix was thawed at 4°C overnight. All the slides and pipettes were precooled because the MATRIGEL® Basement Membrane Matrix will gel rapidly and irreversibly at 22°C to 35°C. A 1:10 dilution of the stock protein was prepared using serum-free medium (11039-021, Dulbecco Modified Eagle Medium: Nutrient Mixture F12, Gibco BRL, Gaithersburg, MD) to make a working solution having a concentration of 1.35 mg/ml.

The fused quartz slides were coated with 1 ml of the working solution to give a coverage of 200 $\mu g/cm^2$.

To coat the glass with PEI, a 2 weight percent suspension of PEI was prepared. The glass surfaces were prepared for coating by soaking in acetone and isopropanol for 3 min., respectively. The slides were then liberally washed with deionized water. The slides were soaked and agitated in a 2 w/o suspension of PEI for 2 min. and turned over and soaked for an additional 2 min. Finally, the slides were again liberally washed with deionized water and allowed to dry.

To verify that the proteins were being retained on the fused quartz surface, attenuated total reflection (ATR) fourier transform infrared spectroscopy (FTIR) (20SXB FT-IR Spectrometer, Nicolet Instrument Co., Madison, WI) was performed on select substrates coated using the previously described procedures. A 45° thallium bromide-thallium iodide (KRS-5) crystal having an index of refraction of 2.35 was used to couple the infrared radiation to achieve internal reflection.

6.2.3 Adhesion Measurements

Adhesion measurements were performed on all the macromolecular substrates (i.e., collagen type I, fibronectin, MATRIGEL® Basement Membrane Matrix, and polyethyleneimine) as described in Chapter 5.2.1. The measurements were performed in a low ionic strength environment, COM saturated solution, and a high ionic strength environment, artificial urine ion solution (AUIS). The ionic strengths of COM saturated solution and AUIS are $5x10^{-6}$ M and 0.323 M, respectively. The pH of COM saturated solution is 5.7 while that of AUIS is 6.0. Analysis of the experimental data was performed in the same manner as the data in Chapter 5. The data was plotted as applied stress vs. $(N(F)/N_o)x100$, where N_o is the original number of particles adhering at no applied stress and N(F) is the number of particles adhering at each applied stress. A curve was fit to the experimental data using SigmaPlot® Software (Version 5.0, Jandel

Corporation, San Rafael, CA). The nonlinear regression was of the form $y = a\exp(-bx)$, where a and b were variables to be solved for. After determining the values of a and b, the value of applied stress was calculated at y=50 and was used for the mean applied stress value.

6.2.4 Streaming Potential Measurements

Streaming potential measurements were performed on all the macromolecule coated substrates (i.e., collagen type I, fibronectin, MATRIGEL® Basement Membrane Matrix, and polyethyleneimine) using the instrument and the procedure described in Chapter 5.2.2. The measurements were performed in two different electrolyte solutions, COM saturated solution and AUIS.

6.3 Results and Discussion

6.3.1 Substrate Coverage

Attenuated total reflection FTIR showed that after the fused quartz slides were coated with the macromolecules that the macromolecules were retained. Figure 6.1 is a plot of wavenumber vs. percent absorbance for all of the substrates. The peaks below 1200 cm^{-1} are from the absorption of the fused quartz substrate (i.e., Si-O-Si vibrations). At lower wavenumbers (higher wavelengths) sampling depth increases as seen in Figure 2.18. Since the majority of material being sampled is fused quartz, the majority of the absorbance will be due to the fused quartz.

Figures 6.2 is the same data shown in Figure 6.1; however, Figure 6.2 shows a much smaller range in wavenumber. Figure 6.2 focuses on higher wavenumbers, 2100-3600 cm^{-1}. In this range, the fused quartz gives no distinct absorbance peaks. However, the macromolecular substrates do exhibit absorbance peaks between 2800-3000 cm^{-1} due to C-H stretch or N-H stretch. Because the macromolecular substrates exhibit absorbance

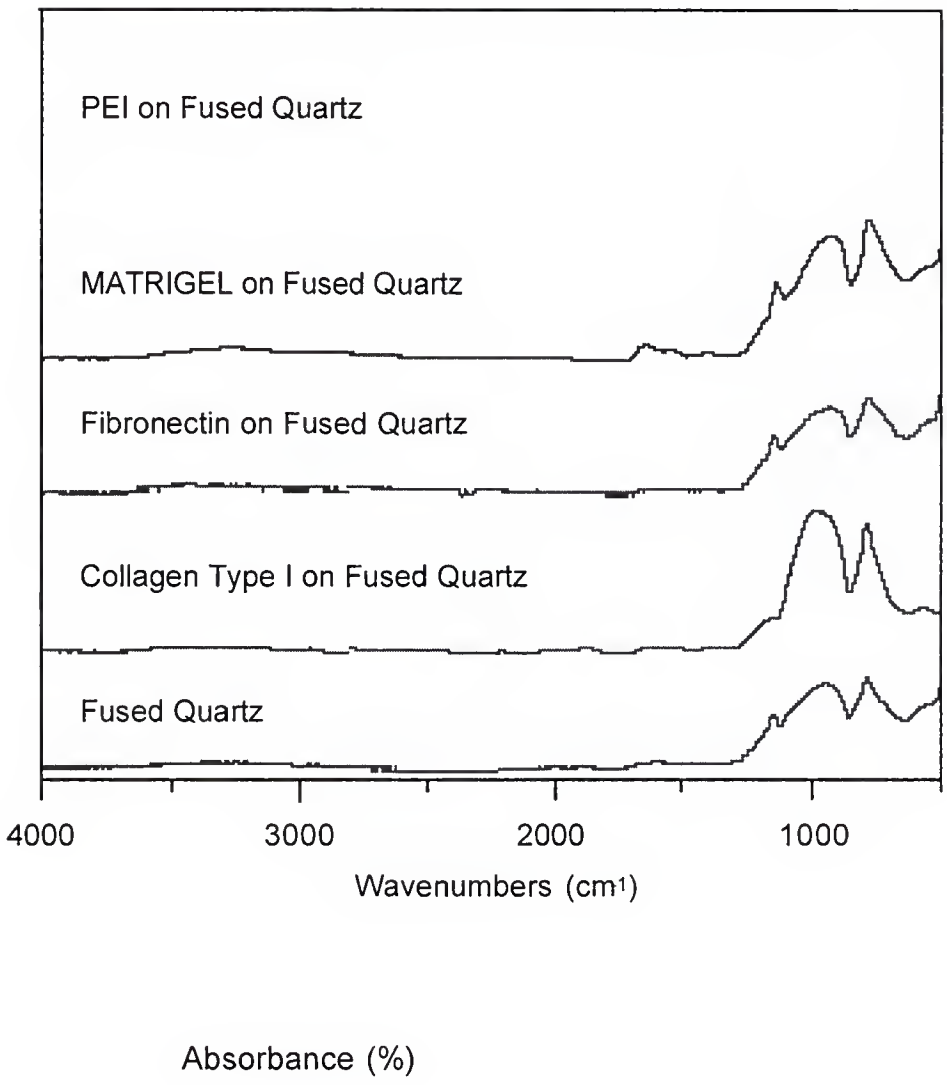

Figure 6.1. A plot of wavenumber vs. absorbance for fused quartz, collagen type I, fibronectin, MATRIGEL®, and PEI produced using ATR-FTIR. All of the macromolecular substrates were coated on fused quartz.

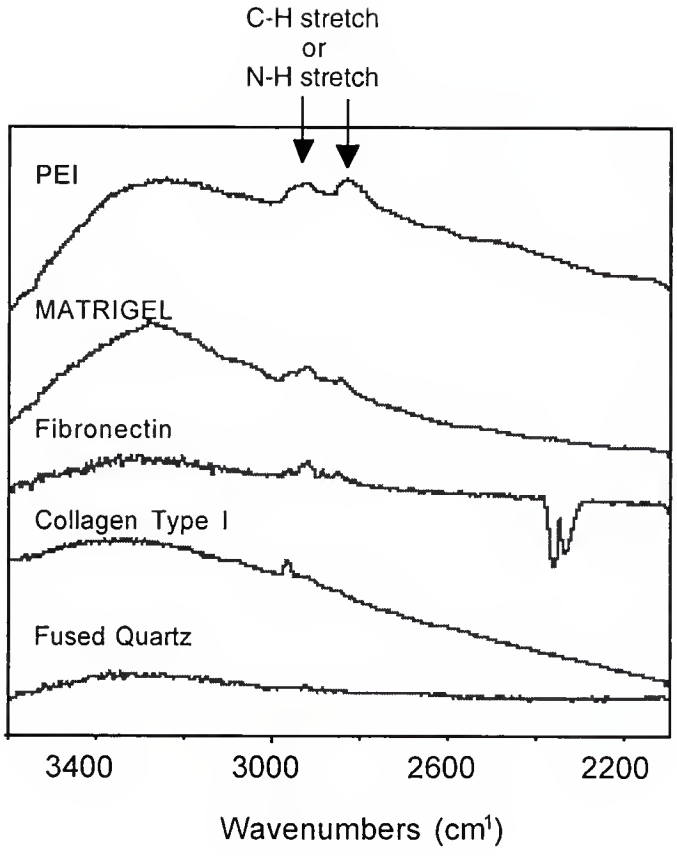

Figure 6.2. A plot of wavenumber vs. absorbance for fused quartz, collagen type I, fibronectin, MATRIGEL®, and PEI produced using ATR-FTIR for the wavenumbers 2100-3600 cm^{-1}. All of the macromolecular substrates were coated on fused quartz.

peaks not found in the FTIR spectra of fused quartz alone, the conclusion that the coating procedure is applicable and that the macromolecules are retained on the fused quartz even after five days at 4°C is made.

6.3.2 Zeta Potential Determinations

The experimental zeta potential of COM particles at pH 6 in saturated COM solution and 10% AUIS at 37°C is -32 mV and -21 mV, respectively, Figure 6.3. Under the solution conditions of saturated COM at a pH of 5.7, the zeta potentials of the different macromolecular substrates varied over a range of values as shown in Table 6.1. The values of zeta potential shown in Table 6.1 are the mean and 95% confidence interval for at least three separate experiments on the same substrate. Collagen type I, fibronectin, and MATRIGEL® had negative zeta potential values. Figure 6.4 shows driving pressure vs. streaming potential for collagen type I, fibronectin, MATRIGEL®, and PEI. The scatter in the data shown in Figure 6.4 for PEI may be due to the fact that the streaming potential for this substrate was measured over a period of 3 days. The equilibrium surface structure may age with time depending on solution conditions, subsequently effecting the zeta potential.

Zeta potential determination of the macromolecular substrates in AUIS was attempted using the streaming potential technique. The values of streaming potential in the high ionic strength, complex ion solution were on the order of 1-2 mV at the highest driving pressures and undetectable at lower driving pressures. The asymmetry potentials were also about 1-2 mV. Because the potentials we were trying to measure (i.e., streaming) and the potentials we were trying to negate (i.e., asymmetry) were approximately the same, valid determinations of the actual streaming potentials could not be made, even using the Horn and Onoda [Hor77] circuit.

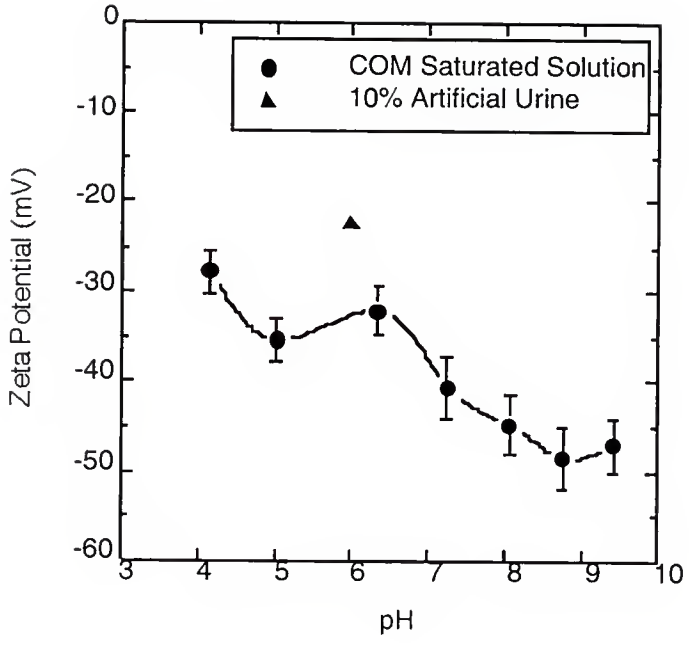

Figure 6.3. Zeta potential as a function of pH for COM in saturated COM solution and zeta potential at a pH of 6 for COM in 10% AUIS.

Table 6.1 The values of zeta potential of the macromolecular substrates determined using streaming potential measurements in saturated COM solution.

Macromolecular Substrate	Zeta Potential (mV)	
	Mean	Standard Deviation
Collagen type I	-9.6	0.3
Fibronectin	-12.8	2.5
MATRIGEL®	-10.9	1.4
Polyethyleneimine	7.8	0.4

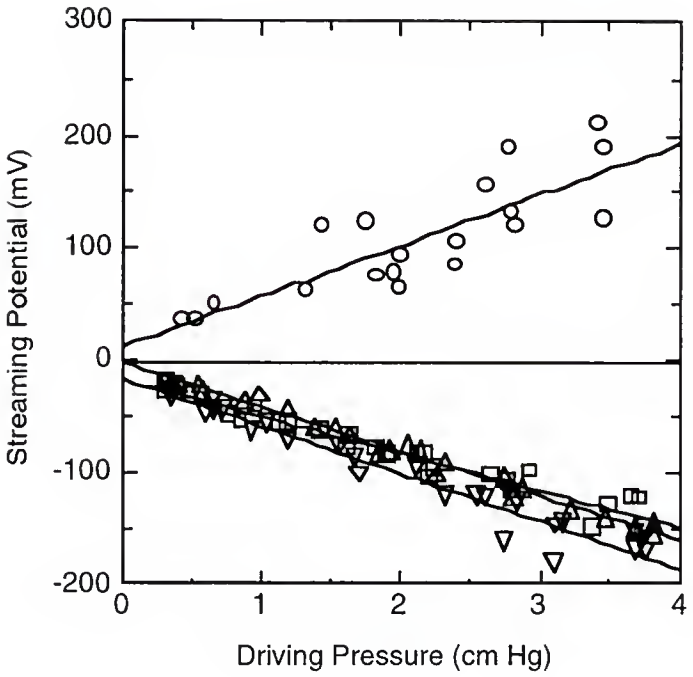

Figure 6.4. A plot of driving pressure vs. streaming potential for the substrates collagen type I (Δ), fibronectin (∇), MATRIGEL® (□), and PEI (○).

6.3.3 Adhesion Measurements

The measurement of adhesion of COM particles to the fused quartz and macromolecular substrates generated the curves labeled Figure 6.5 to Figure 6.11. The plots of adhesion of COM particles to the MATRIGEL® and PEI substrates in AUIS are not included because no decrease in the number of particles as the applied stress increased was observed. In fact, an increase in the number of particles adhering was observed throughout the experiments, indicating an adhesive strength well above that measurable with the current instrument between particle and substrate in AUIS.

The adhesion between glass and COM crystals was demonstrated in Chapter 5 and a COM crystallographic dependence on adhesion to glass was observed. In much of the results involving macromolecular substrates and COM saturated solution, the same correlation between COM crystallographic habit and adhesive stress was observed, as shown in Figure 6.12. In every case, a COM particle lying on the $(10\bar{1})$ will have a higher adhesive stress than will a COM particle lying on the (010) when in contact with a negatively charged substrate, with the exception of the fibronectin substrate. The fibronectin substrate had a slightly lower adhesive strength to the $(10\bar{1})$ than to the (010), ~35 Pa. Such trends can be explained in terms of electrostatic interactions. The negatively charged proteins exhibit a greater repulsive force against the more highly negative 010 planes than the less negative $10\bar{1}$ planes of the COM crystal resulting in a lower adhesive stress to the COM (010) versus the COM $(10\bar{1})$ due to electrostatic interactions. The COM crystals obtained the highest adhesive stress to the positively charged macromolecule, PEI. The opposite crystallographic orientation effect of COM was observed on the adhesive stress to PEI. The more negatively charged (010) crystal plane had a larger adhesive strength to the positively charged PEI than did the less

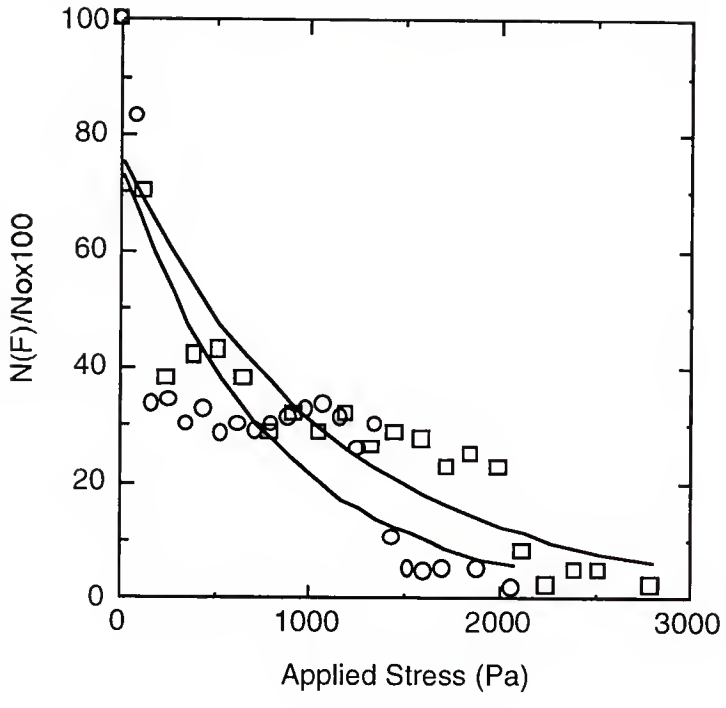

Figure 6.5. The probability of an initial COM particle on the (010), ○, and the $(10\bar{1})$, □, adhering to fused quartz in AUIS versus the applied stress acting on a particle at failure as determined using the dynamic wet cell. The total number of particles counted lying on the (010) was n=113 and on the $(10\bar{1})$ was n=84.

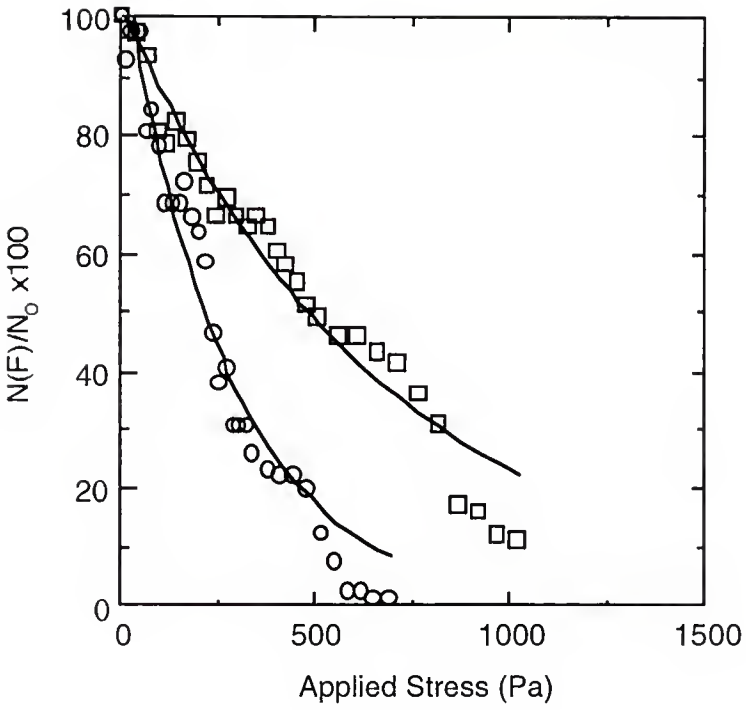

Figure 6.6. The probability of an initial COM particle on the (010), ○, and the $(10\bar{1})$, □, adhering to collagen type I in COM saturated solution versus the applied stress acting on a particle at failure as determined using the dynamic wet cell. The total number of particles counted lying on the (010) was n=82 and on the $(10\bar{1})$ was n=133.

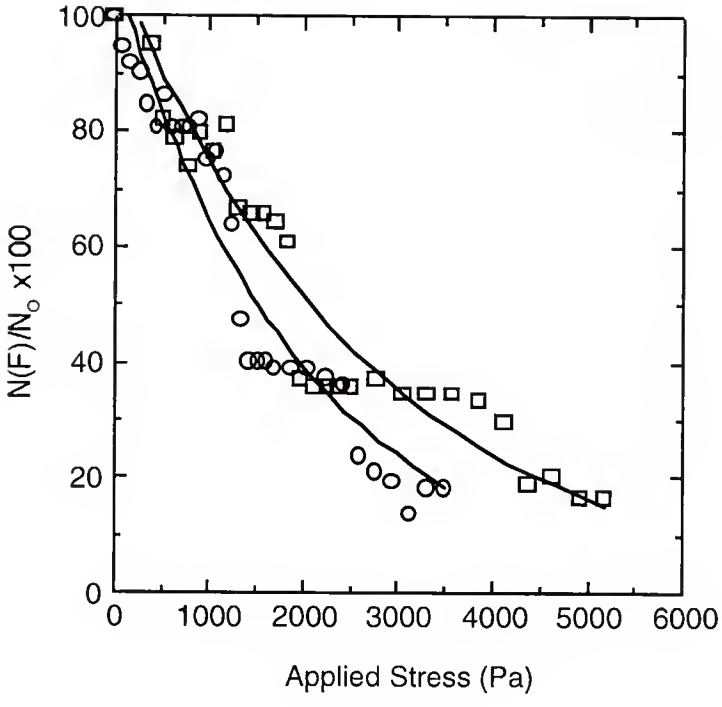

Figure 6.7. The probability of an initial COM particle on the (010), ○, and the $(10\bar{1})$, □, adhering to collagen type I in AUIS versus the applied stress acting on a particle at failure as determined using the dynamic wet cell. The total number of particles counted lying on the (010) was n=84 and on the $(10\bar{1})$ was n=72.

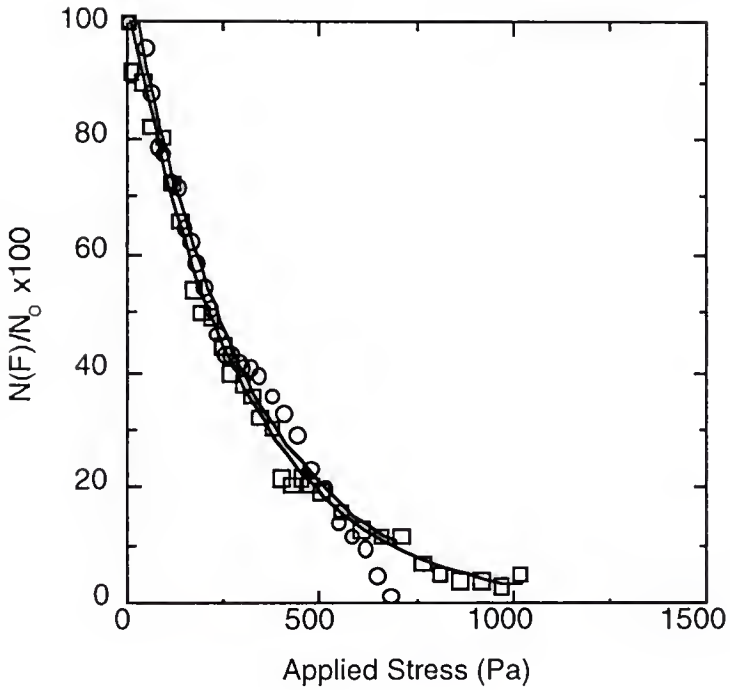

Figure 6.8. The probability of an initial COM particle on the (010), O, and the $(10\bar{1})$, □, adhering to fibronectin in COM saturated solution versus the applied stress acting on a particle at failure as determined using the dynamic wet cell. The total number of particles counted lying on the (010) was n=87 and on the $(10\bar{1})$ was n=104.

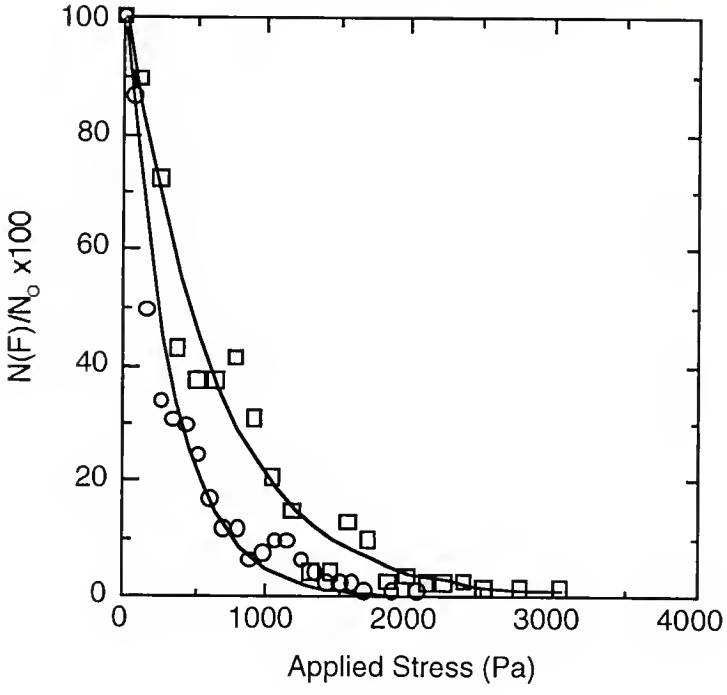

Figure 6.9. The probability of an initial COM particle on the (010), O, and the ($10\bar{1}$), □, adhering to fibronectin in AUIS versus the applied stress acting on a particle at failure as determined using the dynamic wet cell. The total number of particles counted lying on the (010) was n=95 and on the ($10\bar{1}$) was n=143.

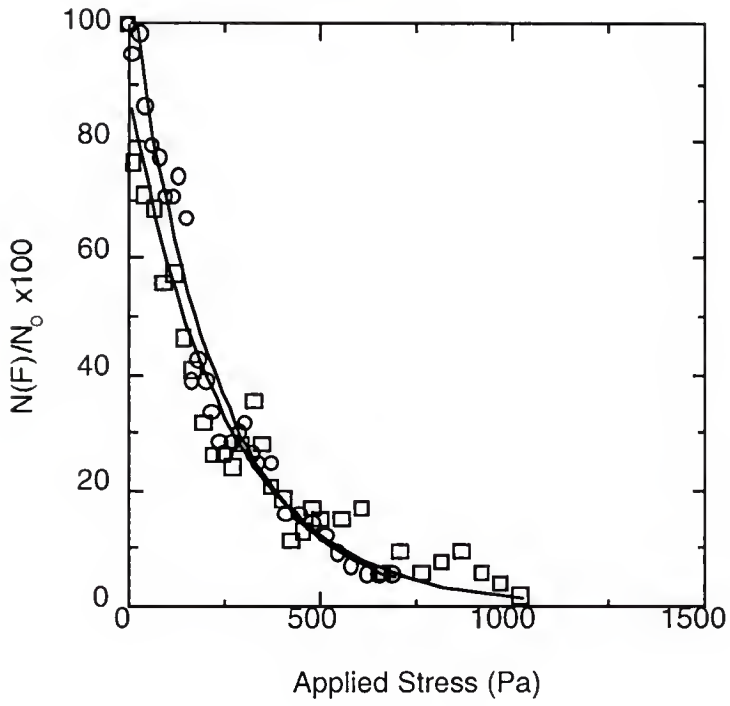

Figure 6.10. The probability of an initial COM particle on the (010), O, and the ($10\bar{1}$), □, adhering to MATRIGEL® in COM saturated solution versus the applied stress acting on a particle at failure as determined using the dynamic wet cell. The total number of particles counted lying on the (010) was n=57 and on the ($10\bar{1}$) was n=54.

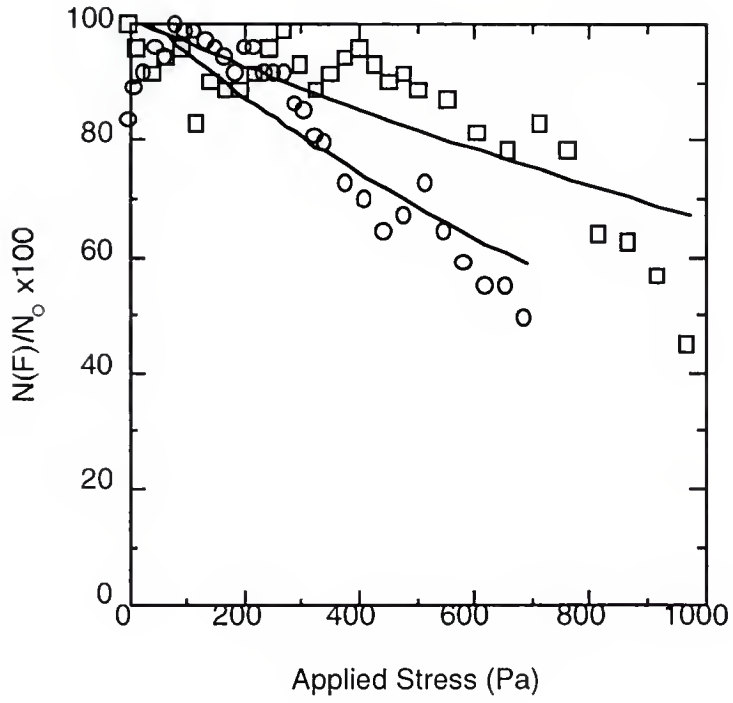

Figure 6.11. The probability of an initial COM particle on the (010), ○, and the ($10\bar{1}$), □, adhering to PEI in COM saturated solution versus the applied stress acting on a particle at failure as determined using the dynamic wet cell. The total number of particles counted lying on the (010) was n=61 and on the ($10\bar{1}$) was n=69.

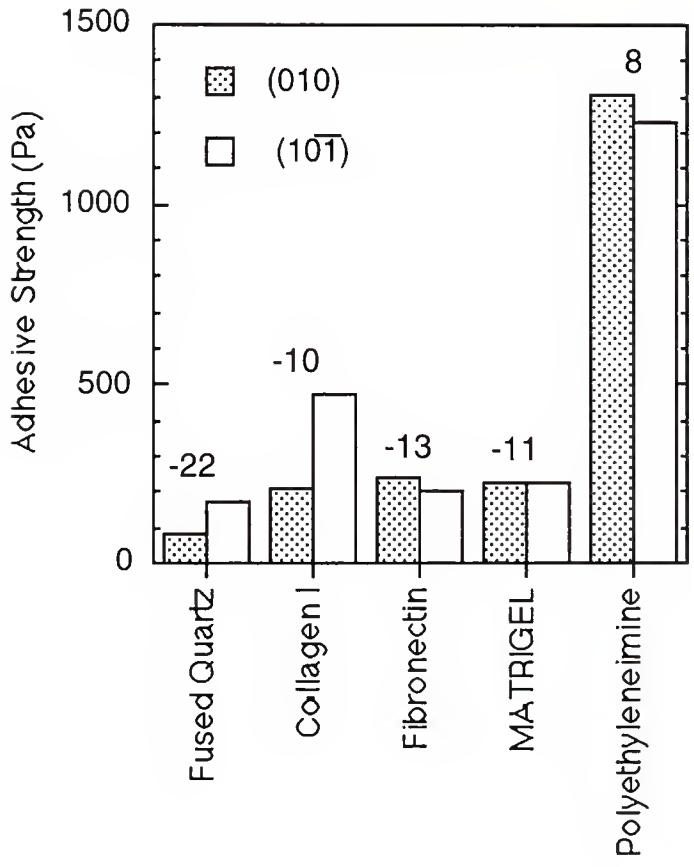

Figure 6.12. A bar chart summarizing the adhesion data experimentally determined in COM saturated solution (i.e., low ionic strength). The numbers above each set of bars is the value of the zeta potential for each substrate.

negatively charged ($10\bar{1}$) of the COM crystal. Although crystallographic orientation did not always effect the adhesive strength (e.g., fibronectin); experimentally determined adhesion results suggest that electrostatic interactions play a large role in COM adhesion at low ionic strength.

Under high ionic strength conditions the adhesion of COM particles to the macromolecular substrates was higher than adhesion of COM to the same macromolecules under low ionic strength conditions, with the exception of the (010) crystal face of COM in contact with fibronectin, as shown in Figure 6.13. The increase may be due to the collapse of the ionic double layer surrounding both the particle and substrate. The double layer collapse leads to reduced electrostatic repulsion, therefore allowing for shorter separation distances between the particle and the substrate where van der Waals attractive forces will be stronger.

Because the ionic strength of the AUIS is so high, the solution will not be able to support charge and the effect of electrostatic interactions will be negligible. Calculations performed using the HHF theory for heterocoagulation, as discussed in Chapter 5, for the materials COM and fused quartz in AUIS determined that a separation distance of less than 10 nm was necessary to produce adhesive pressures on the order of 5000 Pa. The two materials cannot come into such close proximity because the minimum surface roughness of COM is approximately 20-30 nm. When the fused quartz is coated with a macromolecule, the van der Waals forces decrease due to the lower Hamaker constant of the macromolecules therefore limiting the total van der Waals pressure to below 5000 Pa. However, a macromolecule has the ability to rearrange itself to optimize its orientation and lower its free energy. Reorientation of the macromolecule may bring it into much closer proximity to the COM crystal allowing very short range interactions to transpire. Because both MATRIGEL® and PEI had adhesive strengths above 5000 Pa (i.e., off the scale), and electrostatic and van der Waals forces cannot account for the high adhesion, some other specific adhesion mechanism must be occurring such as covalent bonding

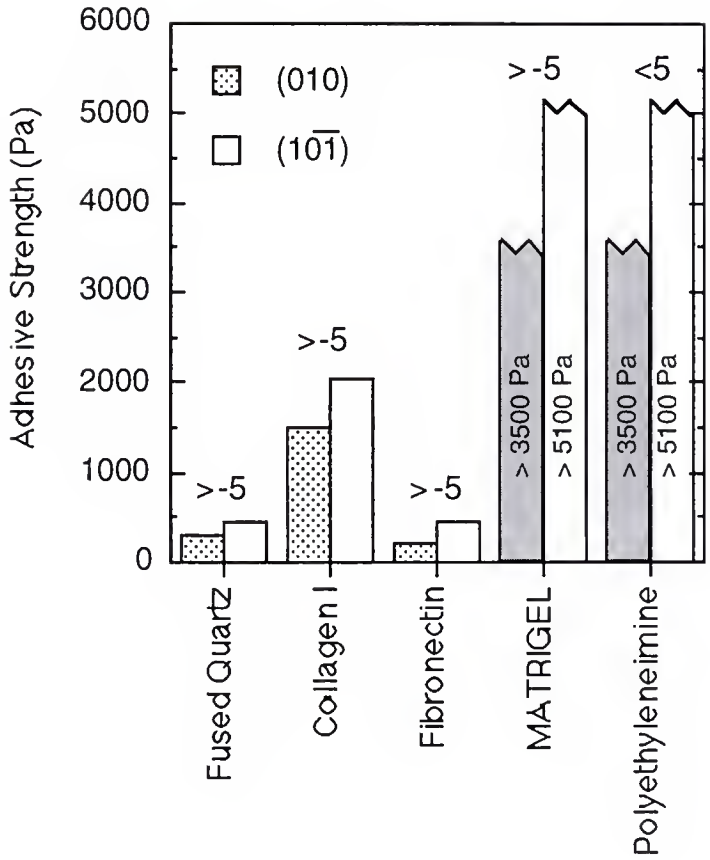

Figure 6.13. A bar chart summarizing the adhesion data experimentally determined in COM saturated solution (i.e., low ionic strength). The numbers above each set of bars is the value of the zeta potential for each substrate.

between the N atoms in the PEI and MATRIGEL® and the Ca atoms in the COM crystal.

As shown in Table 6.2, generally at low ionic strength the adhesive strength between COM and substrates qualitatively depends on the difference in polarity and the magnitude of the difference in zeta potential values of the two adhering materials. That is, the adhesive strength of negatively charged COM particles to a particular macromolecule is larger if the zeta potential of that macromolecule is positively charged and lower if the macromolecule is negatively charged. However, a negatively charged protein substrate has not produced an adhesive strength equal to zero, indicating that forces other than purely electrostatic interactions are present. For proteins, this may be due to conformational changes of the protein on the glass surface under slight variations in solution conditions. Many of the proteins have both positive and negative sites due to the amino and carboxyl groups along the chain length. If a positive area of the protein is extended into the solution, electrostatic attraction will occur to a negative rich area on the COM crystal and vice-versa, increasing the adhesive force. Another explanation may be the fact that the proteins are not a hard surface but a pliable surface capable to some extent of accommodating the crystal, possibly allowing for optimum electrostatic interaction [Big96].

At high ionic strength, another mechanism of adhesion is occurring. The values of adhesion strength are given in Table 6.3. The adhesion values of ~3500 and ~5100 Pa listed are the maximum adhesive strengths measurable for the (010) and ($10\bar{1}$) faces, respectively. At lower values of adhesion, van der Waals forces are dominant; however, at the higher adhesion values, specific bonding interactions are occurring. Trommler et al. [Tro85] measured the adhesion between glass and red blood cells and concluded that molecular contacts must be made between the two negatively charged surfaces for adhesion to occur.

Table 6.2 Values of adhesion strength for COM particles adhering to macromolecular substrates as a function of crystallographic habit plane in COM saturated solution.

Substrate Material	Zeta Potential (mV)	Adhesion Strength (Pa)	
		(010)	$(10\bar{1})$
Fused Quartz	-22	81	170
Collagen type I	-9.6	208	475
Fibronectin	-12.8	238	203
MATRIGEL®	-10.9	222	225
Polyethyleneimine	7.8	1305	1230

6.3 Values of adhesion strength for COM particles adhering to macromolecular substrates as a function of crystallographic habit plane in AUIS.

Substrate Material	Zeta Potential (mV)	Adhesion Strength (Pa)	
		(010)	$(10\bar{1})$
Fused Quartz	> -5	304	457
Collagen type I	> -5	1497	2047
Fibronectin	> -5	220	441
MATRIGEL®	> -5	> 3500	> 5100
Polyethyleneimine	< 5	> 3500	> 5100

In both solution conditions some amount of mechanical bonding will also be occurring due to the pliable nature of the macromolecular surfaces. Further experimental study in the area of COM crystal adhesion to protein substrates is needed to fully understand the mechanism(s) of attachment.

SEM photomicrographs showed that in a few instances, the COM particles were coated with a macromolecular layer after adhesion experiments, Figure 6.14(A). In other samples, the macromolecular coating was not observed, yet adhesion took place as shown in Figure 6.14(B). The differences in coating may be due to the solubility of the protein in COM saturated solution at pH=5.7 and/or the position of the particle in the adhesion cell. If the particle is lying toward the center or beyond the first few millimeters of the entrance of the dynamic wet cell, the flow is established, the flow rate is higher, and the protein in solution may be washed off by the high flow rate such that the particle is not coated. In an area of the cell where the flow rate is lower, near the eluent inlet and very close to the side walls, the protein in solution is more easily coated onto the surface of the COM crystals. The etching observed on the COM particles shown in Figure 6.14(B) is probably due to some modest dissolution of the particles synthesized at 25°C then equilibrated at 37°C in COM saturated solution also prepared at 25°C. The increase in temperature slightly increases the solubility of COM in aqueous solution and dissolution may occur. This argument is also consistent with the greater etching observed on the Ca^{2+}-rich ($10\bar{1}$) than the more $C_2O_4^{2-}$-rich (010) face. Such binding of Ca^{2+} by insoluble urinary macromolecules has been previously discussed by Finlayson and Dubois [Fin73].

6.3.4 Hydrodynamic Model of the Human Kidney

Kok and Khan [Kok94] calculated the volumetric flow rates in the kidney to be 0.2 ml/min to 39.1 ml/min, as shown in Table 6.4. These flow rates correspond to forces of 8.6×10^{-8} N to 2.3×10^{-4} N for a particle of 1 μm diameter calculated using the volumetric flow rates and tubule dimensions from Kok and Khan [Kok94] in the Poiseuille equation

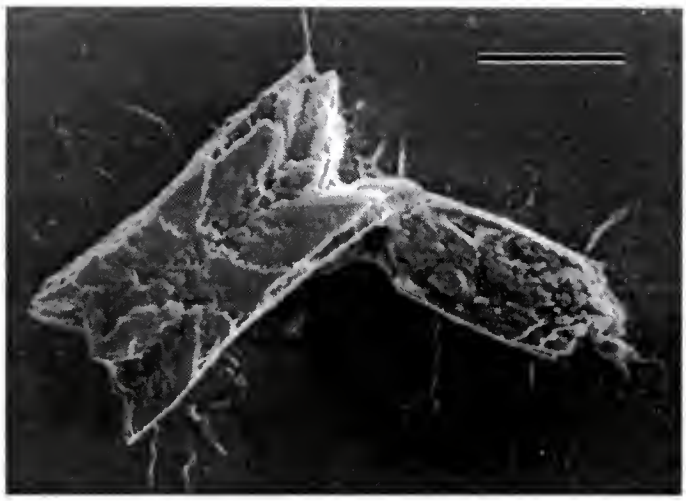

(A)

(B)

Figure 6.14. COM particles (A) coated during an adhesion experiment using fibronectin and (B) uncoated COM particles used in an adhesion experiment. Both photomicrographs were taken after flow. (bar = 10 μm)

Table 6.4. Human kidney tubule dimensions and volumetric flow rates reported by Kok and Khan [Kok94].

	Tubule Diameter (μm)	Volumetric Flow Rate (ml/min)
Proximal Tubule	25-35	39.1
Descending Loop of Henle	14-37	13.1
Ascending Loop of Henle	19-29	5.8
Distal Tubule	18-30	5.8
Outer Medullary Collecting Duct	30-35	3.7
Inner Medullary Collecting Duct	35-60	0.9
Duct of Bellini	60-100	0.2

(Appendix B). In the current research, the force is acting on the particles at a radius of 3.5 μm for a particle on the (010) and at a radius of 4.2 μm for a particle on the $(10\bar{1})$. For a particle of radius 5 μm, the forces acting on the particle range from $8.6x10^{-8}$ N to $2.3x10^{-4}$ N. The stress acting on a model COM particles having a 5 μm and 8 μm radius resulting from the hydrodynamic flow in each section of the kidney is shown in Figure 6.15. The current measured values of COM crystal adhesion to the macromolecular substrates are represented on Figure 6.15 by the shaded area. The experimentally measured values of adhesion correspond to the duct of Bellini and the inner medullary collecting duct of the human kidney, where the shear stresses are lower due to larger tubule sizes and lower flow rates. Many kidney stones are in fact found in these two regions of the human kidney near the papillary tip [Kha91, Kha95b].

6.4 Conclusions

Adhesion of COM crystals to different extracellular matrix proteins substrates were measured experimentally and found to adhere with varying strengths. The adhesion strength of the macromolecules increased as the ionic strength of the solution conditions increased. In the low ionic strength solution conditions a COM crystallographic dependence was observed. Trends existing in the adhesion results demonstrate that electrostatic interactions play a significant role in COM crystal adhesion to surfaces at low ionic strength. At high ionic strength, another mechanism of adhesion is occurring. At lower values of adhesion, van der Waals forces are dominant; however, at the higher adhesion values, specific bonding interactions are occurring.

Of the biologically significant materials, collagen type I exhibited the largest adhesive strength to COM at low ionic strength. However, at high ionic strength the material MATRIGEL®, a mixture of extracellular materials, exhibited the highest adhesive strength to COM.

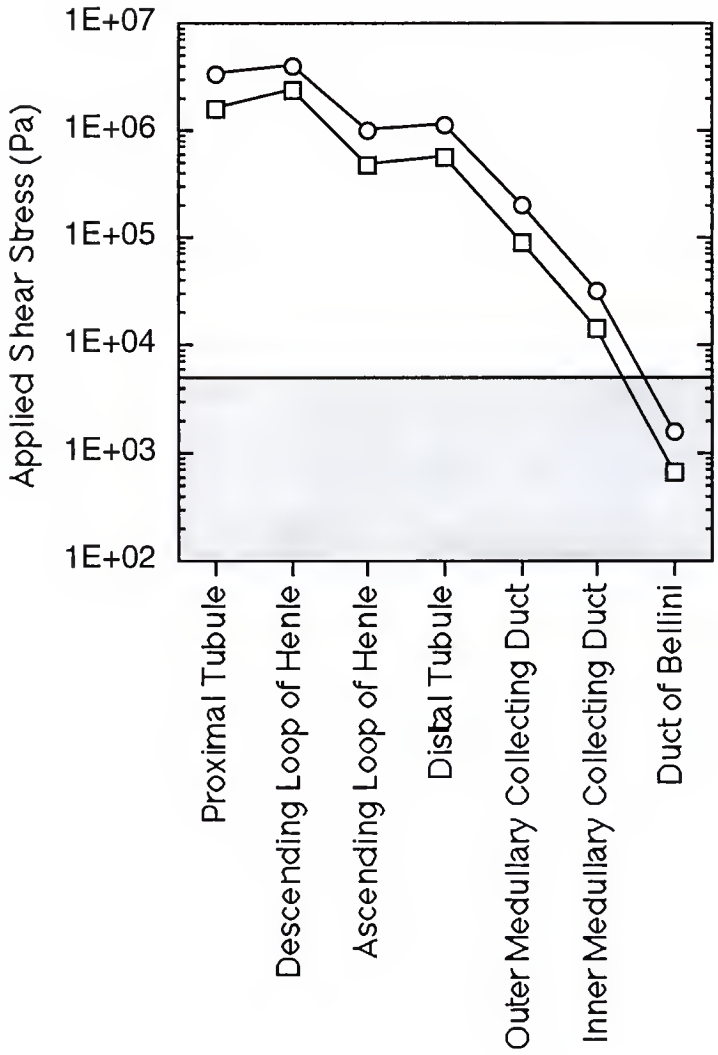

Figure 6.15. A plot of the stress on a 5 μm (□) to 8 μm (○) radius model COM particle under the hydrodynamic conditions found in the different areas in the human kidney. The shaded region represents the range of experimentally measured values of adhesion of COM to biological materials.

A hydrodynamic model was used to calculate the force applied on particles various radius in the different regions of the human kidney. The values of stress which correspond to the calculated forces on the particles correspond to the experimentally measured adhesive strength values between COM and the macromolecules reported herein.

CHAPTER 7
SUMMARY AND FUTURE WORK

7.1 Summary

COM crystals having a distinct shape and narrow particle size where synthesized. The equilibrium shapes with face indices of experimentally produced COM particles synthesized in different conditions have been successfully generated using the computer program SHAPE©. Computer calculations of theoretical crystallographic shapes have been reconciled to the observed shapes of experimentally synthesized COM particles under various conditions. Also, the seeding studies suggest that it is possible to control the size of COM crystals ("33" particles) by controlling the amount of seed materials. The computer program SHAPE© was demonstrated to be a useful tool to determine the face indices of COM crystals. The equilibrium shape of COM crystals based on the lattice parameters of Deganello and Piro [Deg81a] is reconciled to the morphology of the experimentally synthesized COM crystals from the comparison between the calculated shape and the morphological form of the experimentally derived particles.

Based on the face indices of the equilibrium shapes and atomic coordinates, the atomic structures of COM particles as a function of habit plane have also been generated by using the computer program ATOMS©. From the comparison between the theoretical atomic structures generated by ATOMS©, the (010) and (100) planes generated with the atomic coordinates published by Cocco and Sabelli [Coc62] are reconciled to the layering sequence reported by Deganello and Piro [Deg81a] and Tozzoli and Domeneghetti [Taz80].

The Hamaker constant of COM was determined using the Tabor-Winterton relationship. The dielectric constant of COM was deconvoluted from a COM/silicone composite using various mixing rules. The series mixing rule yielded the highest nonlinear regression coefficient, however the composites were clearly not representative of the series model. Therefore the Lichtenecker model, previously shown to describe irregularly shaped inclusions in a matrix [Mon47] was used and a value of 28.9 for the COM dielectric constant was determined. Plots of refractive index as a function of optical direction and wavelength were used to generate the ultraviolet absorption frequency and the dielectric and refractive index at the UV absorption frequency for use in the Hamaker constant calculation. The resulting value of the Hamaker constant, 13.7 ($\pm$5.90)x10^{-21} J, compares well with previously published values of 11.4 ($\pm$3.42)x10^{-21} J determined using the Gregory approximation.

A device was designed and built and the methodology developed to measure the adhesion strength between a particle and substrate. A second device was designed and built and the methodology developed to measure the zeta potential on a flat substrate. The parallel plate adhesion technique is a suitable method for determining the adhesive strength between a particle and a substrate in a dynamic liquid environment. The van der Waals interactions were estimated and related to the adhesion between COM crystals and a fused quartz substrate. Correlations were made between the theoretical atomic surface structure of COM and the crystallographic dependence on adhesive strength. Theoretical electrostatic considerations were invoked and are used to explain the crystallographic dependence.

Adhesion of COM crystals to different extracellular matrix protein substrates were measured experimentally and found to adhere with varying strengths. The adhesion strength of the macromolecules increased as the ionic strength of the solution conditions increased indicating a decrease in electrostatic repulsion due to compression of the electrical double layer at elevated ionic strengths. In the low ionic strength solution

conditions a COM crystallographic dependence was observed. A trend in the adhesion results demonstrates that electrostatic interaction plays a significant role in COM crystal adhesion to surfaces. At high ionic strength, another mechanism of adhesion is occurring. At lower values of adhesion, van der Waals forces are dominant; however, at the higher adhesion values, specific bonding interactions are occurring, which may be covalent in nature.

Of the biologically significant materials, collagen type I exhibited the largest adhesive stress to COM at low ionic strength. However, at high ionic strength the material MATRIGEL®, a mixture of extracellular materials, exhibited the highest adhesive strength to COM.

A hydrodynamic model was used to demonstrate that COM crystals may adhere to areas in the kidney where the flow rate is low and the corresponding shear stress is low. The application of the adhesion measuring technique reported in this work is promising for the study of kidney stone disease in that the importance of specific biological materials can be ranked with respect to their adhesive properties to COM crystals. This method of measuring adhesion may be an accurate predictor of COM kidney stone formation by a fixed particle mechanism. Also, the adhesion measuring technique may be used as a tool to evaluate biological materials implicated in kidney stone formation. Which, in turn, may allow researchers to focus on materials that have the greatest adhesion to COM.

7.2 Future Work

A surface energy study of COM with respect to the two dominant crystallographic planes should be performed. Surface and interfacial energies may be measured and the work of adhesion determined. From this information, the free energy change upon adhesion can be determined to investigate if adhesion of COM to a particular substrate is thermodynamically stable.

A re-evaluation of the video taped adhesion experiments to analyze the effect of orientation of the anisotropic COM particles with respect to the fluid flow direction should be performed. The error associated with the values of adhesive strength should decrease when only one particle orientation is analyzed at a time.

The effect of COM surface roughness on adhesion would also be an interesting study. The effect of mechanical bonding between a COM crystal and macromolecule which has reoriented itself near a COM particle may be observed.

The orientation of the macromolecular substrates should be determined to determine which molecular sites are available to interact with the COM crystal. Infrared spectroscopy can aid in this analysis. Also, Surface Potential Microscopy and Non-contact AFM may be performed on the substrates to map the surface potential and van der Waals forces, respectively.

Finally, in an effort to minimize adhesion between COM and macromolecular substrates, the effect of solute additions on adhesion (e.g., adhesion inhibitory molecules) should be measured. The aspect of initial testing of therapeutic drugs for kidney stone disease is promising.

APPENDIX A

DETERMINATION OF THE AREA OF COM CRYSTALLOGRAPHIC FACES USING EQUIVALENT SPHERICAL DIAMETER

Average Equivalent Spherical Diameter (μm)

$esd = 13.01$

$$V = \frac{\pi}{6}(esd)^3$$

$$a = \left[\frac{V}{(0.43)(0.35)}\right]^{1/3}$$

For COM "33" particles having the ratio of lengths of the crystal sides, A:B:C = 1.0:0.43:0.35,

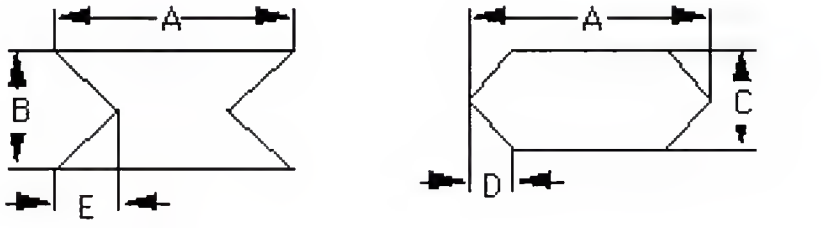

A := 1·a B := 0.43·a C := 0.35·a D := 0.19·a E := 0.33·a

The dimensions of the crystal (μm)

$A = 19.714$

$B = 8.477$

$C = 6.9$

Determining the area of the two major crystallographic faces (μm^2)

$$Area(010) = (A - 2 \cdot D) \cdot C + 2 \cdot \left(\frac{1}{2} \cdot C\right) \cdot D$$

$$Area(10\bar{1}) = A \cdot B - 2 \cdot \left(\frac{1}{2} \cdot B\right) \cdot E$$

$$Area(010) = 110.175$$

$$Area(10\bar{1}) = 111.963$$

APPENDIX B
DETERMINATION OF THE STRESS IN THE KIDNEY AS A FUNCTION OF FLOW AND DISTANCE FROM THE TUBULE WALL

Input:

i = 1, 2..7

D_i =	values taken from Kok and Khan [Kok90]
25	Diameter of Proximal Tubule (25-30 μm)
14	Diameter of Descending Loop of Henle (14-37 μm)
19	Diameter of Ascending Loop of Henle (19-29 μm)
18	Diameter of Distal Tubule (18-30 μm)
30	Diameter of Outer Medullary Collecting Duct (30-35 μm)
35	Diameter of Inner Medullary Collecting Duct (35-60 μm)
60	Diameter of Duct of Bellini (60-100 μm)

Q_i =	values taken from Kok and Khan [Kok90]
39.1	Volumetric flow through the Proximal Tubule (ml/min)
13.1	Volumetric flow through the Descending Loop of Henle (ml/min)
5.8	Volumetric flow through the Ascending Loop of Henle (ml/min
5.8	Volumetric flow through the Distal Tubule (ml/min)
3.7	Volumetric flow through the Outer Medullary Collecting Duct (ml/min)
0.9	Volumetric flow through the Inner Medullary Collecting Duct (ml/min)
0.2	Volumetric flow through the Duct of Bellini (ml/min)

$rstone = 3x10\text{-}6$	Radius of a kidney stone undergoing the calculated force (m)
$\eta = 0.6915$	Viscosity of water at 37°C (cPoise)
$a = 111x10^{-12}$	Area of crystal face (m^2)

Conversions and Calculations

Determination of radius from diameter

$$R_i = \frac{D_i \cdot 10^{-6}}{2}$$

Viscosity conversion- cPoise to Poise

$$\eta m = 0.1 \cdot \eta$$

Distance from the center of tubule at which the velocity is calculated

$$r_i = R_i - rstone$$

Flow rate conversion- ml/min to ml/s

$$Q\sec_i = \frac{Q_i}{60}$$

Flow rate conversion- ml/s to m^3/s

$$H_i = \frac{Q\sec_i}{100^3}$$

Calculation of the velosity at one stone radius from the tubule wall (m/s)

$$V_i = \frac{2 \cdot H_i}{R_i^4 \cdot \pi} \cdot \left(R_i^2 - r_i^2\right)$$

Calculation of the force acting at one stone radius from the tubule wall (N)

$$F_i = 1.7 \cdot 6 \cdot \pi \cdot \eta m \cdot rstone \cdot V_i$$

Calculation of the stress acting at one stone radius from the tubule wall with an interaction area of a (Pa)

$$Stress_i = \frac{F_i}{a}$$

Plot of kidney tubule section vs. stress

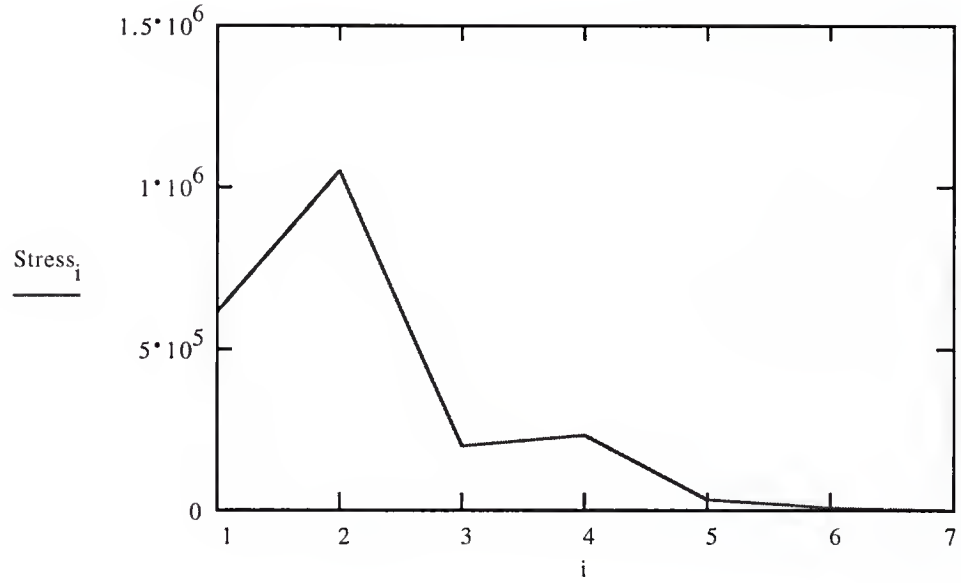

REFERENCES

Ada81 Adair, J.H., Ph.D. Dissertation, University of Florida, Gainesville.

Ada88 Adair, J.H., Aylmore, L.A.G., Brockis, J.G., and Bowyer, R.C., J. Colloid Interface Sci. 124, 1.

Ada91 Adair, J.H., Onoda, G.Y., and Finlayson, B., Am. J. Kidney Dis. 17[4], 3396.

Ada95 Adair, J.H., Linhart, R.V., Habeger, C.F., and Khan, S.R., in: Calcium Oxalate in Biological Systems, S.R. Khan, ed., CRC Press, Boca Raton, 37.

Add85 Addadi, L,. and Weiner, S., Proc. Natl. Acad. Sci. USA 82, 4110.

Alb89 Alberts, B. Bray, D., Lewis, J. Raff, M., Roberts, K., and Watson, J.D., Molecular Biol;ogy of the Cell, 2nd ed., Garland, New York, 787.

All90 Allen, T., Particle Size Measurement, Chapman and Hall, New York, 153.

Arc90 Archer, D.G. and Wang, P., J. Phys. Chem. Ref. Data 19, 371.

Bar78 Barouch, E., Matijevic, E., Ring, T.A., and Finlan, J.M., J. Colloid Interface Sci. 67[1], 1.

Ber90 Bergethon, P.R. and Simons, E.R., Biophysical Chemistry: Molecules to Membranes, Springer-Verlag, New York.

Big96 Bigalow, M.W, Wiessner, J.H. Kleinman, J.G., and Mandel, N.S., J. Urol. 155, 1094.

Boe94 Boeve, E. R., Cao, L. C., DeBruijn, W. C., Robertson, W. G., Romijn, J. C., and Schroder, F. H., J. Urol. 152, 531.

Boy68 Boyce, W.H., J. Med. 45, 673.

Bri28 Briggs, D.K., J. Phys. Chem. 32, 641.

Bro92 Brown, C.M. and Purich, D.L., in: Disorders of Bone and Mineral Metabolism,. F.L. Coe and M.J. Favus, eds., Raven Press, New York, 1.

Bul35 Bull, H.B., J. Amer. Chem. Soc. 57, 259.

Bus84 Busscher, H.J., Weerkamp, A.H., van der Mei, H.C., van Pelt, A.W.J., de Jong, H.P., and Arends, J., J. Appl. Enviro. Microbio. 48[5], 980.

Bus92 Busscher, H.J., Doornbusch, G.I., and Van der Mei, H.C., J. Dent. Res. 71[3], 491.

Bus93 Busnaina, A., Taylor, J., and Kashkoush, I., J. Adhesion Sci. Technol. 7[5], 441.

Cam89 Campbell, A.A., Ebrahimpour, A. Perez, L., Smesko, S.A., and Nancollas, G.H., Calcif Tissue Int 45, 122.

Cha84 Chan, D.Y.C. and Halle, B., J. Colloid Interface Sci. 102[2], 400.

Cha91 Charles, Y.C., Amer. J. Kidney Diseases 17 4], 420.

Cla95 Clark, J.Y., J. Urol. 154, 2020.

Coc61 Cocco, G., Atti. Accad. Naz. Lincei Rend. Cl. Sci. Fis Mat. Nat. 31, 292.

Coc62 Cocco, G., and Sabelli, C., Atti. Soc. Tascana Sci. Nat. Pisa, Proc. Verbali Mem. Ser. A 69[2], 289.

Cod94 Cody, A.M. and Cody, R.D., J. Crystal Growth 135, 235.

Coe91 Coe, F.L., Nakagawa, Y., and Parks, J.H., Am. J. Kidney Diseases 17[4], 407.

Con90 Conyers, R.A.J., Bals, R., and Rofe, A.M., Clin. Chem. 36[10], 1717.

Cor66 Corn, M., in Aerosol Science, ed. C.N. Davies, Academic Press, New York.

Cul78 Cullity, B.D., Elements of X-Ray Diffraction, 2nd ed., Addison-Wesley, Reading, MA.

Cur79a Curreri, P.A., Ph.D. Dissertation, University of Florida, Gainesville, FL.

Cur79b Curreri, P., Onoda, Y., Jr., and Finlayson, B., J. Colloid Interface Sci. 69[1], 170.

Cur87 Curreri, P.A., Onoda, G.Y., Jr., and Finlayson, B., in Proteins at Interfaces, Physicochemical and Biochemical Studies, J.L. Brash and T.A. Horbett, Eds., American Chemical Society, Washington, D.C., 278.

Deg80 Deganello, S., Zeitschrift für Kristallographie 152, 247.

Deg81a Deganello, S. and Piro, O., Neues Jahrbuch für Mineralogie Monatshefte 2, 81.

Deg81b Deganello, S., Acta Cryst. B37, 826.

Deg91 Deganello, S., Calcif. Tissue Int. 48, 421.

Der41 Derjaguin, B.V. and Landau, L., Acta Physicochim. URSS 14, 633.

Der54 Derjaguin, B.V., Disc. Faraday Soc. 18, 85.

Der61 Derjaguin, B.V. and Zimon, A.D., Kolloidn. Zh. 23[5], 544.

Dit82 Ditter, W., Eisenlauer, J., and Horn, D., in The Effect of Polymers on Dispersion Properties, Academic Press, New York, 323.

Dor77 Doroszewski, J., Skierski, J., and Przadka, L., Exp. Cell Res. 104, 335.

Dow92 Dowty, E., and Richards, R.P., SHAPE©, A Computer Program for Drawing Crystals, v.3.0.

Dow93 Dowty, E., ATOMS©, A Computer Program for Displaying Atomic Structures, v.2.0.

Duc91 Ducker, W.A., Senden, T.J., and Pashley, R.M., Nature 353, 239.

Ebd77 Ebdon, D., Statistics in Geography: A Practical Approach, Billing & Sons, Great Britain.

Ebi95 Ebisuno, S., Kohjimoto, Y., Tamura, M., Ohkawa, T., Eur. Urol. 28, 68.

Edy86 Edyvane, K.A., Ryall, R.L., and Marshall, V.R., Clin. Chim. Acta 156, 81.

Edy87a Edyvane, K.A., Ryall, R.L., and Marshall, V.R., Urol. Res. 15, 87.

Edy87b Edyvane, K.A., Ryall, R.L., Mazzaachi, R.D., and Marshall, V.R., Urol. Res. 15, 87.

Edy87c Edyvane, K.A., Hibberd, C.M., Harnett, R.M., Marshall, V.R,. and Ryall, R.L., Clin. Chim. Acta. 167, 329.

Eis85 Eisenlauer, J. and Horn, D., Colloids Surf. 14, 121.

Esk68 Eskinazi, S., Principles of Fluid Mechanics, 2nd ed., Allyn and Bacon, Boston.

Fai25 Fairbrother, F. and Mastin, H., J. Chem Soc. 127, 323.

Fin78a Finlayson, B., Kidney Int. 13, 344.

Fin78b Finlayson, B., and Reid, F., Invest. Urol. 15[6], 442.

Fin84 Finlayson B., Khan, S.R., and. Hackett, R.L., Scan. Elec. Microsc. III, 1419.

Fle78 Fleisch, H., Kidney Int. 13, 361.

For84 Forrester, J.V. and Lackie, J.M., J. Cell Sci. 70, 93

Gil79 Gill, W.B., Ruggiero, K., and Strauss, F.H., II, Invest. Urol. 17, 257.

Gol67 Goldman, A.J., Cox, R.J., and Brenner, H., Chem. Eng. Sci. 22, 653.

Gor59 Gordon, L.,. Salutsky, M.L, and Willard, H.H., Precipitation from Homogeneous Solution, John Wiley and Sons, New York.

Gre81 Gregory, J., Chem. Engr. Sci. 36[11], 1789.

Gre85 Gregory, J., J. Colloid Interface Sci. 105[2], 357.

Gro90 Grover, P.K., Ryall, R.L., and Marshall, V.R., Clin. Chim. Acta. 190, 223.

Hab97 Habeger, C.F., Condon, C., Khan, S.R., Adair, J.H., in print Colloid Surf.B.

Har86a Hartel, R.W., Gottung, B.E., Randolph, A.D., and Drach, G.W., AICHE J. 32[7], 1176.

Har86b Hartel, R.W., and Randolph, A.D., AIChE J. 32[7], 1186.

Hoc73 Hochmuth, R.M., Mohandas, N., and Blackshear Jr., P.L., Biophys. J. 13, 747.

Hog66 Hogg, R. Healy, T.W., and Fuerstenau, D.W., Trans. Faraday Soc. 62, 1638.

Hor77 Horn, J.M., Jr. and Onoda, G.Y., J. Colloid and Interface Sci. 61, 272.

Hor90 Horn, R.G., J. Am. Ceram. Soc. 73[5], 1117.

Hou80 Hough, D.B. and White, L.R., Adv. Colloid Interface Sci. 14, 3.

Hun62 Hunter, R.J. and Alexander, A.E., J. Colloid Sci. 17, 781.

Hun81 Hunter, R.J., Zeta Potential in Colloid Science: Principles and Applications, Academic Press, New York.

Hun93 Hunter, R.J., Introduction to Modern Colloid Science, Oxford Science, New York.

Ile79 Iler, R.K. The Chemistry of Silica: Solubility, Polymerization, Colloid and Surface Properties, and Biochemistry, John Wiley and Sons, New York.

Isr78 Israelachvilli, J.N. and Adams, G.J., J. Chem. Soc., Faraday Trans. 1 74, 975.

Isr92 Israelachvili, J.N., Intermolecular and Surface Forces, 2nd ed., Academic Press, New York.

Jon45 Jones, G. and Wood, L.A., J. Chem. Phys. 13,106.

Kal87 Kallay, N., Barouch, E., and Matijevic, E., Advan. Colloid Interface Sci. 27, 1.

Kha82 Khan, S.R., Finlayson, B., and Hackett, R.L, Am. J. Pathol. 107, 59.

Kha83a Khan, S.R., Finlayson, B., and Hackett, R.L., J. Urol. 130, 992.

Kha83b Khan, S.R., Finlayson, B., and Hackett, R.L., Scan. Elec. Microsc. pt. 1, 379.

Kha84 Khan, S.R., Cockrell, C.A., J. Urol. 132, 153.

Kha87 Khan, S.R. and Hackett, R.L., Scan. Microsc. 1[3], 1405.

Kha88 Khan, S.R., Shevock, P.N., and Hackett, R.L., J. Urol. 139[2], 418.

Kha91 Khan, S.R. and Hackett, R.L, Scanning Microsc. 5[3], 707.

Kha95a Khan, S.R., Urol. Res. 23, 71.

Kha95b Khan, S.R., Scanning Microsc. 9[1], 89.

Kle82 Kleinman, H.K., McGarvey, M.L., Liotta, L.A., Tryggvason, K., and Martin, G.R., Biochemistry 21[24], 6188.

Knu85 Knutson, K. and Lyman, D.J., Surface and Interfacial Aspects of Biomedical Polymers, Vol. 1: Surface Chemitry and Physics, J.D. Andrade, ed., Plenum, New York.

Koh96 Kohjimoto, Y., Ebisuno, S., Tamura, M., and Ohkawa, T., Urol. Res. 24, 193.

Kok90 Kok, D.J., Papoulos, S.E., and Bijvoet, O.L.M, Kidney Int. 37, 51.

Kok94 Kok, D.J. and Khan, S.R., Kidney Int. 46, 847.

Kor60 Kordecki, M.C. and Orr, C., AMA Arch. Environ. Health 1[1], 1.

Kri94 Krishnan, S., Busnaina, A.A., Rimai, D.S., and Demejo, L.P., J. Adhesion Sci. Technol. 8[11], 1357.

Kuc92 Kucharz, E.J., The Collagens: Biochemistry and Pathophysiology, Springer-Verlag, New York.

Kru67 Krupp, H., Advan. Colloid Interface Sci. 1, 111.

Küh87a Kühn, K., in Structure and Function of Collagen Types, R Mayne and R.E. Burgeson, eds., Academic Press, Orlando, 1.

Küh87b Kühn, K., in Structure and Function of Collagen Types, R Mayne and R.E. Burgeson, eds., Academic Press, Orlando, 43.

Kuo80 Kuo, R.J. and Matijevic, E., J. Colloid Interface Sci. 78[2], 407.

Lan88 Lanzalaco, A.C., Singh, R.P., Smesko, S.A., Nancollas, G.H., Sufrin, G., Binette, M., and Binette, J.P., J. Urol. 139, 190.

Lea77 Leal, J. and Finlayson, B., Invest. Urol. 14[4], 278.

Lid90 Lide, D.R., CRC Handbook of Chemistry and Physics, 71st ed., CRC Press, Boca Raton.

Lie92 Lieske, J.C., Walsh-Reitz, M.M., and Toback, F.G., Am. J. Physiol. 262, F622.

Lie93 Lieske, J.C. and Toback, F.G, Am J. Physiol. 264, F800.

Lie94 Lieske, J.C., Swift, H., Martin, T., Patterson, B., and Toback, F.G, Proc. Nat. Acad. Sci. USA 91, 6987.

Lie95 Lieske, J.C., Leonard, R., and Toback, F.G., Am. J. Physiol. 268, F612.

Lie96a Lieske, J.C., Leonard, R., Swift, H., and Toback, F.G., Am. J. Physiol. 270, F192.

Lie96b Leiske, J.C., Toback, F.G., and Deganello, S., Calcif. Tissue Int. 58, 195.

Man81 Mandel, N.S. and Mandel, G.S., in Urolithiasis: Clinical and Basic Research, Plenum Press, New York.

Man87 Mandel, N.S., Mandel G.S., and Hasegawa, A.T., J. Urol. 138, 557.

Man91 Mandel, N. and Riese, R., Am. J. Kidney Dis. 17[4], 402.

Man94 Mandel, N., J. Am. Soc. Nephrol. 5, 537.

Mar30 Martin, W.McK. and Gortner, R.A., J. Phys. Chem. 34, 1509.

Mar86 Marcott, C., ASM Handbook, Vol. 10: Materials Characterization, ASM International, USA.

Mat81 Matijevic, E., Pure Appl. Chem. 53, 2167.

Mey71 Meyer, A.S., Finlayson, B., and DuBois L., Br. J. Urol. 43, 154.

Mey82 Meyer, J.L. and Thomas, W.C., Jr., J. Urol. 128, 1372.

Moh74 Mohandas, N., Hochmuth, R.M., and Spaeth, E.E., J. Biomed. Mater. Res. 8, 119.

Mon47 Montgomery, C. G., Techniques in Microwave Measurement, McGraw-Hill, New York.

Nak83 Nakagawa, Y., Abram, V., Kezdy, F.J., Kaiser, E.T., and Coe, F.L., J. Biol. Chem. 258, 12594.

Nak87 Nakagawa, Y., Ahmed, M., Hall, S.L., Deganello, S. and Coe, F.L., J. Clin. Invest. 79, 1782.

Nat95 National Hospital Discharge Survey: Annual Summary, 1993, CDC, HHS.

NIH97 www.niddk.nih.gov/KU_Stats/kustats.htm.

Nyv85 Nyvlt, J., Söhnel, O., Matuchová, M., and Broul, M., The Kinetics of Industrial Crystallization, Elsevier, New York.

Ols78 Olsson, J., Ph.D. Dissertation, University of Goteborg, Sweden.

Ove52 Overbeek, J.Th.G., Colloid Science, Vol. 1, H.R. Kruyt, ed., Elsevier, New York, 115.

Owe87 Owens, N.F., Gingell, D., and Rutter, P.R., J. Cell Sci. 87, 667.

Pal51 Palache, C., Berman, H., Frondel, C., The System of Minerology, Vol. 2., Wiley, New York.

Pel82 Pelton, R.H., Nugent, H., and Allen, L. H., Colloids and Surf. 4, 397.

Pel84 Pelton, R.H. and Allen, L.H., J. Colloid Interface Sci. 99[2], 387.

Pri47 Prien, E.L. and Frondel, C., J. Urol. 57, 946.

Pri86 Prien, E.L. and Prien, E.L., Am. J. Med. 45, 654.

Ran88 Randolph, A.D., and Larson, M.A., Theory of Particulate Processess: Analysis and Techniques of Continous Crystallization, Academic Press, San Diego.

Ray87 Ray, D.T. and Hogg, R., J. Colloid Interface Sci., 116[1], 3256,.

Rie88 Riese, R.J., Riese, R.W., Kleinman, J.G., Wiessner, J.H., Mandel, G.S., and Mandel, N.S., Am. J. Physiol. 225, F1025.

Rie92 Riese, R.J., Mandel, N.S., Weissner, J.H., Mandel, G.S., Becker, C.G., and Kleinman, J.G., Am. J. Physiol. 262, F177.

Rob69 Robertson, W.G., Clin. Chim. Acta. 26, 105.

Rob85 Robertson, W.G. and Peacock, M., in Pathogenesis of Urolithiasis in Urolithiasis Etiology Diagnosis, Springer-Verlag, New York, 185.

Rob86 Robertson, W.G., Urol. Int. 41, 329.

Rut47 Rutgers, A.J. and DeSmet, M., Trans. Faraday Soc. 43, 102.

Rya81a Ryall, R.L., Harnett, R.M., and Marshall, V.R,. Clin. Chim. Acta 112, 349.

Rya81b Ryall, R., Ryall, R.G., and Marshall, V.R., Invest. Urol. 18[5], 396.

Rya81c Ryall, R.L., Bagley, C.J., and Marshall, V.R., Invest. Urol. 18[5], 401, 1981.

Rya84 Ryall, R.L. and Marshall, V.R., Clin. Chim. Acta 141, 197.

Rya86 Ryall, R., Harnett, R.M., and Marshall, V.R., J. Urol. 135, 174.

Ryd95 Ryde, N., and Matijevic, E., J. Colloid Interface Sci. 169, 468.

Sca92 Scales, P.J., Grieser, F., and Healy, T.W., Langmuir 8, 965.

Sch90 Scheaffer, R.L., and McClave, J.T., Probability and Statistics for Engineers, PWS-KENT, Boston.

Scu86a Scurr, D.S., and Robertson, W.G., J. Urol. 136, 128.

Scu86b Scurr, D.S,. and Robertson, W.G., J. Urol. 136, 505.

Son72 Sonntag, H. and Strenge, K., Coagulation and Stability of Disperse Systems (Engl. trans.), Halsted Press, New York.

Ste90 Stevens, M.P., Polymer Chemistry: An Introduction, 2nd ed., Oxford, New York.

Tab69 Tabor, D., and Winterton, R.H.S., Proc. Roy. Soc. A 312, 435.

Tab80 Tabor, F.R.S. and Winterton, R.H.S., Proc. Roy. Soc. A 312, 327.

Taz80 Tazzoli, V., and Domeneghetti, C., Amer. Min. 65, 327.

Tho85 Thormahlen, I., Straub, J., and Grigul, U., J. Phys. Chem. Ref. Data 14, 933.

Tru90 Truskey, G.A. and Pirone, J.S., J. Biomed. Mater. Res. 24, 1333.

van80 van Wagenen, R.A. and Andrade, J.D., J. Colloid Interface Sci. 76[2], 305.

van92 van Kooten, T.G., Schakenraad, J.M., Van der Mei, H.C., and Busscher, H.J., J. Biomed. Mater. Res. 26, 725.

Ver48 Verwey and Overbeek, Theory of the Stability of Lyophobic Colloids, Elsevier, New York.

Ver96 Verkoelen, C.F., Romijn, J.C., Cao, L.C., Boeve, E.R., DeBruin, W.C., and Schroder, F.H., J. Urol. 155, 749.

Vis76 Visser, J., in Surface and Colloid Science, Vol.8., E. Matijevic ed., Wiley-Interscience, New York.

Von54 Von Hipple, A., Dielectrics and Waves, Wiley, New York.

Wie87 Wiessner, J.H., Kleinman, J.G., Blumenthal, S.S., Garancis, J.C., Mandel, G.S., and Mandel, N.S., J. Urol. 138, 640.

Woo46 Wood, L.A., J. Am. Chem. Soc. 68, 437.

Yam96 Yamate, T., Kohri, K., Umekawa, T., Amasaki, N., Isakawa, Y., Iguchi, M., Kurita, T., Eur. Urol. 30, 388.

Yar87 Yarbrough, W.A., Gururaja, T.R., and Cross, L.E., Am. Ceram. Soc. Bull. 66[4], 692.

Zim82 Zimon, A.D., Adhesion of Dust and Powder, 2nd ed., Consultants Bureau, New York.

BIOGRAPHICAL SKETCH

Craig Fredrick Habeger was born to James and Sandra Habeger on June 10, 1969 in Youngstown, Ohio. He was the youngest of three children. Growing up in a rural area around Youngstown, he honed his common sense skills. He often helped or watched his grandfather, father, brother, and uncles fix farm and other machinery which gave him a good mechanical understanding and an interest in engineering. During his childhood, his parents instilled in him a strong sense of ethics, morality, honesty, and integrity.

After high school, Craig attended the University of Cincinnati to earn his Bachelor of Science degree, where his focus of study was materials science and engineering. During his undergraduate years at the UC, he groomed his social skills enabling him to work well in a team setting. Also, during that time, he began to weight train. This activity lead to greater self confidence and perseverance. He graduated from UC in June of 1992.

Craig moved onto graduate school at the University of Florida in the Materials Science and Engineering Department. At UF, he pursued a Doctor of Philosophy degree in Materials Science and Engineering, specializing in colloidal processing of ceramic materials. During his time at Florida, Craig has grown tremendously. He is viewed as a manager and a leader whose valued opinions are often sought.

On June 24, 1995 Craig Habeger married Nicole Schindler. On October 1, 1997 Craig successfully defended his Ph.D. dissertation, becoming the first Ph.D. in his family (hopefully not the last). After graduating, Craig, Nicole and their first addition (estimated arrival, March 20, 1998) will ride off into the sunset and live happily ever after.

I certify that I have read this study and that in my opinion it conforms to acceptable standards of scholarly presentation and is fully adequate, in scope and quality, as a dissertation for the degree of Doctor of Philosophy.

James H. Adair, Chair
Associate Professor of Materials Science and Engineering

I certify that I have read this study and that in my opinion it conforms to acceptable standards of scholarly presentation and is fully adequate, in scope and quality, as a dissertation for the degree of Doctor of Philosophy.

Christopher D. Batich
Professor of Materials Science and Engineering

I certify that I have read this study and that in my opinion it conforms to acceptable standards of scholarly presentation and is fully adequate, in scope and quality, as a dissertation for the degree of Doctor of Philosophy.

Anthony B. Brennan
Associate Professor of Materials Science and Engineering

I certify that I have read this study and that in my opinion it conforms to acceptable standards of scholarly presentation and is fully adequate, in scope and quality, as a dissertation for the degree of Doctor of Philosophy.

Brij M. Moudgil
Professor of Materials Science and Engineering

I certify that I have read this study and that in my opinion it conforms to acceptable standards of scholarly presentation and is fully adequate, in scope and quality, as a dissertation for the degree of Doctor of Philisophy.

R. L. Hackett

Raymond L. Hackett
Professor of Pathology and Laboratory Medicine

This dissertation was submitted to the Graduate Faculty of the College of Engineering and to the Graduate School and was accepted as partial fulfillment of the requirements for the degree of Doctor of Philosophy.

December, 1997

Winfred M. Phillips
Dean, College of Engineering

Karen A Holbrook
Dean, Graduate School

LD
1780
1997
.H113

UNIVERSITY OF FLORIDA
3 1262 08554 2438